UNIVERSIDAD
DE GRANADA

Facultad de Ciencias

Departamento de Física Aplicada

Programa de Doctorado en Física y Ciencias del Espacio

Tesis Doctoral

Enhancing magnetorheology with unsteady triaxial magnetic fields

Autor: Matthew Terkel

Director: Juan de Vicente Álvarez-Manzaneda

2023

Editor: Universidad de Granada. Tesis Doctorales
Autor: Matthew Terkel
ISBN: 978-84-1195-026-8
URI: https://hdl.handle.net/10481/84672

Acknowledgements

First and foremost, this PhD would not have been possible without the continuous support of my supervisor Juan de Vicente, who so warmly welcomed me into his research group. Thank you for your patience as I improved my Spanish language skills. ¡No puedo creer que hayan pasado 5 años! Pero supongo que el tiempo pasa rápido en buena compañía entre juntas semanales, tiempo en el laboratorio, Nesteas en la cafetería, y una pandemia global para distraerse.

I would like to thank everyone who at one point in time passed through the Sala PIF, and all the members of our research group throughout my time in Granada: Óscar, José, Keshvad, Elisa, Guillermo, José Antonio, Robert, Alejandro, Jesús, Javier, Antonio as well as all the technicians, undergraduate and master students who I had the opportunity to work alongside. I would especially like to express my gratitude to Fernando and María José for their guidance and willingness to share their teaching knowledge, and of course to Stefania who was also there to support my teaching and with whom collaborating on experiments was always an enjoyable experience.

Thank you Sébastien Manneville, Thomas Gibaud, and Thibaut Divoux at ENS de Lyon for welcoming me into your lab during my studies abroad and your continued collaboration.

Aurelio – no te puedo agradecer suficientemente por ser el mejor profesor de español y amigo.

I wish to acknowledge Goldina and Vincent, who both influenced me to pursue my PhD and who continue to inspire me.

To my friends and parents back home who have always supported my education, even when I insist on moving across countries, oceans, and continents – thank you. This thesis is dedicated to my parents. And Karen, obviously!

Table of Contents

Abstract

Magnetorheological (MR) fluids have long been used for industrial applications that require a quick, reversible change in fluid properties such as a spontaneous increase in viscosity in the presence of an external magnetic field. Micron-sized magnetizable particles dispersed in a nonmagnetic fluid carrier structure via their dipolar interactions in line with the field direction — traditionally a uniaxial DC field. For sufficiently large field strengths, particle structuration usually consisting in the formation of chains or thicker columnar structures restricts fluid flow causing the emergence of a yield stress in the MR fluid and making it more robust to deformation under shear. Dampers, shock absorbers, and braking systems are a few industrial applications that take advantage of the unique adaptability of these smart materials.

With our homemade triaxial magnetic field generator we have carried out a complete study of the MR response of more complex precession-like magnetic fields, the particle mesostructures formed under these fields, and other time-dependent field configurations. For time-varying fields the relation between the hydrodynamic and magnetic forces plays a key role in the aggregation dynamics in a magnetic suspension. A nondimensional parameter known as the Mason number relates these two magnitudes. The triaxial device was designed and constructed with the intention of carrying out both videomicroscopy and rheometry experiments. The MR enhancement was quantified through an analysis of the storage modulus. Columns, spirals, and layered structures are some of the 3D particle structures we can form using the triaxial field generator by means of the particles' dipolar and time-averaged magnetostatic interactions. Two main aggregation mechanisms are proposed to explain the MR enhancement — lateral coalescence between vicinal columnar structures, and through particle compaction. The former of the two mechanisms is further

justified with particle-level simulations and a study of the average cluster size of simulated particle structures under low angle precession fields.

Inspired by the emergent dynamics seen in our experimental work, we have integrated particle self-assembly for a hydrogel composed of modified polysaccharide and protein. Directional, or guided, cell growth often involves a fabricated 3D solid scaffolding matrix for which cells can attach to. Although this method is effective, we propose a novel path for tissue engineering for our magnetically-responsive system using both uniaxial and unsteady magnetic fields and the complex structures witnessed in the MR experiments. A 3D anisotropic particle network is first structured under a pre-programmed magnetic field configuration in its fluid-like viscous state. The particle structure, and the suspended cells, are encapsulated in position as the carrier fluid polymerizes via the Schiff reaction. Confocal microscopy shows the cells embedded within the particle network, and multi-day analysis of the hydrogels suggests the particle structure stays intact allowing a lasting scaffold for cell growth. We hope this study establishes a groundwork for the possibilities of less invasive injectable alternatives for cell regeneration remedies.

Resumen

Los fluidos magnetoreológicos (MR) se han utilizado durante mucho tiempo para aplicaciones industriales que requieren un cambio rápido y reversible en las propiedades del fluido, como por ejemplo un aumento de la viscosidad en presencia de un campo magnético aplicado. Partículas magnéticas de tamaño micrométrico dispersadas en un líquido no magnético estructuran a través de interacciones dipolares en línea con la dirección del campo, tradicionalmente un campo DC uniaxial. Para intensidades de campo suficientemente grandes, la estructuración de partículas conlleva a la formación de cadenas o estructuras columnares más gruesas que restringen el movimiento provocando la aparición de un esfuerzo umbral y dotando al fluido de un carácter viscoelástico. Los amortiguadores y los sistemas de frenado son algunas de las aplicaciones industriales que aprovechan la adaptabilidad única de estos materiales inteligentes.

Usando un generador de campo magnético triaxial construido en nuestro laboratorio, hemos llevado a cabo un estudio detallado de la respuesta reológica bajo campos magnéticos de precesión, la formación de mesoestructuras de partículas bajo estos campos y otras configuraciones de campo no estacionarios. Para campos que varían en el tiempo, el balance entre las fuerzas hidrodinámicas y magnéticas juega un papel clave en la dinámica de agregación en una suspensión magnética. Un parámetro adimensional, conocido como número de Mason (Mn), relaciona estas dos magnitudes. El dispositivo triaxial fue diseñado y construido con la intención de realizar experimentos tanto de videomicroscopía como de reometría. La mejora de las propiedades reológicas se cuantificó a través de un análisis del módulo de almacenamiento. Columnas, espirales y estructuras en capas son algunas de las estructuras de partículas 3D que podemos formar usando el generador de

campo triaxial gracias a interacciones magnetostáticas dipolares y otras promediadas en el tiempo a alto Mn. Se proponen dos mecanismos de agregación principales para explicar la mejora reológica: la coalescencia lateral entre las estructuras columnares vecinas y la compactación de los agregados. El primero de los dos mecanismos se demuestra con simulaciones a nivel de partícula y un estudio del tamaño de agregados de partículas simuladas bajo campos de precesión de ángulo pequeño.

Inspirándonos en la dinámica emergente observada en nuestro trabajo experimental, hemos integrado el autoensamblaje de partículas en un hidrogel compuesto de polisacáridos y proteínas modificadas. El crecimiento celular direccional o guiado requiere de una matriz sólida 3D a la que se puedan adherir las células. Aunque este método es efectivo, proponemos aquí un camino novedoso para la ingeniería de tejidos mediante el uso de campos magnéticos uniaxiales no estacionarios y estructuras complejas observadas en los experimentos con fluidos MR. Primero se estructura una red 3D anisotrópica de partículas bajo una configuración de campo magnético preprogramada en estado líquido (pregel). La estructura en base a partículas y las células suspendidas se encapsulan a medida que el fluido portador polimeriza a través de una reacción de Schiff. Técnicas de microscopía confocal muestran células incorporadas dentro de la red de partículas, y el análisis de varios días de los hidrogeles sugiere que la estructura de las partículas permanece intacta, lo que permite una matriz duradera para el crecimiento celular. Esperamos que este estudio establezca una base para alternativas inyectables menos invasivas en regeneración tisular.

Chapter 1

Introduction

Smart materials are given that illustrious identifier for their innate ability to respond to their environment. Whether this external stimulus be stress, electric or magnetic field, temperature, or pH motivated, the ability to self-adapt is one of the main features of these materials [1]. In addition to other qualities such as multi-functioning and self-sensing, smart materials are useful for a number of potential applications, for example shape-memory, chemical sensors, and self-healing polymers [2-3]. In the latter case, dynamic covalent networks of crosslinked polymers are the fundamental explanation for the success of self-healing systems in repairing mechanical damage, used both in hydrogel formulations and more recently in magnetorheological elastomers [4]. Perhaps the most popular subclass involving magnetic stimulus, however, would be magnetorheological (MR) fluids, with their mechanical properties dependent on the external field.

In developing a magnetorheological fluid there are generally two phases, with at least one of them being magnetically responsive. A suspension of magnetic particles dispersed in a non-magnetic Newtonian fluid carrier is considered our most simple design for a MR fluid [5-6]. Depending on the particle size these smart materials can be broken down into two main categories, ferrofluids and traditional MR fluids. Ferrofluids consist of particles on the order of tens of nanometers where thermal fluctuations play a key role in their response to an external magnetic field. This Brownian energy often dominates the magnetic forces resulting in this type of fluid remaining in their liquid state while magnetized [7]. Inverse ferrofluids are a multiphase system with the addition of non-magnetic particles dispersed in a ferrofluid. Typically, the MR effect of these suspensions are not as responsive as traditional MR fluids. However, there is more versatility in the design of non-magnetic particles, with particle

morphology and surface treatments available and specifically tailored for a particular purpose [8]. Additionally, the interaction between the larger non-magnetic particles and the nanosized particles can reduce the likelihood of sedimentation. For these reasons inverse ferrofluids are still favored in some circumstances.

Traditional MR fluids are usually composed of micron-sized magnetic particles that are much more responsive to external fields. Magnetic fields drive a phase separation, with the particles structuring in line with the field, leading to a liquid to solid transition in the fluid's mechanical properties and an increase in the fluid viscosity. A yield stress also arises from this transition, meaning some stress threshold must be met in order to make the fluid flow. For stresses below this threshold the fluid deformation is considered reversible [5]. This is made possible by working with larger sized magnetic particles with a higher magnetization. A common disadvantage of working with these particles is that the material used usually contains high iron content, which is generally denser than the carrier fluid. Particle sedimentation is one of the most frequent obstacles that commercial MR fluids must address in their design and implementation [6].

In the context of enhancing the magnetorheological response of an MR fluid, the work presented in this thesis aims to do so through external control of the magnetic field. This is made possible with a field generator capable of producing more complex fields. However, up until now MR enhancement would involve modifying the components or phases of the MR fluid to then study its effect under traditional uniaxial fields. Particle agglomeration and sedimentation are two main focuses in formulating MR fluids. In the absence of a field one would hope that the magnetic particles remain dispersed and not settle out of suspension. To avoid particle agglomeration steric stabilization of the particle surface is a common practice [9]. Surface treatments with surfactants provide an interparticle buffer to reduce particle contact. Other surface treatment techniques, such as silica encapsulation, help reduce oxidative stress on the particle surface leading to more corrosion resistance [10].

To prevent particle sedimentation many formulations have been tested [6]. Bidisperse suspensions improve suspension stability by incorporating more than one particle type. For bimodal MR fluids, this entails using two different sized particles. By mixing micron-sized particles (as are typical for MR fluids)

with a secondary nanosized particle the Brownian energy of the smaller particles can impede the settling of the larger type through their particle collisions [11-12]. Furthermore, dimorphic suspensions call for two particle types of different form, for example spherical and rod-shaped particles. Due to their anisotropic shape, magnetized rods can form a secondary particle structure for which the spherical particles and particle chains can find themselves entrapped in. Moreover, when the field is removed the rod structure can remain intact, resulting in a slower sedimentation rate of the spherical particles [13-14]. While these examples of bidisperse systems may facilitate redispersibility, the secondary particle phase could reduce the MR response by acting as a physical barrier for particle interaction or due to their inferior magnetic properties. For this reason, we will focus our work using the well-studied traditional MR fluid system (single phase particles suspended in carrier fluid), but from an exciting new perspective of multiaxial field control.

MR fluids are a unique subclass of yield stress materials. In the absence of an external magnetic field these fluids characteristically behave like Newtonian fluids. However, when a field is applied the viscosity can increases multiple orders of magnitude in a matter of a few milliseconds. This spontaneous change in behavior is often coupled with an emergence of a yield stress. This is due to the formation of particle structures that aggregate in the direction of the field, and thus strengthening the fluid and making it more resistant to deformation [5]. For a sheared MR fluid there are three yield stresses to consider. The first is the elastic-limit stress. For low shear strains an MR fluid suspension behaves like a viscoelastic material, meaning the structured suspension opposes shear flow and strain linearly under an imposed shear stress. The elastic-limit stress therefore is the maximum applied stress in which when reversed and removed the MR fluid can obtain complete recovery. Next, the static yield stress is defined as the minimum stress necessary to make the fluid flow. According to de Vicente *et al.,* this stress is related more to the onset of slip between the particle structures and the shearing boundary than actual fracturing of the structure. At a sufficiently large shear stress, the structure will continuously fracture and restructure (as long as the field is still applied), with the onset of this response corresponding to the dynamic yield stress [5,15].

In general, the yield stress of an MR fluid is proportional to the strength of the magnetic field squared, $\tau_y \propto H_0^2$. Of course, for high field strengths the particles magnetization approaches its saturation and thus an upper limit to the measurable viscosity and yield stress is reached. When working with particles

of little remanent magnetism (soft particles), the drastic change in viscosity is reversible when the external field is removed. The particles lose their magnetism and structure, and redisperse back into suspension.

MR fluids, and the MR effect, have traditionally been studied under uniaxial magnetic fields out of convenience [16]. These experimental setups usually involve a coil situated around the base of a rheometer that induces a field in the z-axis, or the direction orthogonal to the imposed shear. To properly study these fluids under applied shear and more complex field configurations, we required an integrated field generator capable of producing multidimensional and time-varying fields - a feat on its own merit.

The motivation of the work presented in this thesis originates from our desire to explore the magnetorheological response of MR fluids beyond what is currently reported in the literature for uniaxial fields. We know that particles structure into chains and columnar structures when a static field is applied; however, with the proper technology to generate more advanced field configurations we are no longer limited to this singular structural response. Our research presented here has been greatly inspired by the work of Fernando Donado and James E. Martin, with the latter stating in their 2013 review on magnetic systems under time-dependent magnetic fields that the magnetorheology, or the study of these systems simultaneously under multiaxial field forces and applied shear, is still largely unexplored [2]. Martin has extensively studied triaxial magnetic fields, developed a chain model for precession fields, and identified optimal balanced time-dependent fields to induce vortex mixing in suspension, among a number of other research accomplishments in this field [17-18]. However, as alluded to above studying the magnetorheology of these systems is difficult due to the obstacle of the often bulky hardware involved to generate such fields.

On the other hand, Donado and their colleagues were the first to begin studying the MR response of their suspension of magnetic particles under a non-stationary field, in their case a low angle perturbation field [19-20]. A perturbation field is a biaxial field configuration where an oscillatory field is directed perpendicular to a static field. In those experiments they studied the aggregation kinetics (average chain length) in a 2D system of sedimented particles, while varying experimental parameters such as the field frequency, viscosity of the carrier fluid, and particle concentration. It was determined that lower viscosities and higher particle concentrations both maximized the chain

lengths. Furthermore, an optimal frequency of $f = 2$ Hz showed a peak in the average length of the chain-shaped clusters. Coincidently, this frequency when plugged into their approximation of the Mason number for a perturbation field resulted in $\mathrm{Mn} \sim 1$ [20]. Reflecting on these results through the lens of the results presented in this work, it is no surprise that the Mn reaches a peak when the magnetostatic and hydrodynamic forces are balanced, and that the average chain length decreases for higher frequencies given what we know of structures collapsing at larger Mn and interacting less with their surroundings.

Moreover, moving into a 3D space Donado also studied the effective viscosity response while applying a perturbation field. Similarly, they studied the effect of both field frequency and particle concentration and found a greater viscosity increase for higher concentrations and an optimal frequency at 2 Hz. Interestingly, when the perturbation field was removed and the field was returned to a static uniaxial field, they witnessed a further uptick in the measured viscosity [19]. In our experimental work we will also adhere to their protocol of first applying a uniaxial field, followed by the non-stationary field, and then returning to a static field. In this way we can directly compare the MR effect of our unsteady field configuration to the baseline static field case. In a later paper on the lateral aggregation induced by perturbation fields, Donado and Moctezuma make an argument for chain coalescence as depending on lateral displacement and separation, as well as the effective sweeping area of the chain that the perturbation field brings about. An oscillatory movement in neighboring chains provoking a lateral displacement can be a fundamental explanation for driving chain aggregation [20]. This displacement can move chains from an in registry to out of registry spatial orientation, with the former producing a repulsive interaction between chains and the latter an attractive interaction. As previously reported by Furst and Gast the short-range interactions between rigid chains can be either attractive or repulsive depending on the displacement [21].

Overall, the study into perturbation fields driving an enhanced response in MR fluids was only an introduction into the possible research that we have since been able to carry out. At the time these perturbation fields were generated using a set of Helmholtz coils, which often produce low field strengths due to larger working distances between the coils and the sample. Also, the rheology tests were done using a viscometer rather than a fully integrated rheometer. Since then we have constructed our homemade triaxial magnetic field

generator designed for operating in conjunction with a modified MCR501 rheometer from Anton Paar.

Lastly, it is worth commenting on the varied uses of MR fluids from industrial applications to the biomedical sector. Perhaps the most common industrial use for MR fluids is their employment as dampers, or shock absorbers [22-23]. Unlike conventional (hydraulic) shock absorbers that may have a constant setting, MR fluid dampers can constantly be modified as desired given that the damping force is regulated by the magnetic field strength. This greater control over dissipating shock energy makes MR dampers appealing alternatives on the market. Rotary brakes are the next most popular commercial use for MR fluids [24]. By activating a magnetic field, a rotating shaft immersed in a magnetic fluid will expectedly slow down as the viscous forces would increase. The ease of field induced torque control makes MR fluid rotary devices highly efficient braking systems. Another industrial use for MR fluids is in optical polishing [25]. Structured magnetically responsive particles can interact with non-magnetic abrasive particles to affect the surface finish. Of course, the functionality and long-term durability of all these devices is also dependent on the state of the MR fluid in its off state, or when magnetic fields are not applied. Considerable attention and design have gone into particle redispersibility and preventing sedimentation to make these devices more effective.

On the biomedical front, MR fluids have been employed in in-vitro experiments for cancer treatment. Here a field induced simulated blood embolization was investigated to study their sealing strength in suppressing blood supply to a tumor [26]. For its damping abilities MR fluids have also been used for artificial joints and prosthesis [24]. Currently, magnetic responsive particles are being used in innovative tissue engineering research. Hydrogel polymer networks are often used in tissue engineering practices for their high water content and similarities to the microenvironment of native biological tissue [27]. Magnetic particles ingested by cells are thereafter capable of being structured into anisotropic oriented structures, which more accurately reflects certain nerve, muscle and cardiovascular tissues [28]. Alternatively, in a mixed medium hydrogel, particle doped microelements have been shown to provide an oriented extracellular scaffold that helps guide cell growth in a preferred field aligned direction. For a study involving neurons, this guided alignment was visualized by neurite outgrowth following the same direction as the hydrogel had been structured by the external field [29]. In these experiments the magnetic control was very basic, simply using magnets to

generate a uniaxial field during the gelling phase of the hydrogel precursor solution. There is certainly an opportunity to incorporate more advanced field control in creating magnetic hydrogels, as is explored as an application of the research presented in this thesis.

In the present work MR fluids and their enhanced properties in unsteady magnetic fields are studied. Dynamic triaxial field control has allowed us to generate a variety of field configurations that until recently have not been studied in the context of magnetorheology. The emergent 3D particle structures arising from such fields also pose great intrigue for biomedical studies involving cell encapsulation and guided proliferation.

This thesis is organized as follows: Chapter 2 lists the thesis objectives. Chapter 3 presents a theoretical overview of dipolar interactions and the derivation of field and force equations that govern our magnetic system. The Mason number is also discussed, from its origins in electrorheological fluids to our current definition for MR fluids in precession fields. Next, Chapter 4 details our homemade triaxial magnetic field generator that was integral in carrying out all the experimental research in the present work. Chapters 5 through 7 report our findings on MR enhancement through the use of unsteady magnetic fields. First, Chapter 5 proposes using our triaxial device to induce the aggregation of complex particle mesostructures by way of precession and perturbation fields. Chapter 6 goes more into detail of the lateral interactions between chained structures that arise under low angle precession fields. Here, particle-level simulations are presented to supplement the experimental work and further address MR fluid strengthening via chain coalescence and structural reinforcement. Then, Chapter 7 gives a complete analysis of the MR effect for magnetic fields ranging from uniaxial DC to rotational AC fields and an array of precession fields in between. An argument for both chain coarsening and particle compactness is made to explain the MR enhancement witnessed under certain magnetic field configurations. Lastly, Chapter 8 introduces our current investigation into an exciting advancement in tissue engineering - employing unsteady magnetic fields to generate anisotropic magnetic hydrogels for cell regeneration therapies. The conclusions and final remarks can be found in Chapter 9.

References

[1] Schwartz, M. (2008). Smart materials. CRC press.

[2] Martin, J. E., & Snezhko, A. (2013). Driving self-assembly and emergent dynamics in colloidal suspensions by time-dependent magnetic fields. Reports on Progress in Physics, 76(12), 126601.

[3] Nardecchia, S., Jimenez, A., Morillas, J. R., & de Vicente, J. (2021). Synthesis and rheological properties of 3D structured self-healing magnetic hydrogels. Polymer, 218, 123489.

[4] Cerdan, K., Brancart, J., Camacho, G., de Vicente, J., & Van Puyvelde, P. (2023). Self-healing magnetorheological elastomers based on thermoreversible Diels–Alder networks. Smart Materials and Structures, 32(4), 045004.

[5] de Vicente, J., Klingenberg, D. J., & Hidalgo-Alvarez, R. (2011). Magnetorheological fluids: a review. Soft matter, 7(8), 3701-3710.

[6] Morillas, J. R., & de Vicente, J. (2020). Magnetorheology: a review. Soft Matter, 16(42), 9614-9642.

[7] Shahrivar, K., Morillas, J. R., Luengo, Y., Gavilan, H., Morales, P., Bierwisch, C., & de Vicente, J. (2019). Rheological behavior of magnetic colloids in the borderline between ferrofluids and magnetorheological fluids. Journal of Rheology, 63(4), 547-558.

[8] Ramos, J., Klingenberg, D. J., Hidalgo-Alvarez, R., & de Vicente, J. (2011). Steady shear magnetorheology of inverse ferrofluids. Journal of Rheology, 55(1), 127-152.

[9] López-López, M. T., de Vicente, J., González-Caballero, F., & Durán, J. D. G. (2005). Stability of magnetizable colloidal suspensions by addition of oleic acid and silica nanoparticles. Colloids and Surfaces A: Physicochemical and Engineering Aspects, 264(1-3), 75-81.

[10] Liu, Y. D., Choi, H. J., & Choi, S. B. (2012). Controllable fabrication of silica encapsulated soft magnetic microspheres with enhanced oxidation-resistance and their rheology under magnetic field. Colloids and Surfaces A: Physicochemical and Engineering Aspects, 403, 133-138.

[11] Li, W. H., & Zhang, X. Z. (2010). A study of the magnetorheological effect of bimodal particle based magnetorheological elastomers. Smart Materials and Structures, 19(3), 035002.

[12] Morillas, J. R., Bombard, A. J., & de Vicente, J. (2018). Enhancing magnetorheological effect using bimodal suspensions in the single-multidomain limit. Smart Materials and Structures, 27(7), 07LT01.

[13] Sedlacik, M., Pavlínek, V., Vyroubal, R., Peer, P., & Filip, P. (2013). A dimorphic magnetorheological fluid with improved oxidation and chemical stability under oscillatory shear. Smart Materials and Structures, 22(3), 03501

[14] Bombard, A. J., Gonçalves, F. R., Morillas, J. R., & de Vicente, J. (2014). Magnetorheology of dimorphic magnetorheological fluids based on nanofibers. Smart materials and structures, 23(12), 125013.

[15] Klingenberg, D. J., & Zukoski IV, C. F. (1990). Studies on the steady-shear behavior of electrorheological suspensions. Langmuir, 6(1), 15-24.

[16] Ginder, J. M. (2003). Rheology controlled by magnetic fields. Digital Encyclopedia of Applied Physics.

[17] Martin, J. E. (2009). Theory of strong intrinsic mixing of particle suspensions in vortex magnetic fields. Physical Review E, 79(1), 011503.

[18] Martin, J. E., Shea-Rohwer, L., & Solis, K. J. (2009). Strong intrinsic mixing in vortex magnetic fields. Physical Review E, 80(1), 016312.

[19] Donado, F., Sandoval, U., & Carrillo, J. L. (2009). Kinetics of aggregation in non-Brownian magnetic particle dispersions in the presence of perturbations. Physical Review E, 79(1), 011406.

[20] Moctezuma, R. E., Donado, F., & Arauz-Lara, J. L. (2013). Lateral aggregation induced by magnetic perturbations in a magnetorheological fluid based on non-Brownian particles. Physical Review E, 88(3), 032305.

[21] Furst, E. M., & Gast, A. P. (2000). Dynamics and lateral interactions of dipolar chains. Physical Review E, 62(5), 6916.

[22] Bica, I., Liu, Y. D., & Choi, H. J. (2013). Physical characteristics of magnetorheological suspensions and their applications. Journal of Industrial and Engineering Chemistry, 19(2), 394-406.

[23] Ashtiani, M., Hashemabadi, S. H., & Ghaffari, A. (2015). A review on the magnetorheological fluid preparation and stabilization. Journal of magnetism and Magnetic Materials, 374, 716-730.

[24] Ahamed, R., Choi, S. B., & Ferdaus, M. M. (2018). A state of art on magneto-rheological materials and their potential applications. Journal of Intelligent Material Systems and Structures, 29(10), 2051-2095.

[25] Sidpara, A., & Jain, V. K. (2012). Experimental investigations into surface roughness and yield stress in magnetorheological fluid based nano-finishing process. International journal of precision engineering and manufacturing, 13, 855-860.

[26] Liu, J., Flores, G. A., & Sheng, R. (2001). In-vitro investigation of blood embolization in cancer treatment using magnetorheological fluids. Journal of Magnetism and Magnetic Materials, 225(1-2), 209-217.

[27] Pardo, A., Gómez-Florit, M., Barbosa, S., Taboada, P., Domingues, R. M., & Gomes, M. E. (2021). Magnetic nanocomposite hydrogels for tissue engineering: design concepts and remote actuation strategies to control cell fate. ACS nano, 15(1), 175-209.

[28] Demri, N., Dumas, S., Nguyen, M. L., Gropplero, G., Abou-Hassan, A., Descroix, S., & Wilhelm, C. (2022). Remote Magnetic Microengineering and Alignment of Spheroids into 3D Cellular Fibers. Advanced Functional Materials, 32(50), 2204850.

[29] Babu, S., Chen, I., Vedaraman, S., Gerardo-Nava, J., Licht, C., Kittel, Y., ... & De Laporte, L. (2022). How do the Local Physical, Biochemical, and Mechanical Properties of an Injectable Synthetic Anisotropic Hydrogel Affect Oriented Nerve Growth?. Advanced Functional Materials, 2202468.

Chapter 2

Objectives

The main objective of the work presented in this thesis is to determine whether unsteady magnetic fields, particularly precession fields, are capable of enhancing the magnetorheological response beyond what is currently known for traditional uniaxial fields.

Specific objectives within the context of this main goal read as follow:

- To validate the versatility of the triaxial magnetic field generator in its ability to produce a wide range of field configurations using both static and oscillatory field components, and the superposition of the two field types.
- To integrate the triaxial device for both rheometry and videomicroscopy experiments through hardware and software design.
- To study particle aggregation dynamics of our MR fluids via high-speed image capturing for precisely programmed precession fields.
- To measure the rheological response of our MR fluids under configured precession fields.
- To compare the measured yield stress between MR fluids structured under unsteady field configurations and uniaxial DC fields.
- To study selected geometry parameters in particle-level simulations exploring the structural evolution of particle systems under uniaxial DC and precession AC fields, as well as examine these properties in the fracturing case under a simulated shearing flow.
- To study the cluster size of particle aggregates under simulated precession fields and analyze interparticle connectivity as a way to explain structural resistance to deformation.

- To identify the main driving mechanisms for MR enhancement induced by certain unsteady precession fields.
- To explore the use of stepped transition fields to mitigate structure fracturing and segmentation.
- To map out the structural response of MR fluids under precession fields where specified conditions in which magnetic and hydrodynamic forces are balanced according to the Mason number.

The following objectives arose from the success in and our ability to freeze 3D particle structures in a gelling medium and our desire to implement dynamic field control for a biomedical application:

- To optimize a hydrogel formulation for cell viability and for magnetic structuring.
- To develop an experimental method to break the intrinsic isotropic nature of randomly crosslinked polymers in a hydrogel.
- To compare cell growth and proliferation between an anisotropically structured hydrogel and a hydrogel sample without added magnetic particles.

Chapter 3

Theoretical Overview and Background

To understand particle interactions under unsteady magnetic fields, it is first important to appreciate the basics of dipole interactions. This chapter begins with a step-by-step derivation of the field produced by a dipole in Section 3.1. In the following Section 3.1.1 the potential energy of interaction between two dipoles is defined and commented on for a selection of relevant field configurations. In Section 3.1.2 we show another derivation for the field induced magnetic force on a particle. Then, in Section 3.2 we describe the evolution of the nondimensional parameter known as the Mason number, with its origins in sheared electrorheological fluids and its current definition for magnetorheological fluid systems. Finally, Section 3.3 discusses time-varying magnetic fields and their use in structuring MR fluids and other applications.

3.1 Dipole interaction

In the absence of an external magnetic field a MR fluid behaves like a Newtonian fluid, with a relatively low viscosity and randomly dispersed magnetic particles in the carrier fluid. It is only when a field is applied that the particles magnetize and a magnetic dipole moment is induced in the particles which leads to aggregation taking place in the direction of the field lines. Particle structuration increases the viscosity of the system and eventually the fluid exhibits a yield stress that increases with the external field strength – this is known as the MR effect [1]. Although the magnetizable particles are typically of micron-size and consist of multidomains, we can frequently neglect multipole and multibody interactions to simplify our understanding of magnetostatic interactions and consider the particles as point dipoles [2-3].

Magnetic dipoles can be defined in a couple of ways, for example, as a small current loop whose dipole vector is oriented orthogonal to the loop [4]. However, here we have chosen to define a magnetic dipole as a pair of two magnetic charges, $+q_m$ and $-q_m$, with the dipole directed from the negative to the positive charge. The separation distance between these two magnetic charges, l, is taken to be infinitesimally small in the limit where the product $q_m l$ is constant. In Figure 3.1 we place these magnetic charges on the z-axis at a distance $l/2$ on either side of the origin. We aim to define the magnetic field, $\vec{B}$, at some point, P, located at a distance, r, from the origin and situated in the y,z-plane. In this orientation the field vector consists of vector components, $B_z = B\cos\theta$ and $B_y = B\sin\theta$, with each individual field component being the sum of the fields produced by the two equal but oppositely charged magnetic monopoles. Starting with $B_z = B_{z,+q_m} + B_{z,-q_m}$ we can define the sum of two fields for two point charges as follows:

$$B_z = \frac{q_m}{r_1^2}\left(\frac{z-\frac{l}{2}}{r_1}\right) - \frac{q_m}{r_2^2}\left(\frac{z+\frac{l}{2}}{r_2}\right) \tag{3.1a}$$

$$= q_m\left(\frac{z-\frac{1}{2}l}{r_1^3} - \frac{z+\frac{1}{2}l}{r_2^3}\right) \tag{3.1b}$$

where r_1 and r_2 are the respective distances between monopoles $+q_m$ and $-q_m$ and point P:

$$r_1 = \left[y^2 + \left(z - \frac{l}{2}\right)^2\right]^{1/2} \tag{3.2}$$

$$r_2 = \left[y^2 + \left(z + \frac{l}{2}\right)^2\right]^{1/2} \tag{3.3}$$

As mentioned, we are interested in describing this definition of a magnetic dipole for two charges with an infinitesimal small separation distance. In doing so we can first isolate the $1/r_1^3$ term from Eqn. 3.1b neglecting $\mathcal{O}(l^2)$ terms:

$$\frac{1}{r_1^3} = \frac{1}{\left[y^2 + \left(z - \frac{l}{2}\right)^2\right]^{3/2}} \tag{3.4a}$$

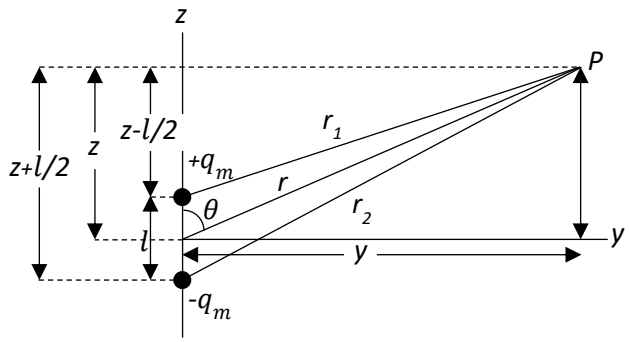

Figure 3.1 Schematic of a dipole constituted of two magnetic charges, $+q_m$ and $-q_m$, and their distances from point, P. All components are situated in the y,z-plane.

$$= \left(\frac{1}{\sqrt{y^2 + z^2 - zl}} \right)^3 \tag{3.4b}$$

$$= \frac{1}{r^3} \left(\frac{1}{\sqrt{1 - \frac{zl}{r^2}}} \right)^3 \tag{3.4c}$$

And by taking the limit of the $1/r_1^3$ term as $l \to 0$ we can rewrite the above term in parenthesis in Eqn. 3.4c as its equivalent Taylor series, or binomial expansion:

$$\lim_{l \to 0} \frac{1}{r_1^3} = \frac{1}{r^3} \left[1 + \frac{zl}{2r^2} + \frac{3}{8} \left(\frac{zl}{r^2} \right)^2 + \cdots \right]^3 \tag{3.5a}$$

$$= \frac{1}{r^3} \left(1 + \frac{3zl}{2r^2} + \frac{3z^2 l^2}{4r^4} + \frac{z^3 l^3}{8r^6} \right) \sim \frac{1}{r^3} \left(1 + \frac{3zl}{2r^2} \right) \tag{3.5b}$$

To simplify this limit we choose to ignore all higher orders of l given that as $l \to 0$ all terms with l^n where $n \geq 2$ rapidly become trivial. Thus, we are left with the following limit of $1/r_1^3$:

$$\lim_{l \to 0} \frac{1}{r_1^3} = \frac{1}{r^3} \left(1 + \frac{3zl}{2r^2} \right) \tag{3.6}$$

Following the same steps we can derive a similar limit of $1/r_2^3$as $l \to 0$:

$$\lim_{l\to 0} \frac{1}{r_2^3} = \frac{1}{r^3}\left(1 - \frac{3zl}{2r^2}\right) \tag{3.7}$$

Now, we can plug Eqn. 3.6 and 3.7 back into Eqn. 3.1b and take the limit as $l \to 0$ and similarly discard the terms with higher orders of l:

$$\lim_{l\to 0} B_z = q_m\left[\left(z - \frac{1}{2}l\right)\frac{1}{r^3}\left(1 + \frac{3zl}{2r^2}\right) - \left(z + \frac{1}{2}l\right)\frac{1}{r^3}\left(1 - \frac{3zl}{2r^2}\right)\right] \tag{3.8a}$$

$$= \frac{q_m l}{r^3}\left(3\frac{z^2}{r^2} - 1\right) \tag{3.8b}$$

We can write Eqn. 3.8b in terms of the magnetic dipole moment $m_1 = q_m l$ and θ, the polar angle between the z-axis and the r vector, to define the field component in the direction of the z-axis:

$$B_z = \frac{m_1}{r^3}(3\cos^2\theta - 1) \tag{3.9}$$

As done for B_z, we similarly begin the derivation for the field component in the y-axis direction by taking the net field as the sum of the fields produced by each of the point charges $B_y = B_{y,+q_m} + B_{y,-q_m}$:

$$B_y = \frac{b}{r_1^2}\left(\frac{y}{r_1}\right) - \frac{b}{r_2^2}\left(\frac{y}{r_2}\right) \tag{3.10a}$$

$$= by\left(\frac{1}{r_1^3} - \frac{1}{r_2^3}\right) \tag{3.10b}$$

Again, we can plug Eqn. 3.6 and 3.7 into Eqn. 3.10b for the $1/r_1^3$ and $1/r_2^3$ terms, respectively, and take the limit of B_y as $l \to 0$:

$$\lim_{l\to 0} B_y = by\left[\frac{1}{r^3}\left(1 + \frac{3zl}{2r^2}\right) - \frac{1}{r^3}\left(1 - \frac{3zl}{2r^2}\right)\right] \tag{3.11a}$$

$$= \frac{3bl}{r^3}\frac{y}{r}\frac{z}{r} \tag{3.11b}$$

Which we then can write in terms of the magnetic dipole moment and θ:

$$B_y = \frac{3m_1}{r^3}\sin\theta\cos\theta \tag{3.12}$$

The total field, $\vec{B}$, at point P would then be the sum of B_z and B_y written below in cartesian coordinates where ϕ would be taken as the azimuthal angle of rotation about the z-axis:

$$\vec{B} = \frac{3m_1}{r^3}\left[\sin\theta\cos\theta\,(\cos\phi\,\hat{\boldsymbol{x}} + \sin\phi\,\hat{\boldsymbol{y}}) + \left(\cos^2\theta - \tfrac{1}{3}\right)\hat{\boldsymbol{z}}\right] \tag{3.13}$$

In order to express the total field in polar coordinates we must convert the unit vectors according to the following trigonometric functions:

$$\begin{bmatrix}\hat{\boldsymbol{x}}\\ \hat{\boldsymbol{y}}\\ \hat{\boldsymbol{z}}\end{bmatrix} = \begin{bmatrix}\sin\theta\cos\phi & \cos\theta\cos\phi & -\sin\phi\\ \sin\theta\sin\phi & \cos\theta\sin\phi & \cos\phi\\ \cos\theta & -\sin\theta & 0\end{bmatrix}\begin{bmatrix}\hat{\boldsymbol{r}}\\ \hat{\boldsymbol{\theta}}\\ \hat{\boldsymbol{\phi}}\end{bmatrix} \tag{3.14}$$

By combining like terms and doing some rearranging, we end up with the following expression of the total field in polar coordinates:

$$\vec{B} = \frac{m_1}{r^3}\left(2\cos\theta\,\hat{\boldsymbol{r}} + \sin\theta\,\hat{\boldsymbol{\theta}}\right) \tag{3.15}$$

Where the dipole is understood to be aligned along the z-axis, $\vec{m}_1 = m_1\hat{\boldsymbol{z}}$. Furthermore, the magnetic dipole moment can be converted to polar coordinates:

$$\vec{m}_1 = m_1\left(\cos\theta\,\hat{\boldsymbol{r}} - \sin\theta\hat{\boldsymbol{\theta}}\right) \tag{3.15}$$

If we scale the above Eqn. 3.15 by $1/r^3$ and add the right hand side to Eqn. 3.15 and subtract the left hand side we would obtain:

$$\vec{B} = \frac{m_1}{r^3}\left(2\cos\theta\,\hat{\boldsymbol{r}} + \sin\theta\,\hat{\boldsymbol{\theta}}\right) + \frac{m_1}{r^3}\left(\cos\theta\,\hat{\boldsymbol{r}} - \sin\theta\hat{\boldsymbol{\theta}}\right) - \frac{\vec{m}_1}{r^3} \tag{3.16a}$$

$$= \frac{1}{r^3}\left(3m_1\cos\theta\,\hat{\boldsymbol{r}} - \vec{m}_1\right) \tag{3.16b}$$

Finally, through the simple dot product relation of the vectors $\vec{m}_1 \cdot \hat{\boldsymbol{r}} = \|\vec{m}_1\|\|\hat{\boldsymbol{r}}\| \cos\theta$, we can rewrite Eqn. 3.16b in a coordinate-free form:

$$\vec{B} = \frac{1}{r^3}[3(\vec{m}_1 \cdot \hat{\boldsymbol{r}})\hat{\boldsymbol{r}} - \vec{m}_1] \tag{3.17}$$

While we carried out this derivation for the field at point *P* under the assumption that the dipole produces a static field oriented in the z-axis, this coordinate-free form of the field equation will be of great use in defining the dipole, or particle, interaction for more complex fields.

3.1.1 Dipole potential and time-averaged interactions

To understand particle interactions under complex triaxial magnetic fields, it is important to first grasp the basics, such as the interaction between two particles in the presence of a static uniaxial field. Traditionally the symbol $\vec{B}$ is representative of the magnetic flux density. Moving forward the magnetic field strength, $\vec{H}$, will be defined as follows:

$$\vec{H} = \frac{1}{4\pi r^3}[3(\vec{m}_1 \cdot \hat{\boldsymbol{r}})\hat{\boldsymbol{r}} - \vec{m}_1] \tag{3.18}$$

Here the field should be considered uniform in space. In keeping with the coordinate orientation of Fig. 3.1, lets now consider that we have two particles, again represented as point dipoles, located at the origin, $\vec{m}_1$, and a second located at point *P*, $\vec{m}_2$. The potential energy $V(r) = \vec{m}_2 \cdot \vec{H}$ then expresses the interaction between the dipoles:

$$V(r) = \frac{3(\vec{m}_1 \cdot \hat{\boldsymbol{r}})(\vec{m}_2 \cdot \hat{\boldsymbol{r}}) - \vec{m}_1 \cdot \vec{m}_2}{4\pi r^3} \tag{3.19}$$

where r is the distance between the dipoles, $\hat{\boldsymbol{r}} = \vec{r}/r$ is the unit vector pointed in the same direction as the line of centers connecting the two dipoles, and $\vec{r} = x\hat{\boldsymbol{x}} + y\hat{\boldsymbol{y}} + z\hat{\boldsymbol{z}}$ is the position vector in cartesian coordinates. An external field polarizes the particles, inducing a dipolar response in the particle's magnetic moment. Given that the particles exist in a non-magnetic medium and the external field is uniform, we can assume the magnetic moments are identical

$\vec{m}_1 = \vec{m}_2 = \vec{m}$ and defined as follows for particles with the form of magnetizable spheres:

$$\vec{m} = \frac{4}{3}\pi a^3 \vec{M} \tag{3.20}$$

where a is the particle radius, $\vec{M} = 3\beta\vec{H}_0$ is the particle magnetization, $\beta = (\mu_p - \mu_c)/(\mu_p + 2\mu_c)$ is the contrast factor, μ_p is the relative permeability of the particle and μ_c is the relative permeability of the continuous phase. These relative permeabilities are the ratio of the absolute permeability of each material component to the permeability of a vacuum, μ_0. The magnetic susceptibility of a particle is incorporated into the contrast factor variable and depends on the particle's material and structure.

First, we would like to consider the simple case of a uniaxial field directed in the z-axis, $\vec{H}_0 = H_z\hat{\boldsymbol{z}}$. In an ideal model the magnetic moments of our two-particle system will similarly direct themselves with the external field and align in the z-axis as well. Of course thermal energy of the system can deflect the alignment from the direction of the external field. However here we choose to assume that $\vec{m} \cdot \vec{H} \gg k_B T$ which corresponds to the complete alignment of the dipoles with the external field.. Now, depending on the location of the particles, or their dipoles, with respect to one another will determine their interaction and whether they are attractive or repulsive. With $\vec{H}_0$ defined as is for a simple uniaxial field, we can plug Eqn. 3.20 into Eqn. 3.19, again noting that the magnetic moments are identical, and solve the potential expression:

$$V(r) = \frac{(4\pi a^3 \beta H_z)^2}{4\pi r^3}(3\cos^2\theta - 1) \tag{3.21}$$

To help map out the particle interaction, we plot the $3\cos^2\theta - 1$ term as a function of θ, as shown in Figure 3.2. Here we see the term is positive for angles $\theta \leq 54.7^{\circ}$ and $\theta > 125.3^{\circ}$, and negative for $54.7^{\circ} < \theta \leq 125.3^{\circ}$. For our definition of the potential energy a positive potential is an attractive interaction, and a negative potential is a repulsive interaction. Also, we choose to discuss the particle orientation in the first quadrant with respect to the positive z-axis knowing that there is symmetry about $\theta = 90^{\circ}$. Therefore, if the particles are positioned in a way such that $\theta \leq 54.7^{\circ}$ the field will induce tip-to-tip deterministic dipolar attraction leading to the formation of a particle dimer [2]. Of course, in a much more concentrated system of particles a

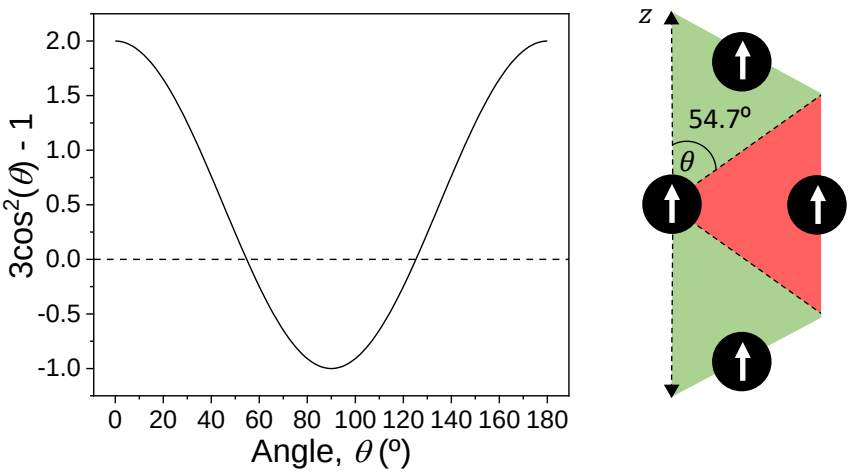

Figure 3.2 The interaction between to dipoles is attractive when the θ dependent term of the potential energy is positive, and repulsive when the term is negative. For a uniaxial field, shown here aligned with the z-axis on the right, a critical angle $\theta = 54.7^{o}$ is the crossover angle from attractive to repulsive interaction.

particle's response would be its net interaction with the dipole moment of every other particle in the system. For a simple uniaxial field configuration this leads to the structuration of chain-like aggregates aligned along the field line direction [5-6]. By introducing unsteady, or time-varying, magnetic fields we can drive more unique aggregate structures [7]. In the following Section 3.2 we will explain the importance of balancing the hydrodynamic and magnetostatic forces to determine a particle's response to an unsteady field configuration. For now, we will focus on two high frequency field configurations that promote the formation of layered structures due to the time-averaged interactions at play.

A 2D rotating field consists of perpendicular oscillating AC fields with a phase difference of 90º, which we define here in the x,y-plane:

$$\vec{H}_0 = H_0(\cos \omega t\, \hat{\boldsymbol{x}} + \sin \omega t\, \hat{\boldsymbol{y}}) \tag{3.22}$$

where $\omega = 2\pi f$ is the angular frequency, and f is the field frequency. For low field frequencies a particle chain will rotate in line with the external field vector. However, as the field frequency increases, the hydrodynamic drag acting on each half chain on either side of the center particle also increases. This leads to an s-like deformation of the chain, which as the field frequency

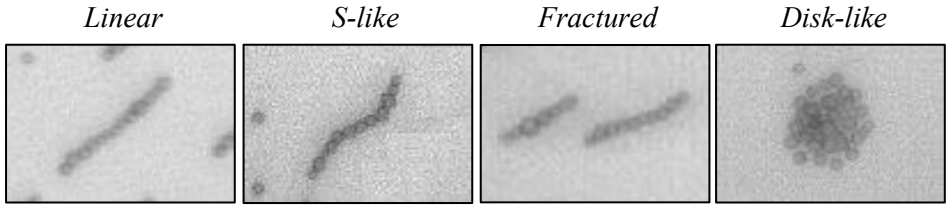

Figure 3.3 A particle chain devolves in a rotating field, from left to right, from a rigid chain to a disk-like aggregate as the rotating field frequency increases. The transition from the s-like form to fracturing is expected to take place at a Mason number around unity where the hydrodynamic drag force and magnetic forces are balanced.

further increases leads to chain fracturing. In general, when we discuss high frequency field configurations this implies $f \to \infty$. For this case a particle chain will lose its chain-like integrity and devolve into a disk-like aggregate that is dominated by the hydrodynamic forces [8]. In Figure 3.3 we show this breakdown of a chain as the field frequency increases.

To explain the disk-like aggregation in dilute suspensions, or layer formation for a more densely populated system of particles, we can incorporate Eqn. 3.22 into Eqn. 3.19 through the magnetic moment, and redefine the potential expression for a rotating field:

$$V(r) = \frac{(4\pi a^3 \beta H_0)^2}{4\pi r^3}[3\sin^2\theta\,(\cos^2\phi\cos^2\omega t + \sin^2\phi\sin^2\omega t + \cos\phi\sin\phi\cos\omega t\sin\omega t) - 1] \tag{3.23}$$

where ϕ is the azimuthal angle about the z-axis. As previously mentioned, disk and layer formation are driven by the time-averaged magnetostatic interactions that take place for high frequency rotating fields [9]. We can take the time-average of Eqn. 3.23 and simplify the expression given that the time-dependent sine and cosine terms converge to zero, and squared time-dependent sine and cosine terms converge to 1/2:

$$\langle V(r)\rangle = \frac{(4\pi a^3 \beta H_0)^2}{4\pi r^3} \cdot -\frac{1}{2}(3\cos^2\theta - 1) \tag{3.24}$$

In comparing Eqn. 3.24 with the potential expression for a uniaxial field aligned with the z-axis (Eqn. 3.21), it becomes clear that the time-averaged potential expression for a high frequency rotating field in the x,y-plane is half the inverse of the uniaxial case. This implies that for angles less than the critical

angle $\theta \leq 54.7^{o}$ the interaction between two dipoles now becomes repulsive, and for angles $\theta > 54.7^{o}$ the dipole interaction is attractive. A cluster of sedimented particles, considered here in the x,y-plane, in the far right panel of Fig. 3.3 thus makes sense given that each particle's dipole would be situated at a polar angle of $\theta = 90^{o}$ with respect to the z-axis (directed out of the page) and the time-averaged interaction is attractive in the x,y-plane. For a more concentrated system, the attractive interaction in the x,y-plane and repulsive interaction in the z-axis direction leads to the formation of layered structures interspersed by particle vacant layers.

Rotating fields are not the only field configuration that can be utilized to form layered particle structures. In experimental practice perturbation fields have been highly effective in promoting layer formation as well [10]. A perturbation field is generated when an oscillatory AC field is directed orthogonal to a uniaxial DC field, defined here in the x,z-plane:

$$\vec{H}_0 = H_x \sin \omega t\, \hat{\boldsymbol{x}} + H_z \hat{\boldsymbol{z}} \tag{3.25}$$

where H_x and H_z are the field amplitude and field strength in the x- and z-axis, respectively. Unlike rotating fields, the resultant field strength of a perturbation field varies with time. For low field frequencies regardless of the angle of perturbation, $\theta_f = \tan^{-1}(H_x/H_z)$, a chain of particles would oscillate back and forth with the external field vector. However, for some high perturbation field configurations we see a similar response to the time-averaged interactions of high-frequency rotating fields. Again, using Eqn. 2.25 we can define the potential expression for a perturbation field as the following:

$$V(r) = \frac{(4\pi a^3 \beta H_0)^2}{4\pi r^3}[3\sin^2\theta\,(\cos^2\phi\cos^2\omega t + \sin^2\phi\sin^2\omega t + \cos\phi\sin\phi\cos\omega t\sin\omega t) - 1] \tag{3.26}$$

Given our interests in modeling the particle interaction under a high frequency perturbation field we similar take the time-averaged approximation of the potential expression:

$$\langle V(r)\rangle = \frac{(4\pi a^3\beta)^2}{4\pi r^3} \cdot \left[-\frac{1}{2}H_x^2(1 - 3\sin^2\theta\cos^2\phi) - H_z^2(1 - 3\cos^2\theta)\right] \tag{3.27}$$

Here the term in brackets on the right hand side is more complex. However, by adjusting the individual field strength components, H_x and H_z, we can pinpoint ideal configurations where $\langle V(r)\rangle$ is mostly positive, or attractive, for dipoles located in the plane of the field ($\phi = 0^o$) and negative, or repulsive, for two dipoles located along the y-axis ($\phi = 90^o$), which would depict the necessary time-averaged interaction required for layer formation. In Chapter 8 we explore using high frequency perturbation fields to form anisotropic layered structures in hydrogels.

3.1.2 Force between two dipoles

Up to this point we have been able to derive the field induced by a pair of magnetic charges, and the potential energy of interaction that arises between two dipoles. Using the same coordinate system as in Section 3.1.1 we have two dipoles $\vec{m}_1$ located at the origin and $\vec{m}_2$ located at some distance r from the origin. Eqn. 3.18 still defines the field, $\vec{H}$, at $\vec{m}_2$ due to the presence of the magnetic dipole at the origin. In the same context we aim to calculate the force acting on dipole $\vec{m}_2$ by taking the gradient of the field to derive the following force equation:

$$F = \mu_0 \vec{m}_2 \cdot \nabla \vec{H} \tag{3.28}$$

In the case of a static external field, we can justify moving $\vec{m}_2$ into the gradient operator and get the same force equation one would derive from the current loop model:

$$F = \mu_0 \nabla\left(\vec{m}_2 \cdot \vec{H}\right) \tag{3.29}$$

Now, we plug Eqn. 3.18 into the above force equation and distribute the gradient operator:

$$F = \mu_0 \nabla\left(\vec{m}_2 \cdot \left(\frac{1}{4\pi r^3}[3(\vec{m}_1 \cdot \hat{\boldsymbol{r}})\hat{\boldsymbol{r}} - \vec{m}_1]\right)\right) \tag{3.30a}$$

$$= \frac{\mu_0}{4\pi} \nabla\left(\frac{3(\vec{m}_1 \cdot \hat{\boldsymbol{r}})(\vec{m}_2 \cdot \hat{\boldsymbol{r}})}{r^3} - \frac{(\vec{m}_1 \cdot \vec{m}_2)}{r^3}\right) \tag{3.30b}$$

$$\begin{aligned} = \frac{\mu_0}{4\pi}\Big[&3(\vec{m}_1 \cdot \hat{\boldsymbol{r}})(\vec{m}_2 \cdot \hat{\boldsymbol{r}})\nabla\frac{1}{r^3} + \frac{3}{r^3}(\vec{m}_2 \cdot \hat{\boldsymbol{r}})\nabla(\vec{m}_1 \cdot \hat{\boldsymbol{r}}) \\ &+ \frac{3}{r^3}(\vec{m}_1 \cdot \hat{\boldsymbol{r}})\nabla(\vec{m}_2 \cdot \hat{\boldsymbol{r}}) - (\vec{m}_1 \cdot \vec{m}_2)\nabla\frac{1}{r^3}\Big] \end{aligned} \tag{3.30c}$$

At present Eqn. 3.30c is still written in a coordinate-free form. However, we can now carry out the gradient operator as the partial derivative with respect to the Cartesian coordinates in vector form, beginning with the first term in brackets of Eqn. 3.30c:

$$3(\vec{m}_1 \cdot \hat{\boldsymbol{r}})(\vec{m}_2 \cdot \hat{\boldsymbol{r}})\nabla\frac{1}{r^3} = 3(\vec{m}_1 \cdot \hat{\boldsymbol{r}})(\vec{m}_2 \cdot \hat{\boldsymbol{r}})\left[\frac{-3}{r^4}\begin{pmatrix} x/r \\ y/r \\ z/r \end{pmatrix}\right] \tag{3.31}$$

Performing the gradient operator on the second and third term in brackets of Eqn. 3.30c is a little more complicated. The unit vector $\hat{\boldsymbol{r}}$ can be written as a function of the position vector $\hat{\boldsymbol{r}} = \vec{r}/r$. Then, the partial derivative can be performed on the position vector with respect to each of coordinate variables, simplifying to a vector of the direction vectors:

$$\frac{3}{r^3}(\vec{m}_2 \cdot \hat{\boldsymbol{r}})\nabla(\vec{m}_1 \cdot \hat{\boldsymbol{r}}) = \frac{3}{r^3}(\vec{m}_2 \cdot \hat{\boldsymbol{r}})\nabla\left((\vec{m}_1 \cdot \vec{r})\,\frac{1}{r}\right) \tag{3.32a}$$

$$= \frac{3}{r^3}(\vec{m}_2 \cdot \hat{\boldsymbol{r}})\left[(\vec{m}_1 \cdot \vec{r})\nabla\frac{1}{r} + \frac{1}{r}\nabla(\vec{m}_1 \cdot \vec{r})\right] \tag{3.32b}$$

$$= \frac{3}{r^3}(\vec{m}_2 \cdot \hat{\boldsymbol{r}})\left[(\vec{m}_1 \cdot \vec{r})\left(-\frac{1}{r^2}\begin{pmatrix} x/r \\ y/r \\ z/r \end{pmatrix}\right) + \frac{1}{r}\left(\vec{m}_1 \cdot \begin{pmatrix} \partial/\partial x\,(x\hat{\boldsymbol{x}} + y\hat{\boldsymbol{y}} + z\hat{\boldsymbol{z}}) \\ \partial/\partial y\,(x\hat{\boldsymbol{x}} + y\hat{\boldsymbol{y}} + z\hat{\boldsymbol{z}}) \\ \partial/\partial z\,(x\hat{\boldsymbol{x}} + y\hat{\boldsymbol{y}} + z\hat{\boldsymbol{z}}) \end{pmatrix}\right)\right] \tag{3.32c}$$

$$= \frac{3}{r^3}(\vec{m}_2 \cdot \hat{\boldsymbol{r}})\left[(\vec{m}_1 \cdot \vec{r})\left(-\frac{1}{r^2}\begin{pmatrix} x/r \\ y/r \\ z/r \end{pmatrix}\right) + \frac{1}{r}\left(\vec{m}_1 \cdot \begin{pmatrix} \hat{\boldsymbol{x}} \\ \hat{\boldsymbol{y}} \\ \hat{\boldsymbol{z}} \end{pmatrix}\right)\right] \tag{3.32d}$$

The third term follows the same steps as carried out above:

$$\frac{3}{r^3}(\vec{m}_1 \cdot \hat{\boldsymbol{r}})\nabla(\vec{m}_2 \cdot \hat{\boldsymbol{r}}) = \frac{3}{r^3}(\vec{m}_1 \cdot \hat{\boldsymbol{r}})\left[(\vec{m}_2 \cdot \vec{r})\left(-\frac{1}{r^2}\begin{pmatrix} x/r \\ y/r \\ z/r \end{pmatrix}\right) + \frac{1}{r}\left(\vec{m}_2 \cdot \begin{pmatrix} \hat{\boldsymbol{x}} \\ \hat{\boldsymbol{y}} \\ \hat{\boldsymbol{z}} \end{pmatrix}\right)\right] \tag{3.33}$$

Finally, the fourth term of Eqn. 3.30c gives the following:

$$-(\vec{m}_1 \cdot \vec{m}_2)\nabla\frac{1}{r^3} = -(\vec{m}_1 \cdot \vec{m}_2)\left[-\frac{3}{r^4}\begin{pmatrix} x/r \\ y/r \\ z/r \end{pmatrix}\right] \tag{3.34}$$

To simplify the force equation, we can represent the coordinate vector and the vector of direction vectors as w and $\hat{w}$, respectively. Thus, in recombining all the terms and organizing the expression, the force acting on $\vec{m}_2$ written as a Cartesian component gives:

$$C^{-1}F_w = -\frac{w}{r}[5(\vec{m}_1 \cdot \hat{\boldsymbol{r}})(\vec{m}_2 \cdot \hat{\boldsymbol{r}}) - \vec{m}_1 \cdot \vec{m}_2] + (\vec{m}_1 \cdot \hat{\boldsymbol{w}})(\vec{m}_2 \cdot \hat{\boldsymbol{r}}) + (\vec{m}_1 \cdot \hat{\boldsymbol{r}})(\vec{m}_2 \cdot \hat{\boldsymbol{w}}) \tag{3.35}$$

Where $C = 3\mu_0/4\pi r^4$ is a shared prefactor. Again, we can further simplify this expression in the case of a uniform magnetic field where the two magnetic dipole moments are equal:

$$f_c^{-1}F_w = -\frac{w}{r}\left[5\frac{(\vec{m} \cdot \hat{\boldsymbol{r}})^2}{\vec{m}^2} - 1\right] + 2\frac{m_w(\vec{m} \cdot \hat{\boldsymbol{r}})}{\vec{m}^2} \tag{3.36}$$

Here $f_c = 3\mu_0\vec{m}^2/4\pi r^4$ is the force prefactor, which we will see in the following section is a key component of the Mason number calculation for a precession field. With Eqn. 3.36 we have derived the force acting on $\vec{m}_2$ as presented in Martin (2009) [11].

In Chapter 6 we go into more detail of force interaction between particles for particle-level simulations modeled under the mean magnetization

approximation in the linear magnetization regime [12]. We will see how the hydrodynamic forces and hard sphere repulsion forces are also involved in the time evolution of simulated magnetized particles [13].

3.2 The Mason number

In the previous Section 3.1.1 we discussed the transition from polarized dipolar interactions to time-averaged interactions in general terms of the field frequency, with high frequencies $f \gg 1$ s^{-1} required to induce the formation of disks or layered structures. However, a magnetized particle's response to a time-varying field or imposed shear is not solely emblematic of the field frequency or shear rate. For MR fluids, the fluid viscosity and field strength also largely determine a particles response, with also the relative permeability of the particle material and particle susceptibility to be magnetized playing a role. For this reason, a nondimensional number, coined the Mason number, was implemented to characterize the relation between hydrodynamic and polarizing forces and how they describe a particle's behavior [14].

At the time Mason *et al.* worked with electrorheological (ER) fluids [15-17]. These fluids respond in a similar manner to MR fluids, but in the presence of an electric field. Typically, an ER fluid sample is placed between two electrode plates, so that when a potential is applied, an electric field is generated in the direction perpendicular to the plates. In the idealized electrostatic polarization model dielectric spherical particles suspended in an insulating continuous phase (low conductivity and large dielectric breakdown strength) form chains structured in line with the electric field giving structure to the system [18]. An increase in the ER fluid's viscosity and the appearance of a shear yield stress exemplifies the so-called ER effect [19]. The magnitude of electrostatic polarization force is defined as follows:

$$F^E = 12\pi\varepsilon_0\varepsilon_c a^2 \beta_E^2 E^2 \tag{3.37}$$

where ε_0 and ε_c are the dielectric constants of the particles and the suspending medium, respectively, β_E is the polarizability of the particles, and E is the strength of the electric field. Similar to how MR fluids respond to an external uniaxial field, an electric field induces an electric dipole moment in the dielectric particles that drives particle chain alignment due to the attractive electrostatic interaction forces. The hydrodynamic force thus acting on a

spherical particle as it moves through the viscous suspending carrier fluid can be represented by Stokes' drag force:

$$F^H = 6\pi\eta a v \tag{3.38}$$

Here v is the viscosity of the particle, whose definition changes depending on the experimental setup whether it be a sheared system or time-varying external field that provokes the fluid or particle movement. The most simple study of these fluids properties and their response under deformation is to shear the fluid in a direction orthogonal to the external field, as is the case in a rheometry experimental setup [20]. In Figure 3.4a the shear is shown as unidirectional by the movement of the upper boundary. A particle's velocity is a function of its position with respect to the moving boundary, or more simply represented as being proportional to the particle size and shear rate, $v(z) \sim a\dot{\gamma}$. Incorporating this relation into Eqn. 3.38 the hydrodynamic drag force acting on a suspension of particles under unidirectional shear can be written as:

$$F^H = 6\pi\eta a^2\dot{\gamma} \tag{3.39}$$

By directly comparing the hydrodynamic force (Eqn. 3.39) to the electrostatic polarization force (Eqn. 3.37), we define the Mn for a structured ER fluid under shear [21]:

$$\mathrm{Mn} = \frac{F^H}{F^E} = \frac{\eta\dot{\gamma}}{2\varepsilon_0\varepsilon_c\beta_E^2 E^2} \tag{3.40}$$

Naturally, we can directly substitute the electrostatic variables in Eqn. 3.40 for their corresponding magnetostatic variables to define the Mn for a structured MR fluid under shear [22]:

$$\mathrm{Mn} = \frac{\eta\dot{\gamma}}{2\mu_0\mu_c\beta^2 H^2} \tag{3.41}$$

The field strength H in Fig. 3.4a is similarly directed in the vertical z-axis as in the ER case. The Mn can also be written in terms of the particle magnetization $\mathrm{Mn} = 9\eta\dot{\gamma}/2\mu_0\mu_c M^2$ through the relation $M = 3\beta H$. Shearing magnetic suspensions subjected to uniaxial DC magnetic fields beyond a critical Mn is also known to induce unique aggregation dynamics in the formation of banded structures [23].

There are a number of advantageous reasons to characterize the behavior of a MR fluid through the Mn, in that it conveniently portrays the MR fluid's viscosity dependence not solely on the shear rate but the applied field strength as well. Both ER and MR suspensions under continuous shear can be described by the Bingham plastic model [14]:

$$\tau = \tau_0 + \eta_\infty \dot{\gamma} \tag{3.42}$$

where τ is the shear stress, τ_0 is the yield stress, and η_∞ is the high shear rate viscosity. It has been shown in the literature that the reduced viscosity can be written in terms of the Mn given the understanding that the yield stress scales with the field strength squared [1,14]:

$$\frac{\eta}{\eta_\infty} = 1 + \frac{\mathrm{Mn}^*(\phi)}{\mathrm{Mn}} \tag{3.43}$$

Where $\mathrm{Mn}^* = 9\tau_0/2\mu_0\mu_c M^2 \cdot \eta/\eta_\infty(\phi)$ is the critical Mason number value that defines the suspension transition between magnetic and hydrodynamic control. Notably, given that the yield stress scales with the field strength squared the ratio τ_0/M^2 becomes independent of the magnetization (or field strength) thus leaving Mn^* solely dependent on the particle volume fraction. Through this relation, viscosity data for a sheared MR (or ER) fluid can be collapsed onto a single master plot when presented as a function of the Mn. Moreover, it is shown that for more concentrated MR fluids where multipolar interactions are expected to contribute to the magnetostatic interaction force, where F^M (see denominator of Eqn. 3.41) does not appropriately take into consideration multipolar interactions, Eqn. 3.43 still holds true and is solely volume fraction dependent [24]. Finite element method (FEM) simulations have corroborated Mn^* dependence on ϕ even in the nonlinear case [25].

However, direct substitution of the magnetostatic variables used to define the Mn in Eqn. 3.41 may not necessarily always hold true in collapsing viscosity data. Klingenberg *et al.* walk through several ways to more accurately describe the magnetostatic response of MR suspensions [21]. For example, nonlinear particle magnetization can occur for high field strengths as the particle magnetization approaches its saturation, M_s. The particle contrast factor $\beta = (\mu_p - \mu_c)/(\mu_p + 2\mu_c)$ can then be written as a function of the field strength:

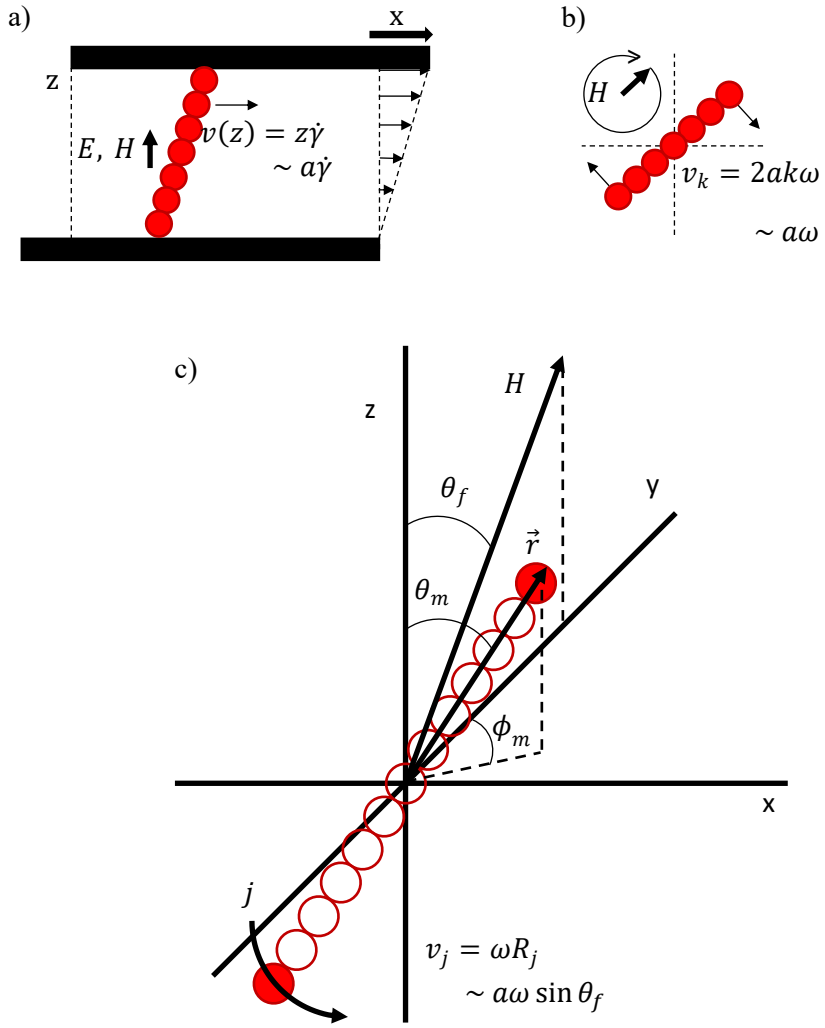

Figure 3.4 Hydrodynamic drag acting a particle chain model can be induced by applied shear or through time-varying magnetic fields. We show that a particles velocity scales with a) $\sim a\dot{\gamma}$ for unidirectional shear, b) $\sim a\omega$ for a rotating field, and c) $\sim a\omega \sin\theta_f$ for a precession field.

$$\beta(H) = \frac{\mu_p(H) - \mu_c}{\mu_p(H) + 2\mu_c} \tag{3.44}$$

With the relative permeability of the particle material being:

$$\mu_p(H) = 1 + \frac{(\mu^0 - 1)\, M_s/H}{(\mu^0 - 1) + M_s/H} \tag{3.45}$$

Here $\mu^0 = 10^3$. This is one way to account for nonlinear particle magnetization in plugging Eqn. 3.44 into Eqn. 3.41 to address the Mn dependence on field strength in the high field strength regime. In the context of the work presented in the following chapters, we work with relatively low magnetic field strengths well within the linear region of the magnetization curves and therefore these corrections to the Mn were regarded as unnecessary.

Continuing the discussion for field induced hydrodynamic drag, Fig. 3.4b shows the particle velocity scales with the angular frequency for a chain in a rotational field (Eqn. 3.22). We can define another Mn comparing the hydrodynamic forces acting on a particle in a rotating field by substituting the angular frequency, ω, into Eqn. 3.41 [22]:

$$\mathrm{Mn} = \frac{\eta\omega}{2\mu_0\mu_c\beta^2H^2} \tag{3.46}$$

In practice, it has been reported by Melle *et al.* that the above Mn multiplied by a factor of 32 more accurately interprets their experimental work, giving the following nondimensional expression in terms of the magnetization [22,26]:

$$\mathrm{Mn} = \frac{12^2\eta\omega}{\mu_0M^2} \tag{3.47}$$

Additionally, one can derive this Mn expression for a rotating field by using the force prefactor f_c from Eqn. 3.36 as the magnetic force component F^H in the Mn calculation. A similar derivation is shown in Chapter 7 for a precession field.

In circling back to Fig. 3.3, we can now explain a chain's deformation in a rotating field by means of the Mn. For a low Mn (low field frequency, low viscosity, high field strength) the magnetic forces at play will dominate the hydrodynamic forces, allowing a particle chain to rotate with the external field with a minimal phase difference. However as the Mn increases (high field frequency, high viscosity, low field strength) the hydrodynamic forces begin a play a more crucial role in a chain's behavior. As the Mn approaches unity, meaning a scenario where the magnetic and hydrodynamic forces are more or less balanced, the particle chain deforms into an s-like shape and will then fracture near the center of mass creating two small chains of equal size, thus reducing hydrodynamic drag acting on each half chain. As the Mn further

increases each half chain will continue fractioning until not even doublets remain intact. In this high Mn regime Mn $\gg 1$ the previously discussed time-average magnetostatic interaction drive disk-like aggregate formation. By looking at a chain model's response through the lens of the Mn we can appreciate the other parameters such as the fluid viscosity and field strength, in addition to the field frequency, that factor into the aggregation dynamics and can each be individually adjusted.

Lastly, Fig. 3.4c illustrates the field and chain vectors for a precession field:

$$\vec{H}_0 = H_z\,\hat{\boldsymbol{z}} + H_{x,y}[\sin(\omega t)\hat{\boldsymbol{x}} + \cos(\omega t)\hat{\boldsymbol{y}}] \tag{3.48}$$

which shown here consists of a uniaxial field in the z-axis superimposed with a rotational field in the x,y-plane. Here the resultant field strength of the individual field components is constant with time and can be calculated as follows:

$$H_0 = \left({H_z}^2 + {H_{x,y}}^2\right)^{1/2} \tag{3.49}$$

With the angle of precession with respect to the vertical z-axis being:

$$\theta_f = \tan^{-1}\left(H_{x,y}/H_z\right) \tag{3.50}$$

In the case of a precession field, it is important to consider the precession angle for the Mn calculation. In a precession field the hydrodynamic drag acting on, for example, the particles at the chain's extremities, is proportional to the distance between the particle and the lateral axis that coincides with the uniaxial field component. Therefore, intuitively a chain moving in a precession motion with a low angle of precession will experience far less hydrodynamic drag than a chain moving in a rotating field (a rotating field here is equivalent to a precession field with a precession angle of $\theta_f = 90^o$). Thus, it was deemed necessary to define a new Mn for precession fields whose particle velocity scales as $\propto a\omega \sin\theta_f$ [27]:

$$\mathrm{Mn} = \frac{12^2\eta\omega\sin\theta_f}{\mu_0 M^2} \tag{3.51}$$

The structural evolution of a MR fluid in the presence of precession field we will see highly depends on both the Mn and θ_f. This Mn definition will be

crucial for the experimental design and analysis employed throughout the following chapters.

3.3 Particle structuring using time-varying fields and their applications

James E. Martin has perhaps most prominently explored the emergent dynamics seen in MR fluids under time-varying magnetic fields in their research [7]. Exploring first uniaxial and biaxial rotating fields, he then continued his research on balanced triaxial fields and was able to produce new and unexpected structures and vortices in a MR fluid that otherwise previously was not possible using more simple field control. As discussed, a triaxial field is generated by a uniaxial DC field applied in one axis while a biaxial field is applied in the orthogonal plane. A balanced triaxial field would require that each axis induces the same field strength of root-mean square amplitude. In studying the stability of particle structures under these fields, Martin found time-evolving molecular-like particle clusters fall into a local energy minimum corresponding to a metastable state. In the case of hexagonally packed layered sheet-like structures, despite calculating an energy reduction for stacked sheets, both simulations and experimental work showed a preference for single particle width layers due to the time-averaged magnetostatic interactions driving the particle structuration [28-29].

Martin refers to aggregate structuring due to dipolar or time-averaged interactions as dynamic and static assembly, respectively. He also defines a quasistatic assembly under time-varying triaxial field configurations of nearly commensurate field frequencies (even as small a difference as a few tenths of a Hertz), such that particle assemblies follow the heterodyne beats between field components [29]. Heterodyning the component fields as well as field biasing are the key to structuring intricate and unique three-dimensional designs, including porous structures, particle foams, sheetlike structures, and cellular structures with deep pores. In heterodyning field components, the resultant instantaneous field magnitude and direction changes slowly compared to the response time of the particle dispersion. This leads to a dramatic response in the colloidal suspension to the heterodyne beat. A beat in this context is an oscillation between coherent and incoherent interactions. Given the time evolution of the field magnitude and direction for these configurations, it is no surprise that the structural response likewise evolves

consistently leading to aggregate formation and fracturing unless the interaction is slowed down by gelling of the carrier fluid [7]. Field biasing is important in heterodyne fielding to give anisotropic properties to the particle structuring. Here, two of the three field components are heterodyned and a uniaxial DC field is applied in the non-heterodyned direction inducing anisotropy and enhancing the composite properties in that axis.

In fact, one of the greatest benefits of anisotropic particle structuring is the enhanced Laplacian properties. By solidifying their structured (and unstructured) carbonyl iron suspensions in an epoxy resin, Martin *et al.* were able to subsequently study various Laplacian properties. In general, a random dispersion of magnetic particles displays a moderate magnetic susceptibility with neither axis direction favored. However, a uniaxial field, say in the z-axis, applied prior to sample gelling resulted in an effective magnetic susceptibility in the axis of the applied field [28]. Similarly for layered particle sheets structured by a biaxial field in the x,y-plane, an appreciable increase in the magnetic susceptibility was measured in the x,y-axes, and was suppressed in the direction normal to the layered sheets (the z-axis) [28]. Composites formed in a balanced triaxial field, on the other hand, showed enhancement in all three coordinate directions [30]. Analogous experiments on the thermal conductivity of these composites showed comparable results indicating that the anisotropic alignment of particles facilitates thermal transport as well [31]. Oriented field structuring is also known to increase the ohmic contacts between neighboring particles, with contacts immensely rising during the subsequent curing stage of gelling due to the composite compression that takes place [7]. These enhanced electrical conductivity properties make structured composites practical as chemical sensors [32]. For example, if the surrounding gelled polymer is designed with an affinity for some predetermined chemical, polymer swelling will thus decrease the number of ohmic contacts and cause a reduction in electrical conductivity.

Another application of precession-like balanced triaxial fields are their use in inducing vortex mixing in MR fluids [33]. Strong mixing occurs for low $\mathrm{Mn} < 0.02$ where the magnetic forces dominate the hydrodynamic forces and chain formation is possible. For field components of balanced root-mean square amplitude, chains move in a precession motion about the critical precession angle $\theta_f = 54.7^{\circ}$ from the axis of the DC field component. Chain size, N, is inversely proportional to the Mn meaning $N \propto H_0/\eta f$. As chain size grows, so does the lag of the chain vector behind the field vector, which in turn

induces the torque needed for mixing to take place. This is the azimuthal angle depicted as ϕ_m in Fig. 3.4c. A prime advantage of vortex mixing in a system of suspended magnetic particles is the ability to homogenously mix the entire sample volume. Vortex fields therefore have the potential to alleviate densely packed or jammed MR fluids. In the literature it is also shown that rotating particle chains situated at the convergence of two microfluidic fluid streams were able to increase the effective mixing at the site [34]. Vortex mixing has typically been studied using spherical magnetic particles. Non-spherical particles such as platelet particles are not ideal for vortex mixing due to an increase probability of particle sedimentation. However, platelet particles are special on their own right.

Solis and Martin investigated the novel use of platelet particles in suspension to create functional fluid flows for heat and mass transfer, known as isothermal magnetic advection [35-36]. In a time-dependent field, the platelets continuously re-orient so that the local field vector lies in the platelet plane and thus reducing the magnetostatic energy. In other words, the platelet director (surface normal) is usually aligned perpendicular to the field. Each particle is subjected to the magnetostatic interactions and torque of neighboring platelets as well as the torque derived from the externally applied field. This field-driven motion coupled with the hydrodynamics of the system is what causes the unique flow pattern and fluid convection and where the heat and mass transfer suspension dynamics arise from. The flow patterns can take the form of rotational flows or diamond lattices depending on adjusting the strength and frequency of the field orthogonal to the biaxial field [37].

Continuing, interesting surface structures can appear when exposed to time-varying fields if the magnetic particles are fixed to a liquid-air or liquid-liquid interface [38-40]. When an orthogonal DC field is applied to suspended particles in a liquid-air interface, the particles are repulsed and form a 2D lattice of separate particles. However, an AC field results in the particles rotating to align with the field and this movement causes a hydrodynamic drag on the fluids surface producing surface oscillations that propagate to other neighboring particles. Effective attraction leads to chain formation with the magnetic moments of the particles being aligned along the chain rather than in the vertical direction. In these experiments it is essential to work with magnetically hard particles that bear a magnetic remanence. This aggregation dynamic leads to the formation of snake-like structures at the liquid-air interface [39]. The size of the snake-like structures depends on the frequency

of the applied AC field. A higher critical field amplitude is required for snake formation when using higher field frequencies or when there is a lower surface density of particles. By further increasing the field strength and frequency of the field components responsible for forming the snake structures, one can cause instabilities. The snake breaks symmetry of surface flows and in effect become self-propelled swimmers [41].

Furthermore, particles fixed to a liquid-liquid interface similarly respond to an applied AC field orthogonal to the liquid-air surface. However, in this liquid-liquid interface the particles and chains excite interfacial waves that promote radial chain growth since the waves are circular and ultimately form dynamic asters [40]. The clusters have a net zero magnetic moment with individual particle magnetic moments pointing inwards towards the center of the cluster (asters) or pointing outwards (anti-asters). These aster structures can also be propelled along the liquid surface by inducing an in-plane DC field. Asters and anti-asters will propel in opposite directions. Their movement can therefore be controlled by the orientation of the DC field vector, which is greater control than the linear snake magnetic swimmers. Lastly, through intricate control of the aster's structure and movement, these structures can encapsulate a cargo particle and then enclose around it, which could be used for a surface transport application [40].

In conclusion, structuring MR fluids with triaxial fields that drive the formation of chains and sheetlike layers increase the Laplacian properties (permeability, permittivity, thermal conductivity, etc.) in line with the structuring field and suppresses these properties in the direction orthogonal to the structuring field. Moreover, field biasing and heterodyning of magnetic particle suspensions in balanced triaxial fields can lead to the formation of complex three-dimensional structures, for both spherical and platelet particles. Structure formation is also not limited to colloidal suspensions, but liquid-air and liquid-liquid particle suspensions can see snake-like and radial aster cluster formations, respectively. Overall, the wide range of these particle suspensions and the aggregation dynamics therein can be used for a variety of practical purposes such as fluid mixing and heat and mass transfer.

References

[1] De Vicente, J., Klingenberg, D. J., & Hidalgo-Alvarez, R. (2011). Magnetorheological fluids: a review. Soft matter, 7(8), 3701-3710.

[2] Promislow, J. H., Gast, A. P., & Fermigier, M. (1995). Aggregation kinetics of paramagnetic colloidal particles. The Journal of chemical physics, 102(13), 5492-5498.

[3] Morillas, J. R., & de Vicente, J. (2019). On the yield stress in magnetorheological fluids: a direct comparison between 3D simulations and experiments. Composites Part B: Engineering, 160, 626-631.

[4] Yung, K. W., Landecker, P. B., & Villani, D. D. (1970). An analytic solution for the force between two magnetic dipoles. Magnetic and electrical Separation, 9.

[5] Fermigier, M., & Gast, A. P. (1992). Structure evolution in a paramagnetic latex suspension. Journal of colloid and interface science, 154(2), 522-539.

[6] Furst, E. M., & Gast, A. P. (2000). Dynamics and lateral interactions of dipolar chains. Physical Review E, 62(5), 6916.

[7] Martin, J. E., & Snezhko, A. (2013). Driving self-assembly and emergent dynamics in colloidal suspensions by time-dependent magnetic fields. Reports on Progress in Physics, 76(12), 126601.

[8] Melle, S., Calderón, O. G., Rubio, M. A., & Fuller, G. G. (2002). Chain rotational dynamics in MR suspensions. International Journal of Modern Physics B, 16(17n18), 2293-2299.

[9] Martin, J. E., Anderson, R. A., & Tigges, C. P. (1998). Simulation of the athermal coarsening of composites structured by a biaxial field. The Journal of chemical physics, 108(18), 7887-7900.

[10] Terkel, M., & De Vicente, J. (2020). Magnetorheology of exotic magnetic mesostructures generated under triaxial unsteady magnetic fields. Smart Materials and Structures, 30(1), 014005.

[11] Martin, J. E. (2009). Theory of strong intrinsic mixing of particle suspensions in vortex magnetic fields. Physical Review E, 79(1), 011503.

[12] Ruiz-López, J. A., Fernández-Toledano, J. C., Hidalgo-Alvarez, R., & de Vicente, J. (2016). Testing the mean magnetization approximation, dimensionless and scaling numbers in magnetorheology. Soft Matter, 12(5), 1468-1476.

[13] Fernández-Toledano, J. C., Ruiz-López, J. A., Hidalgo-Álvarez, R., & de Vicente, J. (2015). Simulations of polydisperse magnetorheological fluids: A structural and kinetic investigation. Journal of Rheology, 59(2), 475-498.

[14] Marshall, L., Zukoski, C. F., & Goodwin, J. W. (1989). Effects of electric fields on the rheology of non-aqueous concentrated suspensions. Journal of the Chemical Society, Faraday Transactions 1: Physical Chemistry in Condensed Phases, 85(9), 2785-2795.

[15] Chaffey, C. E., & Mason, S. G. (1968). Particle behavior in shear and electric fields: V. effect on suspension viscosity. Journal of Colloid and Interface Science, 27(1), 115-126.

[16] Okagawa, A., Cox, R. G., & Mason, S. G. (1974). Particle behavior in shear and electric fields. VI. The microrheology of rigid spheroids. Journal of Colloid and Interface Science, 47(2), 536-567.

[17] Arp, P. A., & Mason, S. G. (1977). Chains of spheres in shear and electric fields. Colloid and Polymer Science, 255, 1165-1173.

[18] Parthasarathy, M., & Klingenberg, D. J. (1996). Electrorheology: mechanisms and models. Materials Science and Engineering: R: Reports, 17(2), 57-103.

[19] Gast, A. P., & Zukoski, C. F. (1989). Electrorheological fluids as colloidal suspensions. Advances in Colloid and Interface science, 30, 153-202.

[20] Martin, J. E., & Anderson, R. A. (1996). Chain model of electrorheology. The Journal of chemical physics, 104(12), 4814-4827.

[21] Klingenberg, D. J., Ulicny, J. C., & Golden, M. A. (2007). Mason numbers for magnetorheology. Journal of Rheology, 51(5), 883-893.

[22] Melle, S., & Martin, J. E. (2003). Chain model of a magnetorheological suspension in a rotating field. The Journal of chemical physics, 118(21), 9875-9881.

[23] Volkova, O., Bossis, G., Carletto, P., & Cebers, A. (2001). Shear banded structures and nematic to isotropic transition in MR fluids. International Journal of Modern Physics B, 15(06n07), 878-885.

[24] Morillas, J. R. & de Vicente, J. "Physics of Magnetorheological Fluids" in Encyclopedia of Smart Materials, edited by Abdul-Ghani Olabi (Elsevier, Amsterdam, 2022), p. 215-223.

[25] Morillas, J. R., & de Vicente, J. (2019). Yielding behavior of model magnetorheological fluids. Soft Matter, 15(16), 3330-3342.

[26] Melle, S., Calderón, O. G., Fuller, G. G., & Rubio, M. A. (2002). Polarizable particle aggregation under rotating magnetic fields using scattering dichroism. Journal of colloid and interface science, 247(1), 200-209.

[27] Terkel, M., Wright, R., & de Vicente, J. (2023). Magnetorheology in unsteady fields: From uniaxial DC to rotating AC fields. Journal of Rheology, 67(4), 833-833.

[28] Martin, J. E., Venturini, E., Odinek, J., & Anderson, R.S. (2000). Anisotropic magnetism in field-structured composites. Physical Review E, 61(3), 2818.

[29] Martin, J. E., Anderson, R. A., & Williamson, R. L. (2003). Generating strange magnetic and dielectric interactions: Classical molecules and particle foams. The Journal of chemical physics, 118(3), 1557-1570.

[30] Martin, J. E., Venturini, E., Gulley, G. L., & Williamson, J. (2004). Using triaxial magnetic fields to create high susceptibility particle composites. Physical Review E, 69(2), 021508.

[31] Martin, J. E., & Gulley, G. (2009). Field-structured composites for efficient, directed heat transfer. Journal of Applied Physics, 106(8), 084301.

[32] Read, D. H., & Martin, J. E. (2010). Strain-tunable chemiresistor. Analytical chemistry, 82(5), 2150-2154.

[33] Martin, J. E., Shea-Rohwer, L., & Solis, K. J. (2009). Strong intrinsic mixing in vortex magnetic fields. Physical Review E, 80(1), 016312.

[34] Biswal, S. L., & Gast, A. P. (2004). Micromixing with linked chains of paramagnetic particles. Analytical chemistry, 76(21), 6448-6455.

[35] Solis, K. J., & Martin, J. E. (2010). Isothermal Magnetic Advection: Creating functional fluid flows for heat and mass transfer. Applied Physics Letters, 97(3), 034101.

[36] Solis, K. J., & Martin, J. E. (2012). Controlling the column spacing in isothermal magnetic advection to enable tunable heat and mass transfer. Journal of Applied Physics, 112(9), 094912.

[37] Solis, K. J., & Martin, J. E. (2012). Stimulation of vigorous rotational flows and novel flow patterns using triaxial magnetic fields. Soft Matter, 8(48), 11989-11994.

[38] Snezhko, A., Aranson, I. S., & Kwok, W. K. (2006). Dynamic self-assembly of magnetic particles on the fluid interface: Surface-wave-mediated effective magnetic exchange. Physical Review E, 73(4), 041306.

[39] Snezhko, A., Aranson, I. S., & Kwok, W. K. (2006). Surface wave assisted self-assembly of multidomain magnetic structures. Physical review letters, 96(7), 078701.

[40] Snezhko, A., & Aranson, I. S. (2011). Magnetic manipulation of self-assembled colloidal asters. Nature materials, 10(9), 698-703.

[41] Snezhko, A., Belkin, M., Aranson, I. S., & Kwok, W. K. (2009). Self-assembled magnetic surface swimmers. Physical review letters, 102(11), 118103.

Chapter 4

The Triaxial Magnetic Field Generator

Magnetorheological fluids have traditionally been studied under uniaxial fields. Perhaps the most rudimentary field generator would be a permanent magnet. Bringing a magnet in close proximity to a MR fluid sample will certainly be effective in driving particle structuring, and in some cases swift sedimentation due to a field gradient. However, control of the field strength and alignment can be limiting experimentally. For rheometry experiments, a simple coil is the most basic option to generate the magnetic field. By controlling the number of loops of conductive wire and the current intensity running through the coil the resultant field strength can be determined, typically on the order of 10 kA m^{-1} and far from the magnetic saturation regime [1]. Direct (DC) and alternating (AC) currents can be applied to generate static and oscillating fields, respectively. A coil is an effective instrument for magnetic field generation for rheometry experiments given that it can wrap around the upper and lower plates [2-3]. However, to reach larger magnetic field strengths (upwards of 100 kA m^{-1}), special magnetorheometer cells were later designed by implementing electromagnetic circuits. To overcome some of the limitations of traditional torsional rheometer setups, a twin-gap and double-gap were developed to further raise field strength output up to 1.5 T as well as increase the maximum shear rate a full decade to 10,000 s^{-1} without sample loss due to centrifugal forces [1,4].

These cells are generally more enclosed systems, which can inhibit visual inspection of the measured sample. Moreover, we are less concerned with generating field strengths within the saturation regime of our magnetic particles, but rather more concerned with field homogeneity and dynamic field control. As experimental research into MR fluids expanded beyond that of uniaxial fields to unsteady biaxial and triaxial fields, a capable field generator

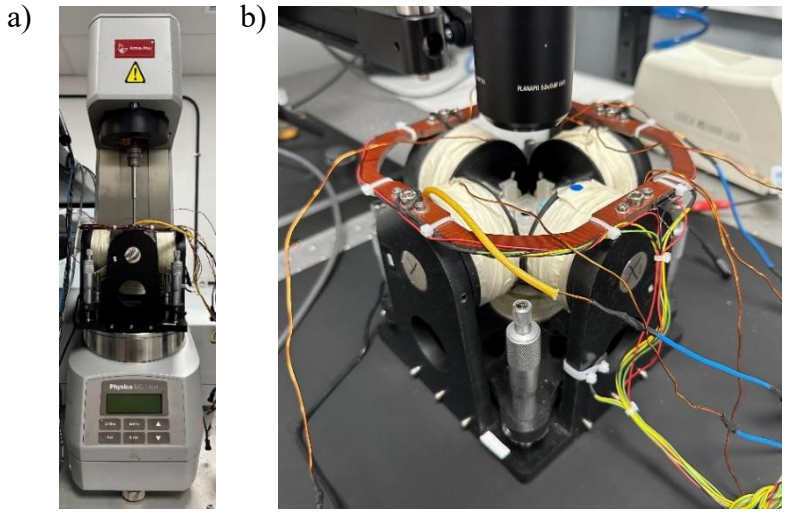

Figure 4.1 The homemade triaxial magnetic field generator was designed to carry out both a) rheometry, and b) videomicroscopy experiments. The device consists of four coils in the x,y-plane and a fifth coil situated beneath that provides the z-axis field component. A triaxial field is generated by inducing the field component in each of the three axes.

was required [5]. Open biaxial and triaxial coils, such as Helmholtz coils, can generate our desired unsteady fields with trusted field homogeneity, although with a considerable loss in field strength output. In order to reach adequate field strengths that bring about a measurable response meeting the threshold of our rheometer, our homemade triaxial magnetic field generator (Figure 4.1) was designed and optimized with mu-metal cores.

4.1 Triaxial hardware

The triaxial magnetic field generator consists of two sets of paired coils in the x- and y-axis, with an additional fifth coil located beneath the x,y-plane that is oriented vertically and generates the z-axis field component. The four coils in the x,y-plane are identical in design (same size, number of loops, distance to sample, etc.) with the z-axis coil being larger to make up for the father working distance between the coil and the center of the sample loading position. The coils are fitted with mu-metal cores to boost their field strength output. Since the loaded sample is not situated inside the coil itself, the mu-metal cores aid in amplifying the field strength felt at the center of the sample loading position. The field component in each axis is independently controlled by three R-L circuits. Each circuit is controlled by its own power supply capable of

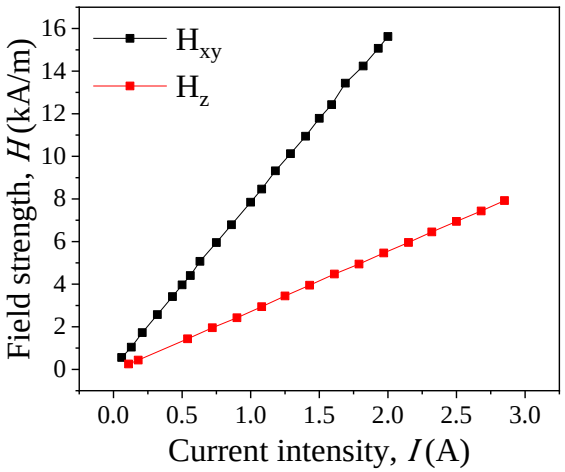

Figure 4.2 The field strength output in each axis is directly proportional to the current intensity running through each coil. The triaxial field strengths were calibrated at the center of the sample holder.

outputting a maximum voltage of 10 V, which can generate a maximum current of around 4 Amperes in the x,y-axis coils and 6.5 Amperes in the z-axis coil. While these current intensities represent the maximum potential of the triaxial generator, we capped the currents to 2 Amperes in all experimental procedures presented in this work to reduce the risk of overheating the field generator.

An extensive calibration went into the design of the hardware for the triaxial magnetic field generator. Using a teslameter (F.W. Bell 5170) we measured the magnetic field strengths of the plots shown in Figure 4.2. Here the field strength (H) in each axis is defined as a function of increasing current intensity (I) in the respective coils:

$$H_{xy}(\text{kA m}^{-1}) = 7.77\, I_{xy}(\text{A}) \tag{4.1}$$

$$H_z(\text{kA m}^{-1}) = 2.80\, I_z(\text{A}) \tag{4.2}$$

The slopes of these H-I curves were used to program the field configurations. For example, for triaxial precession magnetic fields (Eqn. 3.48), the individual field/current components were programmed in such a way that the resultant field strength (Eqn. 3.49) and precession angle (Eqn. 3.50) reflect their desired values.

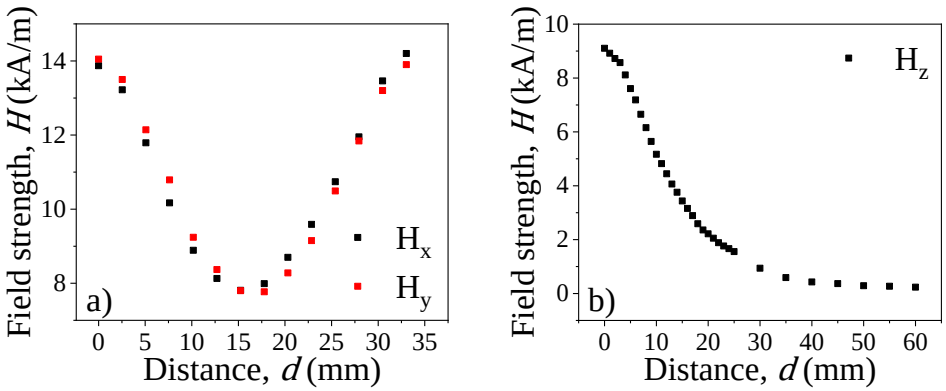

Figure 4.3 Field uniformity is displayed in a) for the x,y-axis along the distance between each paired coil. At the center of the sample holder there is approximately a 10 mm x 10 mm zone of a more homogenously uniform field. In b) the field strength drops farther out from the coil. However, field uniformity in the z-axis is not a concern since sample heights are less than 0.5 mm.

As seen in Fig. 4.1a, the base of the triaxial device was designed such that it can be mounted on top of our MCR501 Anton Paar rheometer. The top of the triaxial device is open to lower the upper geometry (plate-plate) onto the sample for rheometry tests. Similarly, for videomicroscopy experiments a camera is positioned above the triaxial, as shown in Fig. 4.1b. A detailed schematic of the triaxial magnetic field generator for both the rheometry and videomicroscopy experimental setups can be found in Chapter 6 (Fig. 6.1). A small change to the sample holder allows us to install an LED backlit illuminator to increase particle contrast and enhance image capturing.

The uniformity of the field was also studied at the center of triaxial device. In Figure 4.3a we show the uniformity of the field in the x,y-plane along the distance between the two paired coils that make up one axis. In this calibration test a current intensity of 1 Ampere was set in each coil. We see that the field strength is strongest at the coil nucleus (tip of the mu-metal core) and decreases moving away from the coil reaching a minimum at the center position. At the center where the samples are loaded, there is roughly a 10 mm x 10 mm region where the field is more homogenously uniform. For the videomicroscopy experiments carried out in this work, all images were captured from this center region. Fig. 4.3b corresponds to the uniformity of the field in the z-axis. In this case, we see that the field strength continuously decreases farther out from the coil nucleus, since the triaxial generator was designed with only one coil generating the field component oriented in the vertical z-axis direction.

However, this is not an issue as the MR fluid samples loaded into the sample position holder for both rheometry and videomicroscopy experiments typically had a maximum sample height of 500 μm. In general, the uniformity of fields generated by coils can decrease when introducing a core nucleus, albeit with an accompanying increase in the field strength.

4.1.1 Capacitor bank

The oscillating component of time-varying AC magnetic field configurations explored in this work, such as precession and perturbation fields, are controlled by the field frequency, f. This variable we will later see is important in defining the Mn for precession fields, and that in order to carry out an extensive and complete study of MR fluids under a fully encompassing range of field configurations, we required a triaxial field generator able to perform such a task. To do so, three fractal capacitor banks (Figure 4.4) were constructed to operate with each axis of the triaxial device, following the design previously used by Martin [6].

In the absence of a capacitor bank, and solely working with an R-L circuit, for field frequencies $f > 10$ Hz, the current to voltage ratio begins to steadily decrease. In Figure 4.5 we see this drop for both the x,y and z circuits (black dotted curves). In these plots we show the measured current intensities at the maximum voltage $V = 10$ V. On the other hand, in the R-L-C circuit each capacitor bank generates 4905 states in the x,y circuit and 4934 states in the z

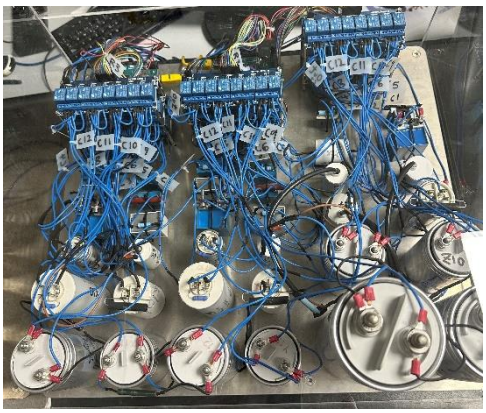

Figure 4.4 Three capacitor banks, consisting of 12 capacitors each, were integrated into an R-L-C circuit in order to generate higher frequency AC fields without drastically diminishing the current to voltage ratio.

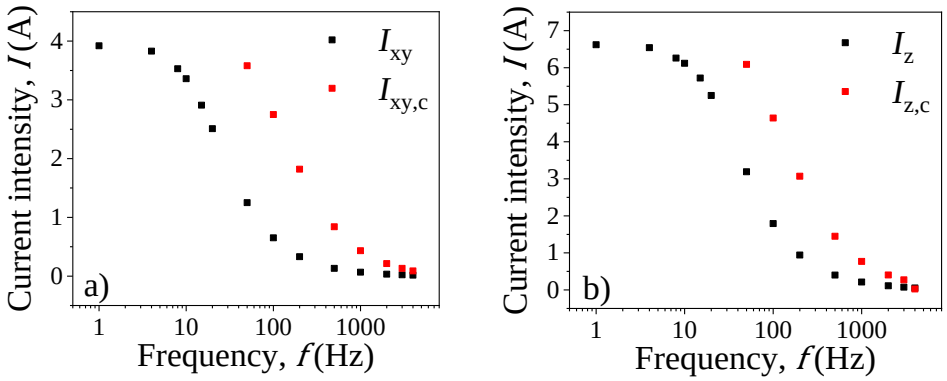

Figure 4.5 At maximum voltage, $V = 10$ V, the current intensity begins to drop at low frequencies for both the a) x,y-axis and b) z-axis. By connecting the circuit to the capacitor bank higher currents can be reached for higher frequencies and this drop is delayed.

circuit to provide a quasi-continuous distribution of capacitance, and thus field frequencies going up to 4 kHz. Each programmed state has an average theoretical resonant frequency about 0.1% greater than the previous state. The red dotted curves in Fig. 4.5 show the measured current intensities, again at $V = 10$ V, for a R-L-C circuit with field frequencies $f > 45$ Hz. By connecting the circuit to the capacitor, the current to voltage drop is now delayed to higher frequencies. By improving the current to voltage ratio we are able to program higher field frequencies while still maintaining desired field strengths.

4.2 Triaxial software

A LabVIEW program was developed to run the triaxial magnetic field generator. The main components to the LabVIEW program interface are highlighted in Figure 4.6. These components are the capacitor bank activation option, field frequency selection, the field configuration box and display window, and the pre-programmed field configuration sequence box.

Both direct and alternating currents can be supplied to each paired coils in the x and y axes and to the z-axis coil of the triaxial device to generate static and oscillating fields. When the capacitor bank is not activated one can switch between supplying DC and AC currents in real time. However, once the capacitor bank is activated (a prompt is given to the user as shown in Fig. 4.6a) in a particular axis for the specified programmed field frequency (the bank is triggered for field frequencies $f > 45$ Hz) the triaxial device will only be able

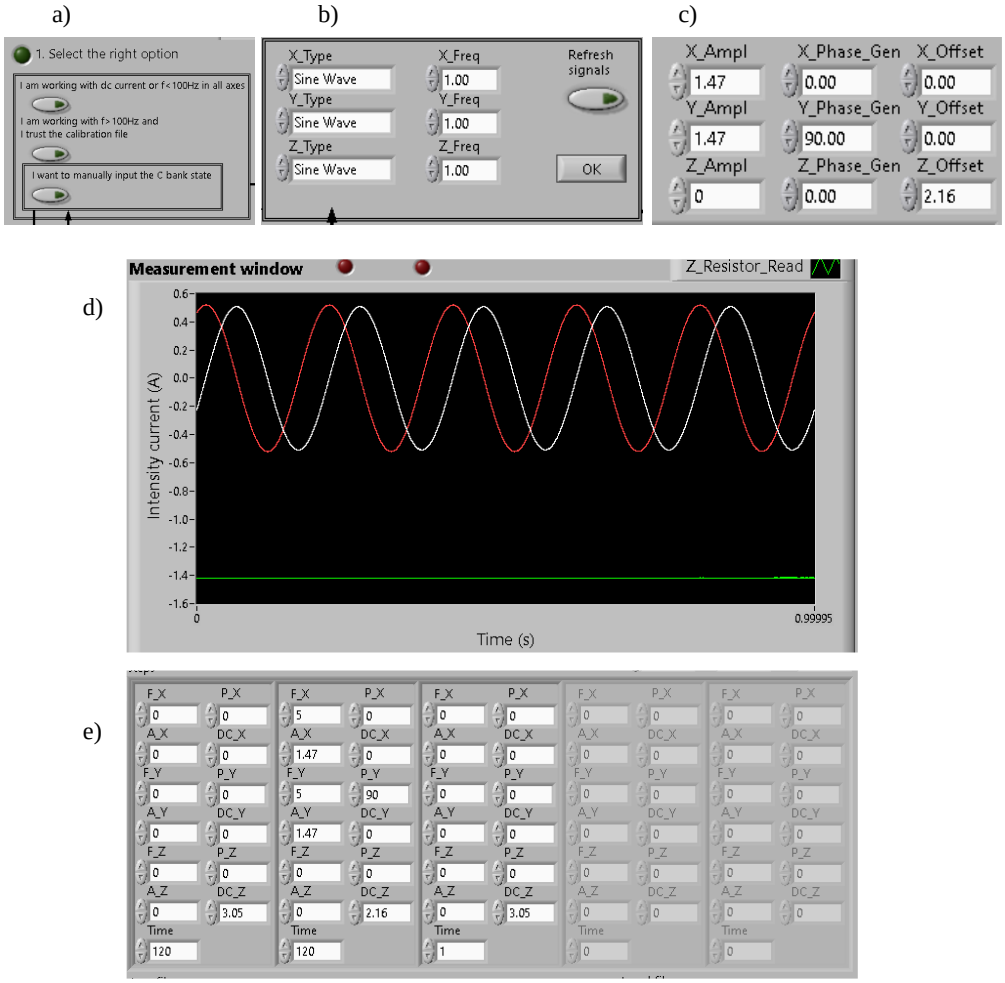

Figure 4.6 The LabVIEW interface. The general operating method consists of first a) choosing to connect the triaxial to the capacitor banks, followed by b) inputting the desired field frequencies and c) field configuration. In d) the current outputs are monitored in the display window. Also, in e) an example three-step field sequence is shown in the pre-programmed field configuration sequence box.

to supply an AC field to the coil(s) at the specified locked in frequency. Only by terminating the LabVIEW program and restarting will the user be able to change the programmed field frequency, opt out of using the triaxial device connected to the capacitor bank, or supply a DC current to the coil(s).

Depending on the experimental protocol and the required field frequencies a choice of connecting the capacitor bank or not is made and then the field frequencies can be inputted (Fig. 4.6b.). Then, the field configuration box (Fig. 4.6c) becomes active. Here, the field amplitude (for AC fields), the phase

difference of one axis' current with respect to the current amplitude of another axis, and an offset value (for DC fields) can be inputted for each of the three field components. This field configuration box also functions in real time when the capacitor bank is not connected, meaning field strengths (both DC offset and AC amplitude values) can be changed while operating. The voltage values shown in Fig. 4.6c correspond to a precession field configuration with current amplitudes in the x,y-plane of $I_{xy} = 0.51$ A and an offset current (DC) in the z-axis of $I_z = 1.42$ A, as are shown in the display window (Fig. 4.6d). First plugging these current values into Eqn. 4.1 and Eqn. 4.2, one can do a quick calculation using Eqn. 3.49 and Eqn. 3.50 to show this programmed field configuration generates a precession field with precession angle $\theta_f = 45^o$ and a resultant field strength of 5.54 kA m^{-1}.

Prior to every experiment the voltage to current ratio is checked as the working conditions of the circuits may change. We can manually measure the voltage to current ratio and adjust the inputted field configuration as needed, or we determine the ratio by implementing a feedback loop feature of the software where the voltage is automatically adjusted until a desired current is found. To maintain experimental consistency, the triaxial field strengths were calibrated as a function of the currents, rather than as a function of the voltage. Also, experimental protocols discussed in this work were designed to prevent a change in the working conditions, such as long experiments or excessive current intensities that could lead to overheating of the coils.

Lastly, another important aspect to the triaxial LabVIEW software was being able to pre-program a sequence of different field configurations that conveniently transitions from one configuration to the next without having to manually change the parameters by hand in real time. Particle structuring in MR fluids is extremely sensitive to the external field. By pre-programming field configurations in sequence, there is no risk of exposing the MR fluid to an undesired intermediate configuration, or a momentary absence of a field that could lead to particle sedimentation, both of which could occur by manual adjustment. Instead, the field transitions smoothly from one configuration to the next in a matter of a few milliseconds via use of the pre-programmed field configurations sequence box. Sequenced field configurations were employed for the typical three-step particle structuration protocols (uniaxial DC + precession AC + uniaxial DC), and especially utilized for the stepped angle transition field experiments discussed in Chapter 7. An example pre-programmed three-step field configuration sequence is shown in Fig. 4.6e. In

each step there are three blocks of four variables related to each of the three axis, followed by the time variable at the bottom. Here the same field configuration from Fig. 4.6c is represented in the second step column sandwiched between two z-axis uniaxial field steps. The offset voltage values $V = 3.05$ V in the z-axis correlate to 2 Amperes, and a field strength of 5.54 kA m^{-1}. The smooth and immediate transition between field configurations programmed in sequence also means maintaining consistent the resultant field strength, which is pivotal for comparing the MR response between precession fields and traditional uniaxial fields.

Overall, our homemade triaxial magnetic field generator has been incredibly essential for the successful realization of the experiments carried out in this work. This original version of the triaxial inspired the development and construction of subsequent models capable of being integrated with more advanced rheometry and microscopy (optical and confocal) experimental setups, which current and future research will undoubtedly benefit from.

References

[1] Morillas, J. R., Yang, J., & de Vicente, J. (2018). Double-gap plate–plate magnetorheology. Journal of Rheology, 62(6), 1485-1494.

[2] Bossis, G., & Lemaire, E. (1991). Yield stresses in magnetic suspensions. Journal of Rheology, 35(7), 1345-1354.

[3] Ginder, J. M. (1998). Behavior of magnetorheological fluids. Mrs Bulletin, 23(8), 26-29.

[4] Laun, H. M., Gabriel, C., & Kieburg, C. (2010). Twin gap magnetorheometer using ferromagnetic steel plates—performance and validation. Journal of Rheology, 54(2), 327-354.

[5] Martin, J. E., Venturini, E., Gulley, G. L., & Williamson, J. (2004). Using triaxial magnetic fields to create high susceptibility particle composites. Physical Review E, 69(2), 021508.

[6] Martin, J. E. (2013). A resonant biaxial Helmholtz coil employing a fractal capacitor bank. Review of Scientific Instruments, 84(9), 094704.

Chapter 5

Magnetorheology of Exotic Magnetic Mesostructures Generated Under Triaxial Unsteady Magnetic Fields

Matthew Terkel and Juan de Vicente

Biocolloid and Fluid Physics Group and Excellence Research Unit 'Modeling Nature' (MNat), Department of Applied Physics, Faculty of Sciences, University of Granada, C/Fuentenueva s/n, 18071 - Granada, Spain

Published in

Smart Materials and Structures
Systems from nano- to macroscale

Smart Mater. Struct. **2020**, 30, 014005
Special Issue: Focus on ERMR 2019

Abstract

Traditionally, the rheological properties of magnetorheological (MR) fluids are investigated under uniaxial steady (DC) fields. These basic fields promote the aggregation of magnetically attractive particles into chain-like structures aligned in the field driven direction. In this manuscript we show how triaxial unsteady fields can generate a variety of exotic mesostructures and influence the rheological response of the MR fluids. We bridge understanding the rheological response to each unique particle structure through videomicroscopy, X-ray microtomography (Micro-CT) and rheometry tests. Small-amplitude oscillatory shear (SAOS) and steady shear tests lay out an unmistakable argument for MR enhancement with both elevated storage modulus and yield stress responses following a sequence of steady uniaxial and unsteady fields. We demonstrate that structures assembled through time-averaged particle interactions or typical dipole-dipole magnetostatic interactions, especially when columnar structures are strengthened through lateral chain coalescence, can boost rheological response.

5.1 Introduction

Magnetorheological (MR) fluids typically consist of magnetic responsive particles suspended in a nonmagnetic fluid. A uniaxial steady (DC) field can increase the viscosity by multiple orders of magnitude due to the formation of field induced structures in the field direction [1-4]. Their ability to rapidly change from a liquid suspension to a solid-like structure when exposed to an external magnetic field has made them popular in mechanical applications. For instance, shock absorbers and dampers benefit from the viscous controllability of MR fluids [5]. Uniaxial DC fields induce dipole interactions between suspended particles motivating over time anisotropic chain growth until a kinetically arrested state is reached. Triaxial unsteady fields, on the other hand, can circumvent this metastable state and further drive particle and chain aggregation into new hopefully strengthened structures. Preliminary studies have shown that triaxial precession fields can boost the rheological response of a fluid compared to the response under uniaxial DC fields without changing the magnetic field strength.

MR fluids have predominantly been studied in uniaxial DC fields [1,6]. Halsey and Toor [7] first calculated the lateral field around an infinite chain of dipoles

and the interaction between two chains. Martin *et al.* [8] extended the Halsey and Toor model to take into consideration the dependence field strength has on suspension coarsening. Fermigier and Gast [9] would later observe lateral chain coalescence through a "zippering" motion takes place when particle concentration is high and the spacing between chains is small. All of these observations agreed that interaction between chains can either be attractive or repulsive depending on whether the center of particles in neighboring chains are in-or out-of-registry with one another. The strong anisotropic interaction between two isolated particles helps us understand the deterministic aggregation process of magnetically responsive colloidal particles and as well as lateral aggregation.

Toggled fields have also been employed to generate novel structures in MR fluids. Promislow and Gast [10,11] showed that when exposing a previously arrested chain network to a toggled field, the particles relax and reconfigure and in addition to particle phase separation a lower energy state is also reached. Tuning the frequency of the on and off states of the toggle period is key to the self-assembly mechanics. A high toggle frequency prevents particle relaxing and the suspension remains arrested, while a low toggle frequency leads to constant particle rearrangement since the off period is sufficiently long for the network to become momentarily disordered. Structural coarsening into condensed domains of both spherical [12,13] and ellipsoidal [14] particles into condensed domains were observed in toggled fields.

Particle assembly can be driven by many different types of field configurations. Structure layer formation driven by the time-averaged magnetostatic interactions often occurs when high component field frequencies are used [15]. In the case that field frequencies slightly vary in biaxial fields, particle assemblies follow the heterodyne beats between field components, and new structures further emerge when a biased DC field is superimposed [16,17]. When it comes to unsteady fields Martin introduced triaxial fields as a means to produce new unexpected structures and vortices in a MR fluid [18,19]. He laid out the criteria for vortex fields and showed that a balanced triaxial field is optimized for mixing when the root means square amplitude of a rotating magnetic field is equal to an orthogonal DC field. Martin only addresses the possibility that these fields can improve the MR response. The work of Donado *et al.* [20] begins to address this topic with preliminary rheometry tests showing that low angle perturbation fields lead to an increase in the fluid viscosity.

In this paper, we present the experimental work done to show a simple way to generate a wide variety of structures superimposing unsteady fields and the enhancement these strengthened structures have on the rheological properties of a MR fluid. We also examine the effect on particle structure of field transitions between uniaxial DC field and unsteady field configurations. In the following section we introduce the relevant theoretical background, including the Mason number, which is fundamental for describing the evolution of a single chain and a collection of chains in the presence of unsteady fields, as it compares the magnetostatic interaction and viscous forces at play. In Section 5.3 we describe the colloidal system and the homemade constructed triaxial device used to generate the triaxial precession fields and biaxial perturbation field employed in the experiments. A specification of the experimental protocol and each unsteady field is also detailed. In Section 5.4 we present the small-amplitude oscillatory shear tests and rheograms performed during the assembly and shear periods of the experimental protocol. We observe that the structures produced in this work were successful in improving the rheological response, as we measured larger storage modulus and yield stress values compared to a uniaxial DC field baseline case.

5.2 Theoretical background

Uniaxial DC fields have been exhaustively studied and we know that magnetic responsive microparticles suspended in a liquid will self-assemble into chain-like structures. A magnetic dipolar moment m is induced in the particles that is aligned with the field, H_0:

$$m = \frac{4}{3}\pi a^3 M \tag{5.1}$$

Here a is the radius of the particle, and M is the particle magnetization $M = \chi H_0$. The magnetic susceptibility is defined as $\chi = 3\beta = 3\left(\mu_{pr} - \mu_{cr}\right)/\left(\mu_{pr} + 2\mu_{cr}\right)$, where μ_{pr} is the relative permeability of the particles, and μ_{cr} is the relative permeability of the continuous phase. For carbonyl iron particles the contrast factor in the linear magnetization regime is of the order of $\beta = 0.65$ [21].

When discussing biaxial rotating chain-like structures under the presence of an external magnetic field, we have the Mason Number (Mn) to define the system.

This dimensionless number compares the magnetostatic interaction forces holding a chain together to the viscous forces acting counteractively to fracture the particle structure. The Mason Number is defined as follows [22]:

$$\mathrm{Mn} = \frac{12^2 \eta \omega}{\mu_0 M^2} \tag{5.2}$$

Here η is the fluid viscosity, ω is the rotational field frequency, and $\mu_0 = 4\pi \times 10^{-7}$ Tm/A is the permeability of a vacuum. For Mn $\ll 1$ a chain will rotate in line with the field vector. However, for increasingly higher Mn the phase lag between the rotating chain and the field vector increases to 90°. At this point the viscous forces acting on the chain dominate the magnetostatic interactions between the chain particles. Overall, a chain will evolve from a linear chain for Mn $\ll 1$ to an S-like shape as the Mn approaches Mn ~ 1 when a single chain will fracture at its center of mass into smaller chains, until ultimately degenerating into a disk-like circular shape for Mn $\gg 1$. Increasing the fluid viscosity and field frequency and decreasing the magnetic field strength are all possible ways to increase the Mn.

In the presence of a triaxial precession magnetic field, $\vec{H}_0 = H_0\{\sin\theta_f[\sin(2\pi f t)\hat{x} + \cos(2\pi f t)\hat{y}] + \cos(\theta_f)\hat{z}\}$, defined here by an alternating field in the x, y-plane and a DC field in the z-axis direction. The field frequency in Eq. 5.2 can be replaced with the angular speed for a precession field $\omega = 2\pi f \theta_f$ giving the following Mn [20]:

$$\mathrm{Mn} = \frac{288\, \eta \pi f \theta_f}{\mu_0 M^2} \tag{5.3}$$

Here θ_f is the angle of precession deviating from the axis of the DC field component. Similar to biaxial rotating fields, a low Mn chain in a precession field will follow in line with the field vector independently of θ_f. At Mn $\gg 1$, however, the angle of precession θ_f is key to determining the resultant structure. There is a critical angle of precession $\theta_{f,crit} = 54.7°$, where below (above) this angle the magnetic dipole moments of particles in a chain remain in the attractive (repulsive) region. As the Mn increases and the phase lag between the chain and the field vector increases, the chain will collapse on the axis of the DC field component of the precession field if $\theta_f < \theta_{f,crit}$.

Alternatively, when the angle of precession is above the critical angle $\theta_f > \theta_{f,crit}$ the magnetic dipole moments of the particles in a chain are repulsive to one another for high Mn. The chain will spontaneously fracture and the individual particles will migrate into layers due to the time-averaged aggregation dynamics.

Another interesting type of unsteady field is a superposition of a steady field and a uniaxial perturbation field orthogonal to the static field, $H = H_s\hat{z} + H_p \sin(2\pi f t)\,\hat{x}$, where H_s is the intensity of the static field component in the z-axis and H_p is the oscillatory perturbation field written here as being in the x-axis to reflect our experiments. Unlike precession fields, biaxial perturbation fields are not constant in strength due to the oscillatory nature of the superposition of H_s and H_p. A maximum angle denoted as the perturbation angle is reached at $\theta_p = \tan^{-1}(H_p/H_s)$. For the purpose of estimating the Mn for perturbation fields, we have chosen to substitute θ_p and H_s into Eq. 5.3 giving us:

$$\mathrm{Mn} = \frac{32\,\eta\pi f \theta_p}{\mu_0 \beta^2 H_s^2} \tag{5.4}$$

It should be noted that in our experiments the static field component of the perturbation field was set to the same strength as the superimposed field strength used when utilizing precession fields, $H_s = H_0$, to maintain a thread of consistency between the two unsteady field types. We had the choice of programming the perturbation field configuration such that the field was equivalent to the superimposed precession field magnitude either at the 0º or maximum angle position, and ultimately chose the former scenario.

Whereas a system of chain-like structures in uniaxial DC fields will stabilize over time, introducing a precession field it is expected to breath new life into chain interaction. In uniaxial DC fields the chain length and thickness is dictated by the particle concentration and field strength employed. Besides these two parameters, precession fields increase the chain-chain magnetostatic interaction needed to further induce lateral chain coalescence beyond the limitations set by traditional uniaxial DC fields. In this manuscript we are less concerned with limiting ourselves to columnar structures and welcome the more exotic structures that arise from unsteady fields and instantaneous field transitions.

5.3 Experimental

5.3.1 Materials

MR fluids investigated in this work were prepared by dispersing carbonyl iron (CI) particles (EW grade from BASF SE Germany) in a 1:1 water/glycerol (99% Fisher chemical) mixture. A centrifugal mixer (Thinky US) was used for 5 minutes to ensure proper particle dispersion. Prior to loading the samples are shaken and sonicated for an additional 2 minutes to guarantee dispersion of particles.

5.3.2 Triaxial magnetic field generator and magnetic field configurations

We used a triaxial magnetic field generator capable of inducing external magnetic fields in three dimensions. The device consists of five coils in total, four situated in the x, y-plane and a fifth larger coil located beneath pointing upwards, which induces the z-axis field. All coils were fitted with a mu-metal core to increase the external field strength induced at the center of the sample platform. Three power sources supply the current through each of the three axis' coils. A capacitor bank has also been integrated to implement unsteady field configurations with high frequencies up to 4 kHz. Additionally, the triaxial magnetic field generator is controlled by a LabView program, which controls the experimental parameters of the magnetic field configuration. The experimental parameters can be pre-programmed in the scenario of having to initiate multiple field configurations in sequence. Lastly, the triaxial device can be fitted with a sample chamber and a backlit illumination setup for videomicroscopy experiments, or a sample platform to do the rheometer tests.

To maintain consistent results between test trials the voltage to current conversion in each coil axis is tested beforehand to adjust and correct for possible coil heating throughout the experimental work day. In the case the coils become slightly heated, the voltage output is increased to account for reduced currents thus bringing the current up to the desired level.

Magnetic fields were superimposed in three steps (see Figure 5.1). In the first stage, a uniaxial DC field is applied to promote directed self-assembly in the field direction. In the second stage, an unsteady magnetic field is applied to rearrange the chain-like aggregates into more exotic structures. Finally, in the

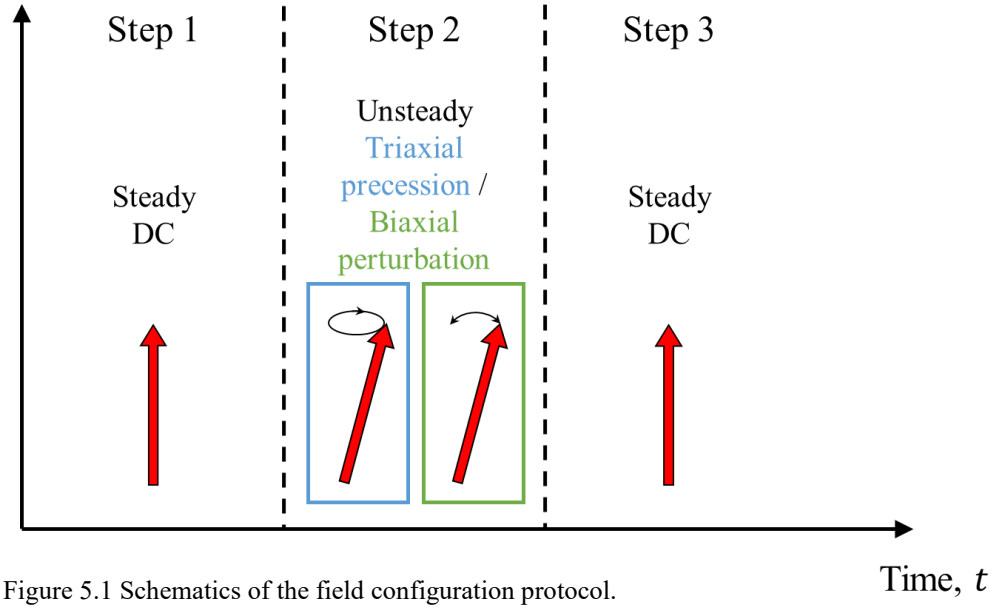

Figure 5.1 Schematics of the field configuration protocol.

third stage a uniaxial DC field is again superimposed to fix the structures. Table 5.1 summarizes all eight distinct magnetic field configurations we studied in this work, and the particular field frequencies and angle of precession or perturbation programmed for each experiment (Exp. #). An emphasis on meticulously programming the field configurations for Exp. 1-6 was fundamental in maintaining constant the magnetic field strength for both the uniaxial DC field and the superimposed precession fields. The purpose of maintaining the field strength is to demonstrate that the rheological response of an MR fluid can be improved solely through structural changes that arise under unsteady magnetic fields without increasing the field strength itself.

Table 5.1 The magnetic field configurations (field frequency and angle of precession or perturbation) used in the second interval of step iii of the experimental protocol. The final structures are the results following the third interval (DC field to reorient the structures in line with the z-axis).

Exp. #	Angle of precession, θ_f (°)	Frequency, f (s^{-1})	Field strength, H_0 (kA m^{-1})	Mn	Structure
1	15	10	5.6	0.14	Fortified columnar structure
2	75	0.01	5.6	0.00068	Segmented structures
3	75	1	5.6	0.068	Dense sheets
4	75	10	5.6	0.68	Less dense sheets
5	75	100	5.6	6.8	Very dense sheets
6[a]	15	1	5.6	0.014	Conical structures
Exp. #	Angle of perturbation, θ_p (°)	Frequency, f (s^{-1})	Field strength, H_s, H_p (kA m^{-1})	Mn	Structure
7	60	0.1	5.6, 9.7	0.0054	Fortified columnar structure
8	60	10	5.6, 9.7	0.54	Vertical layers

[a] 20 min pre-sedimentation period.

5.3.3 Structure imaging techniques

5.3.3.1 Optical microscopy

Analysis of 3D structures obtained during the self-assembly process were carried out through optical microscopy experiments using a 1 vol% concentration of CI particles dispersed in a 1:1 by volume water and glycerol solution.

In more detail, we used a Leica Z6 APO stereomicroscope tube attached to a Photron MiniUX camera. As mentioned in Section 5.3.1, we ensured proper dispersion of particles prior to each experimental test. The triaxial device was fitted with an EFFILUX EFFI-BHS LED illuminator to backlight the MR fluid and enhance the captured images having a bright white background contrasted with the black carbonyl iron particles. We loaded 330 μL of the MR fluid into the sample chamber located at the center of the coils in the triaxial device. The circular sample chamber is 20 mm in diameter and 1 mm in depth. A glass cover-slip (Fisher) is then gently placed covering the chamber to enclose the fluid and avoid air bubbles. The magnetic field configuration and image capturing of the experimental protocol is immediately initiated (unless otherwise indicated) to prevent sedimentation of the particles due to gravity resulting in a non-homogeneous system. Particle sedimentation would lead to a gradient in the dispersion of particles in suspension with a higher concentration of particles near the bottom of the sample. Upon introducing a static DC field to a sample with a particle gradient would theoretically result in the formation of chains with thicker bottoms.

5.3.3.2 Micro-CT

Imaging high concentrated structures is a challenge. Traditional bright-field microscopy fails to adequately distinguish structure formations of a 20 vol% concentration of CI particles due to the high density of particles impeding light penetration of the MR fluid. Micro-CT was used as an alternative imaging technique to better understand the high concentration structure formations that were later tested in the rheological experiments. The biggest obstacle in preparing our MR samples for Micro-CT was having to develop a method to solidify the sample while applying the external magnetic field. Prematurely

removing the magnetic field before the sample has thoroughly solidified would result in an inaccurate portrayal of the particle mesostructure.

First, we prepared the MR fluid of 20 vol% of CI particles dispersed in PDMS. We used a SYLGARD 184 Silicone Elastomer with a 10:1 mix ratio of the PDMS base and curing agent. A centrifugal mixer (Thinky US) was used for 10 minutes to disperse the CI particles and to remove the air bubbles. The MR fluid was immediately loaded to the sample chamber located in the center of the triaxial device; in this experiment the fluid was not enclosed. The three-step magnetic field configuration (see Section 5.3.2) was initiated and during the third stage re-application of the DC field to fix the structures we began the heating and curing process. The sample was heated with a Parkside PHLG 2000 C2 Heat Gun on its lower setting placed 26 cm above the sample. The sample was heated for 4.5 minutes, which was sufficient time to solidify the MR fluid, with the surface temperature of the sample reaching upwards of 110 ºC. The sample was then removed from the triaxial and placed on a pre-heated Torrey Pines Scientific HP30A-2 Hot Plate for an additional 15 minutes before carefully removing the sample from the sample chamber.

A 2 mm by 1 mm cylindrical fragment is cut from the sample and attached to a sample holder before loading it into the ZEISS Xradia 510 Versa 3D submicron imaging system. The sample is divided into a predetermined number of 2D slices that are successively scanned. The sample rotates around its axis of rotation on the holder first -180º and then 180º in the opposite direction completing a full 360º scan for each individual slice. The number of projections for each slice is fixed by the desired spatial resolution. Once finished the slices are stacked to reconstruct a 3D model of the sample, and corrections for attenuation and beam hardening are made. Dragonfly Pro visualization software was used to explore the 2D slices and 3D renderings of our sample mesostructures.

5.3.4 Rheometry

The mechanical response of the generated structures was ascertained in a magnetorheometer using a 20 vol% concentration of CI particles dispersed in a 1:1 by volume water and glycerol solution.

In more detail, rheological experiments were performed using a torsional homemade magnetorheometer adapting a MCR501 from Anton Paar to superimpose triaxial unsteady magnetic fields on the samples. A plate-plate configuration was used (20 mm diameter and 0.5 mm gap). We loaded 150 μL of MR fluid onto the sample platform for the rheometry tests and immediately lowered the upper plate and executed the experimental protocol, again to prevent particle sedimentation. All rheometry experiments were repeated three times.

In a typical rheometry experiment the protocol is as follows: i) First, a preshear is applied at a shear rate of 100 s^{-1} for 60 seconds, ii) then, the suspension is structured at rest 0 s^{-1} for 5 seconds, iii) next, the magnetic field configuration is applied to induce particle self-assembly (see Figure 5.1 and Section 5.4.2) at the same time a small-amplitude oscillatory shear (SAOS) flow is superimposed (strain amplitude $\gamma_0 = 0.01$ and frequency f =1 Hz), and iv) finally, a rheogram is performed by steadily increasing the shear rate from $\dot{\gamma} =$ 0.1 s^{-1} to 1000 s^{-1}. The small strain amplitude in stage iii was chosen to effectively measure the storage modulus response whilst ensuring the particle structures are not prematurely fractured during the structuration process.

5.4 Results and discussion

5.4.1 Videomicroscopy

Unsteady magnetic fields have been used to assemble several distinguishable CI microstructures suspended in a water and glycerol solution with the intended purpose of measuring the rheological response of these novel structures. Image capturing the particle structures throughout the magnetic field configuration protocol gives insight to how these structures assemble, rearrange, fracture and evolve over time depending on the chosen field configuration. A 1 vol% particle concentration showed both deterministic dipole-dipole aggregation and time-averaged aggregation dynamics could occur.

These two aggregation mechanisms, dipole-dipole and time-averaged aggregation, are fundamental to the outcome of the shape and form of the particle structure. Furthermore, the structure transition between uniaxial DC field and precession or perturbation AC field and vice versa is crucial to the

aggregate form. Figure 5.2 displays the final aggregate structures at the end of the three-step field protocol (see Figure 5.1) for the eight different magnetic field configurations defined in Table 5.1 as well as a baseline comparison structure, which was realized by simply applying a uniaxial DC field in the z-axis for the same duration as the three-step protocol. Exp. 1-6 utilized a precession AC field and Exp. 7-8 a perturbation AC field in the second stage of the field configuration. Exp. 1 & 7 both resulted in fortified columnar structures from a low angle medium frequency precession field and high angle low frequency perturbation field, respectively. Both Exp. 1 & 7 aggregation dynamics are defined by dipole-dipole magnetostatic interactions. In Exp. 1 the angle of precession is below the critical angle of precession $\theta_{f,crit}$ therefore the chain structure persists. Likewise the low frequency (and thus low Mn) of Exp. 7 similarly maintains the structural integrity of columnar chain structures. The difference compared to the baseline columnar structures is that both the respective precession and perturbation fields induce lateral chain coalescence that yield the fortified columnar structure, or essentially thick chain bundles. The motivation of lateral coalescence of neighboring chains is twofold: precession and perturbation motion can move two chains within close proximity from a repulsive in-registry to an attractive out-of-registry spatial positioning, and direct contact coalescence by chain collision is also viable.

Moving forward, Exp. 2-5 were done by introducing a high angle precession field above the critical angle of precession $\theta_{f,crit}$ and varying the field frequency. Exp. 2 is confidently within the low Mn range, and the high angle low frequency precession field results in the almost immediate coalescence and sedimentation of the aggregates, such that upon transitioning the field from precession to uniaxial DC field the aggregates fracture and reassemble into vertically-oriented segmented structures. The abrupt field transition from a uniaxial DC field to a precession AC field or another uniaxial DC field directed in a different direction and vice versa can often lead to aggregate fracturing and segmentation depending on the degree of angular change between field configurations.

Another instigator of drastic restructuration is the abrupt change between steady fields and high Mn precession fields and vice versa above the critical angle of precession. Exp. 3-5 are representative of this type of magnetic field transition and their resultant wavy sheet-like structures are shown in Figure 5.2. During the unsteady field configuration stage of the experimental protocol the CI suspension appears all black when imaged from above, indicating the

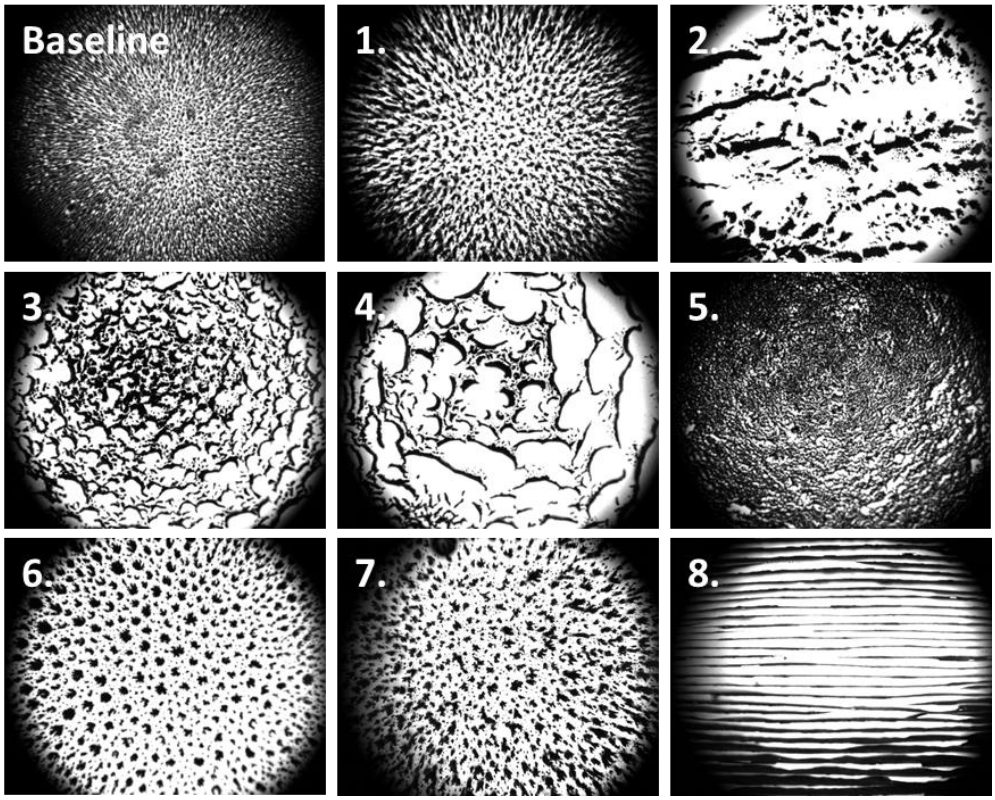

Figure 5.2 Captured images of the CI MR fluid following the first DC field interval in step 3 (Baseline), and the final structures for each of the eight experiments following the unsteady field interval and reapplying the DC field in the z-axis. All images were obtained at a 1 vol.% CI particle concentration in a 1:1 by volume water and glycerol solution. The images are a top view of the samples and the structures span approximately 1 mm in depth.

possible formation of horizontal layers. Layer formation occurs as a result of the time-averaged particle interaction dynamics, which emerges in high angle triaxial precession fields, biaxial rotational fields, and high angle perturbation fields under the condition of utilizing high field frequencies. At increasingly higher Mn precession fields above the critical angle of precession it is believed that the horizontal particle layer packing becomes more orderly, distinctly separated and defined, and dense. This explanation could, in turn, elucidate the aggregate density difference in the Exp. 3-5 structures. It is also possible that in Exp. 3-4 horizontal layers do not appear when the high angle precession field is applied but rather a crowded, opaque network of short-length precessing chains given the $Mn < 1$ for both tests and the final structure after the precession to uniaxial transition varies in wavy sheet density for this reason. That would leave the highly dense, more homogeneous final structure

of Exp. 5 – the most likely to yield horizontal layers due to the highest employed field frequency and a Mn > 1– a result of the spontaneous transition between horizontal layers to a very dense network of sheet-like structures when the steady DC field in the z-axis is reapplied. In order to validate these conjectures future experiments are necessary and are currently in progress. To overcome the top view imaging limitations in Exp. 3-5 (structures in high angle precession fields viewed in line with the DC field component often appear black in a bright-field microscopy setup), we propose rotating the precession axis 90° from the z-axis to, say, the x-axis and therefore we will be able to visualize the structures from a lateral perspective rather than an aerial view. In this field configuration setup the uniaxial DC field is applied in the x-axis and a biaxial rotational field is superimposed in the y, x-plane to generate the precession field.

Exp. 8 shows another method for producing layered structures, in this case well-defined vertical layers, through time-averaged aggregation dynamics. The high angle high frequency perturbation magnetic field configuration thwarts the assembly of chain-like structures and the time-averaged magnetostatic interactions ultimately drive the particles to migrate into vertical layers. The formation of vertical layers was not observed in the work of Donado *et al.* [20] as their experiments only concerned low angle oscillatory perturbation fields, and similar to the low angle precession fields c hains generally follow the field vector for low Mn or collapse to the axis in which the uniaxial DC field is induced for high Mn.

Lastly, Exp. 6 resulted in conical structures having derived from its slightly modified experimental protocol – the CI colloidal suspension was allowed to sediment for 15 minutes prior to initiating the three-step field configuration protocol that includes a low angle precession field similar to Exp. 1. The conical structures begin to take shape after the first uniaxial DC field step, with some structures left open on one side. The subsequent low angle precession field encourages some of the open structures to connect and enclose forming the conical shape. The base of the conical structures is flush with the bottom of the sample chamber and the point is situated above. A top view static image of the conical structures does not do them justice, and are best visualized in precession motion. However, they are made up of tilted individual chains (some may be laterally coalesced), and have a hollow interior. The structure is reminiscent of a teepee, a tent that was used by some indigenous peoples of North America.

5.4.2 Micro-CT

Micro-computed tomography, or Micro-CT, is a useful imaging technique for reconstructing a 3D image from 2D cross-section projections of a specific object. Applying this technology for imaging a "solidified" MR fluid, x-rays passing through the sample discern the particle structure on a micron scale regardless of the particle concentration – the main advantage over optical microscopy, which falls short working with highly dense opaque sample fluids. As mentioned in Section 5.3.3.2, the CI particles were dispersed in a PDMS medium and allowed to aggregate and take form under an external magnetic field before the sample was solidified. For our experiments the spatial resolution was between 1.69-1.93 μm depending on the density of the sample, which is below the average particle size for CI particles EW grade, thus assuring a clear representation of the particle structures.

Prior to carrying out the Micro-CT experiments for two selected field configurations, Exp. 1 and Exp. 8, on a high concentration MR fluid we tested these configurations on a low 1 vol% CI particle suspension in PDMS. The reason for this was threefold: to render a full three-dimensional image of our low concentration particle structures that previously we only had an aerial view of from the videomicroscopy experiments, to see if the structures would form in the more viscous PDMS, and lastly to make sure the structures remained unyielding during the solidification process. The 1:1 by volume water and glycerol fluid base has a viscosity around 8.4 mPa·s whereas the PDMS fluid base has a viscosity of 3500 mPa·s. Despite a much higher viscosity, we were able to replicate the fortified columnar structures and vertical layer structures, Figure 5.3a and 5.3b, respectively, using their corresponding field configurations. Figure 5.3a and 5.3b show a 2D trans-axial projection of the columnar structures and vertical layers, represented by dots and lines, respectively. Therefore, it was determined that the base fluid impact is minimal with the magnetic field strengths we used in our experiments. Additionally, the 3D model reconstruction showed no indication that the hot air gun impacted the particle structures at the sample surface nor throughout the sample.

Moving on to the high concentration scenario, the columnar and vertical layer mesostructures shown in Figure 5.3c and 5.3d were formed under the same field configurations as the analogous structures appearing in Figure 5.3a and 5.3b but clearly with a higher particle density. As expected for high concentration MR fluids, there do not appear isolated structures, but rather a

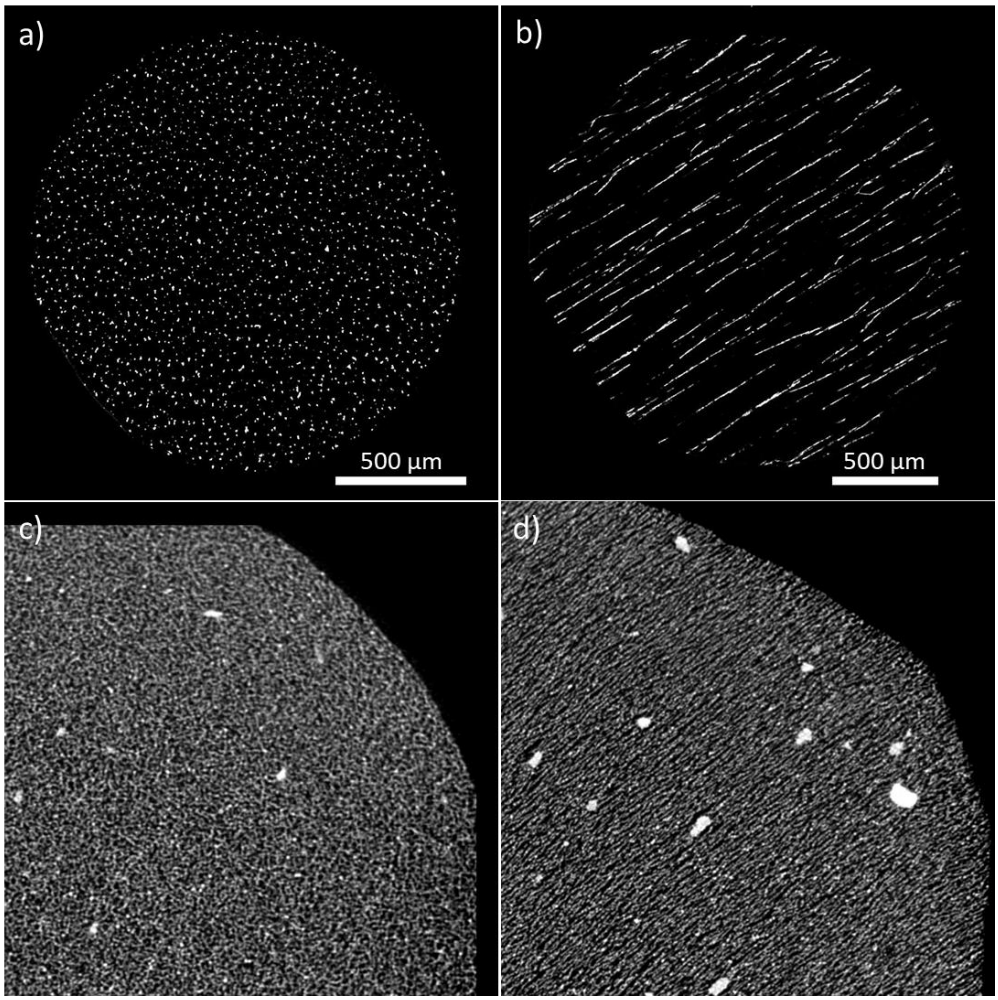

Figure 5.3 2D slices from the micro-CT models of (a) columnar structures in a 1 vol.% CI particles dispersed in PDSM solution, (b) vertical layer structures in a 1 vol.% CI particles dispersed in PDMS solution, (c) columnar structures in a 20 vol.% CI particles dispersed in PDMS solution, and (d) vertical layer structures in a 20 vol.% CI particles dispersed in PDMS solution.

more complex network of laterally connected structures. However, there does appear a convoluted lineation shown in Figure 5.3d at a 45º angle suggesting the presence of very dense layered structures. The orientation of the layers are guided in parallel to the direction of the superimposed perturbation field used to structure them. Figure 5.3c does not show signs of this lineation. The intricate differences between the two high concentration labyrinthine mesostructures affirm our position that each magnetic field configuration

yields unique structures even in MR fluids with a large particle load, which are more often used for industrial applications.

5.4.3 Rheometry

The reason for our study was to prove that exotic CI particle structures formed under unsteady magnetic fields can enhance the rheological response of the MR fluid compared to ordinary uniaxial DC fields. Integrating the rheometer with the triaxial magnetic field generator to study the rheology of MR fluids in real time has been vital in performing this task. Small-amplitude oscillatory shear tests (SAOS) were done during the three-step structuration process (see Figure 5.1) to analyze the storage modulus response to the various structure formations discussed in the previous section. Figure 5.4 displays a selection of G' curves (Exp. 1 fortified columnar structures, Exp. 3 dense sheets, and Exp. 8 vertical layers), with three clear curve plateaus reflecting the initial uniaxial DC field, unsteady field, and return to uniaxial DC field configurations in sequence. As each of the eight tested field configurations only differ in the unsteady field interval (the middle of the three field steps) one can easily identify a G' increase by comparing the first (denoted as the baseline case) and

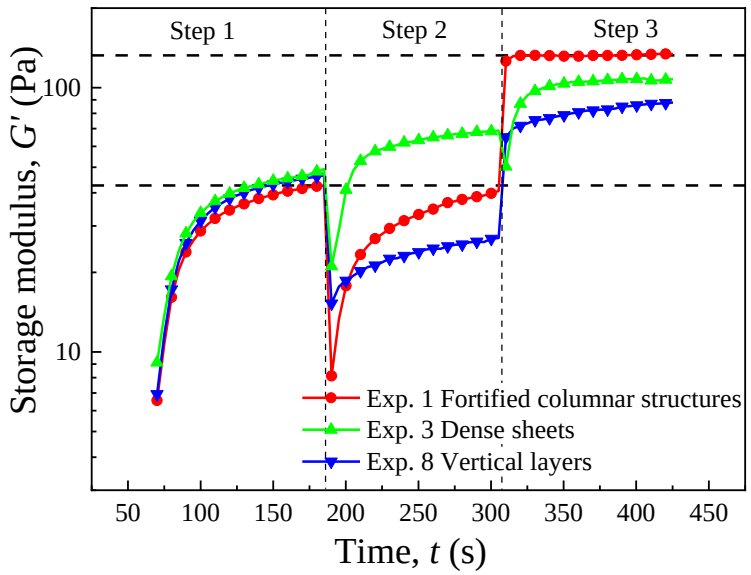

Figure 5.4 Small amplitude oscillatory shear (SAOS) tests showing an overall increase in the storage modulus G' response between the last and first interval in step 3 of the experimental protocol (see Figure 5.1) for a selection of field configurations/structures tested.

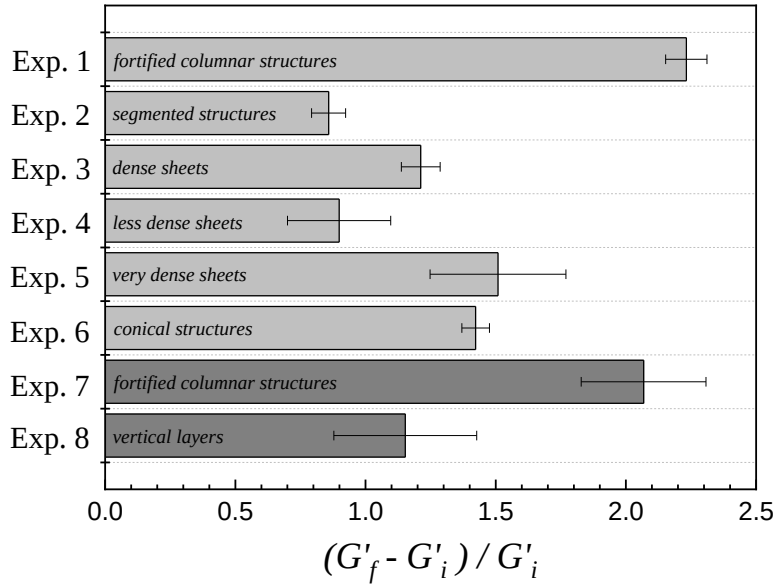

Figure 5.5 Summary of the storage modulus G' response between the last (G'_f) and first (G'_i) interval of the field configuration step of the protocol (see Figure 1). Exp. 1-6 (light gray) were done with a precession field and Exp. 7-8 (dark gray) were done with a perturbation field. The results show that all eight field configurations produced a robust structure that enhanced the MR response compared to the uniaxial DC field case. In particular, the fortified columnar structures formed from the Exp. 1 (low angle precession) and Exp. 7 (high angle perturbation) yielded the highest increase in G'.

last curve plateaux. As expected the nearly overlapping curves of the initial first plateau (uniaxial DC field) at G'_i = 45 Pa indicates that the composition of the MR fluid sample and the field strength produced by the triaxial device was consistent between testing trials. The final plateau curves for the fortified columnar structures, dense sheets, and vertical layers are measured at G'_f = 134 Pa, 107 Pa, and 87 Pa, respectively. Each unique structure, more robust in nature than the basic structure produced by typical uniaxial DC fields, has an increase in its storage modulus compared to the baseline case.

In fact, all eight tested field configurations yielded a bolstered G' response as summarized in the Figure 5.5 plot. The fortified columnar structures derived from Exp. 1 low angle precession field and Exp. 7 high angle perturbation field gave rise to the best response, both approximately tripling the G' response compared to the baseline case, with the precession slightly inching above the perturbation.

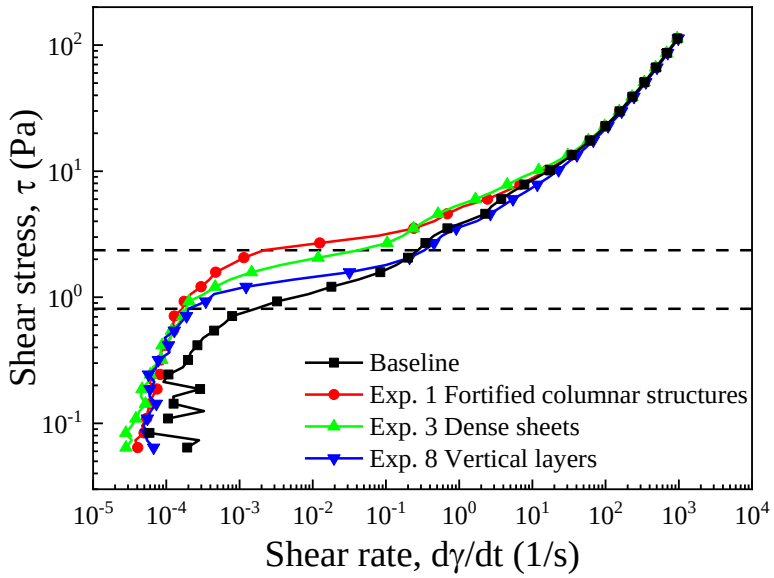

Figure 5.6 Shear stress with increasing shear rate shows an increase in the yield stress in comparison to the baseline case for a selection of field configurations/structures tested. The dashed black lines show the relative increase in MR response for the fortified columnar structure compared to the baseline case.

Following the structuration period, a rheogram was performed and the shear stress versus shear rate curves shown in Figure 5.6 for a selection of structures (again, Exp. 1 fortified columnar structures, Exp. 3 dense sheets, and Exp. 8 vertical layers). The yield stress is taken to be the onset of the curve plateau. Upon quick inspection of the plot it is clear that the yield stress of each Exp. is an improvement to the baseline case. The greatest improvement came from the Exp. 1 fortified columnar structures with a yield stress of 2.4 Pa, which is three times larger than the baseline yield stress of 0.8 Pa. As expected, overall, there is a similar quantitative trend in both the storage modulus and yield stress response for the selected structures shown in Figure 5.4 and 5.6. Since the vertical layers structure is not rotationally symmetric in a plate-plate rheometry setup, it would be interesting to perform a unidirectional shear rheogram both parallel and perpendicular to the layers and compare the rheological response.

In the presence of uniaxial DC fields particle aggregation is limited to chains, chain bundles, and non-reinforced dense laterally-connected structures depending on the concentration of the MR fluid. The results of our videomicroscopy tests showed a wide range of the possible particle structures

capable of forming under unsteady fields, some more homogeneous and others more disordered. The rheometry tests only begin to address the characteristic differences of each of the eight structure networks presented in this work. The complexity of each mesostructure architectural design is the *literal* framework for understanding how these strengthened structures are more robust to yielding.

5.5 Conclusions

We have demonstrated that triaxial precession fields and oscillatory planar perturbation fields can structurally transform a MR fluid such that it improves the rheological response beyond the limits set by traditional uniaxial DC fields. Notably, the triaxial precession fields employed in this work were performed at the same field strength as the baseline uniaxial DC field, thus ensuring that any MR enhancement that arose under these fields is due to the field configuration rather than a change in the field strength. Of the many structures discussed here, fortified columnar structures assembled under low angle precession fields had the best response. Triaxial fields in some cases are capable of promoting lateral chain coalescence that leads to thicker, stronger structures. Vertical layers and sheet structures formed due to time-averaged aggregation dynamics in triaxial and biaxial fields have also been shown to increase the yield stress of a fluid, but to a lesser extent than fortified columnar structures.

These MR enhancements were observed using only modest external magnetic fields strengths that we were able to generate in the laboratory with the triaxial device. Qualitatively similar MR fluid responses are expected for higher intensity field strengths. Apart from rheological applications, the structures discussed in this work could be of potential use as a scaffold for cell deposition and guided directional cell growth. More work is needed to further explore how unsteady fields and field transitions can affect particle structure evolution and MR responses.

Acknowledgements

This work was supported by MINECO MAT 2016-78778-R project (Spain), MICINN PID2019-104883GB-I00 project (Spain), Junta de Andalucía P18-FR-2465 project and European Regional Development Fund (ERDF). M. Terkel acknowledges BES-2017-079891 fellowship.

References

[1] de Vicente J, Klingenberg D J and Hidalgo-Álvarez R 2011 Magnetorheological fluids: a review *Soft Matter* **7(8)** 3701-3710.

[2] Martin J E and Snezhko A 2013 Driving self-assembly and emergent dynamics in colloidal suspensions by time-dependent magnetic fields *Reports on Progress in Physics* **76(12)** 126601.

[3] Wereley N M 2013 *Magnetorheology: Advances and Applications* (London: RSC Publishing)

[4] Choi S B and Li W 2019 *Magnetorheological materials and their applications* (IET)

[5] Zhu X, Jing X and Cheng L 2012 Magnetorheological fluid dampers: a review on structure design and analysis *J. Intell. Mater. Syst. Struct.* **23(8)** 839-873.

[6] Furst E M and Gast A P 2000 Dynamics and lateral interactions of dipolar chains *Physical Review E* **62(5)** 6916.

[7] Halsey T C and Toor W 1990 Fluctuation-induced couplings between defect lines or particle chains *Journal of Statistical Physics* **61(5-6)** 1257-1281.

[8] Martin J E, Odinek J, Halsey T C and Kamien R 1998 Structure and dynamics of electrorheological fluids *Physical Review E* **57(1)** 756.

[9] Fermigier M and Gast A P 1992 Structure evolution in a paramagnetic latex suspension *Journal of Colloid and Interface Science* **154(2)** 522-539.

[10] Promislow J H and Gast A P 1996 Magnetorheological fluid structure in a pulsed magnetic field *Langmuir* **12(17)** 4095-4102.

[11] Promislow J H and Gast A P 1997 Low-energy suspension structure of a magnetorheological fluid *Physical Review E* **56(1)** 642.

[12] Swan J W, Bauer J L, Liu Y and Furst E M 2014 Directed colloidal self-assembly in toggled magnetic fields *Soft Matter* **10(8)** 1102-1109.

[13] Bauer J L, Li Y, Kurian M J, Swan J W and Furst E M 2015 Coarsening mechanics of a colloidal suspension in toggled fields *The Journal of Chemical Physics* **143(7)** 074901.

[14] Kim H, Bauer J L, Vasquez P A and Furst E M 2019 Structural coarsening of magnetic ellipsoid particle suspensions driven in toggled fields *Journal of Physics D: Applied Physics* **52(18)**, 184002.

[15] Martin J E, Anderson R A and Tigges C P 1998 Simulation of the athermal coarsening of composites structured by a biaxial field *The Journal of chemical physics* **108(18)**, 7887-7900.

[16] Martin J E, Venturini E, Gulley G L and Williamson J 2004 Using triaxial magnetic fields to create high susceptibility particle composites *Physical Review E* **69(2)**, 021508.

[17] Martin J E 2005 Using triaxial magnetic fields to create optimal particle composites *Composites Part A: Applied Science and Manufacturing* **36(4)**, 545-548.

[18] Martin J E 2009 Theory of strong intrinsic mixing of particle suspensions in vortex magnetic fields *Physical Review E* **79(1)**, 011503.

[19] Martin J E, Shea-Rohwer L and Solis K J 2009 Strong intrinsic mixing in vortex magnetic fields *Physical Review E* **80(1)**, 016312.

[20] Donado F, Sandoval U and Carrillo J L 2009 Kinetics of aggregation in non-Brownian magnetic particle dispersions in the presence of perturbations *Physical Review E* **79(1)**, 011406.

[21] Shahrivar K, Carreón-González E, Morillas J R and de Vicente J 2017 Aggregation kinetics of carbonyl iron based magnetic suspensions in 2D *Soft matter* **13(14)**, 2677-2685.

[22] Melle S, Calderón O G, Fuller G G and Rubio M A 2002 Polarizable particle aggregation under rotating magnetic fields using scattering dichroism *Journal of Colloid and Interface Science* **247(1)**, 200-209.

Chapter 6

Enhancing magnetorheology with precession magnetic fields

Matthew Terkel[1], Javier Tajuelo[2] and Juan de Vicente[1]

[1]F2N2Lab, Magnetic Soft Matter Group and Excellence Research Unit "Modeling Nature" (MNat), Department of Applied Physics, Faculty of Sciences, University of Granada, C/Fuentenueva s/n, 18071 Granada, Spain

[2]Present address: Departamento de Física Interdisciplinar, Facultad de Ciencias, Universidad Nacional de Educación a Distancia, UNED, 28040 Madrid, Spain

Published in

JOURNAL OF RHEOLOGY®

J. Rheol. **2022**, 66, 67-78

Abstract

We demonstrate a new route to enhance magnetorheology using precession-like magnetic fields. This field configuration is generated by the superposition of a 2D rotational field applied orthogonal to a uniaxial DC field. Maintaining a columnar linear chain structure when applying a precession field was determined to be integral in increasing the average cluster size of the aggregates for low precession angles and a low Mason Number. A yield stress increase was experimentally observed when reapplying a uniaxial DC field following the application of a controlled low angle precession field indicating a favorable structural evolution had taken place under the unsteady field configuration. Experimental results of small-amplitude oscillatory shear tests and shear rheograms are supported by particle level simulation 3D models and start-up tests.

6.1 Introduction

Conventional magnetorheological (MR) fluids are suspensions of magnetizable carbonyl iron (CI) particles in a liquid carrier. In the absence of a magnetic field the suspension behaves as a nearly Newtonian material. However, in the presence of magnetic fields, the CI particles become magnetized and interact forming elongated structures in the field direction [1]. As a result, the flow behavior of the MR fluid is significantly affected up to the point that a liquid-to-solid transition can also appear for sufficiently large field strengths and particle concentrations [2,3].

The literature shows different pathways to enhance magnetorheology. Probably the most exhaustively investigated approaches concern modifications in the formulation of the MR fluids. Ulicny *et al.* (2010) partially substituted the dispersed CI particles with non-magnetic particles and found that the yield stress can be enhanced [4]. They tested both 30 vol% monomodal (2 μm diameter) and 30 vol% bimodal (2 and 8 μm diameter, 1:1 mixture by mass) CI MR fluids with the addition of 15 vol% hollow glass beads. While both systems exhibited a yield stress enhancement compared to the CI only experiment, the bimodal particle system resulted in the largest increase of the yield stress. The addition of non-magnetic particles to MR fluids reduces the fluid density and potential cost, which is advantageous for commercialized applications. In view of the fact that bidisperse MR fluids and non-spherical

particles can exhibit improved MR characteristics [5,6], Bombard *et al.* (2014) coupled this idea of introducing non-magnetic particles with particle morphology and confirmed that particle shape anisotropy is also a key factor in understanding how non-magnetic additives can increase the yield stress of a dimorphic MR fluid [7]. In their experiments they added magnetic chromium dioxide nanofibers and non-magnetic goethite nanofibers to a microsphere-based MR fluid. Both nanofibers enhanced the yield stress. In the magnetic nanofiber case the nanofiber particles, adsorbing near the connecting joints of two spherical particles in a chain through magnetostatic interactions, lead to a local rising in the magnetic permeability. Non-magnetic nanofibers on the other hand can increase the interparticle friction of spherical particle structures and produce similar yield stress enhancements. A more complete study of bimodal MR fluids was done by Morillas *et al.* (2018) using a number of different nanoparticles such as barium ferrite, magnetite, and iron [8]. SEM images of the particle system showed these nanoparticles surrounding the micron-sized CI particles in a cloud-like formation, which is the effect of strong magnetostatic interaction between the large and small particles. In fact, Morillas *et al.* (2018) showed that the iron-based nanoparticles in particular, which have greater magnetic properties than CI particles at the magnetic field investigated, clearly produce an effective yield stress enhancement compared to a monomodal fluid (upwards of 150 % improvement for a constant total volume fraction of solids of 45 vol%), by cause of sufficiently large coercive fields inducing particle interaction [8].

Apart from tuning the chemical composition of the MR fluid, other attempts involve more sophisticated approaches by controlling the flow kinematics and field configuration. Some examples are the so-called squeeze-strengthening effect [9-11] and the superposition of 2D alternating magnetic fields [12]. The process of compression-assisted aggregation behind the so-called squeeze-strengthening effect involves first imposing a uniaxial DC field to an MR fluid and allowing the particles to form chain aggregates in line with the field. Then, the MR fluid is compressed along the field direction. Tao *et al.* (2000) were able to enhance the static yield stress from 80 kPa to 800 kPa through compressing the fluid following the field application of a 372 $kA \cdot m^{-1}$ external field [9]. We know that, when unprovoked, a low concentration of particle chains will remain isolated or thinly bundled together in the presence of a uniaxial field. Tao measured after compression the cross section of their chain bundles 50 µm in diameter and consisting of at least 100 laterally coalesced chains. The compression and thickening of these anisotropic chain structures

is imperative to the enhancement of the static yield stress. Zero enhancements were found when the MR fluid was compressed prior to the application of the uniaxial DC field, because the randomly dispersed spherical particles are free to move in the carrier fluid and never aggregate into thick chain structures.

de Vicente *et al.* (2011) carried out squeeze flow magnetorheometry experiments by slowly moving down the upper plate geometry of a rheometer towards a stationary bottom plate while monitoring the normal force response of the MR fluid sample [13]. An external magnetic field was induced on the MR fluid during this compression process. Gap spanning structures continuously fracture and reform as the fluid is compressed thus increasing the normal force when the upper plate velocity is slow enough to allow particle restructuration. Combining small-amplitude oscillatory shear as the top plate lowers on the sample, they observed an increase in the storage modulus G' response for compressive strains up to 0.5 indicating a compression-induced shear strengthening effect as well. Particle-level simulations supported the experimental results.

Donado *et al.* (2009) found that introducing a low-angle oscillatory perturbation magnetic field following an interval of uniaxial DC field resulted in the increase of the MR fluids viscosity [12]. Moreover, upon reinstating the DC field after the perturbation field interval the viscosity further increased. The perturbation field was generated by applying an oscillatory field in a single axis orthogonal to a uniaxial DC field. The oscillatory movement is believed to provoke an additional mechanism in the aggregation dynamics. For the higher particle concentration ($\phi = 0.03$) tested there is a noticeable increase in the viscosity, whereas the low particle concentration ($\phi = 0.005$) has a negligible response in comparison. Thus, the particle concentration is an important factor when testing MR enhancement beyond uniaxial DC fields. Alternative mechanisms for aggregation dynamics are only observed when the colloidal suspension is occupied by particle structures within interacting distance of one another in the presence of field perturbation [14]. This is also expected to be true for more complex unsteady field configurations.

Inspired in the paper by Donado *et al.* (2009) this manuscript describes a novel route for the MR enhancement using unsteady precession (3D) magnetic fields to generate stronger field-induced structures and therefore a larger yield stress. In more detail, the method consists in first inducing the aggregation of vertically oriented structures using a uniaxial DC field, followed by an interval

of unsteady precession magnetic fields, then followed by another interval of uniaxial DC field. The simulations reported here along with the experiments on the rheological response and aggregation dynamics of the MR fluid after an interval of unsteady precession magnetic fields suggests that lateral chain coalescence resulting in thicker structures is the key aggregation mechanism taking place under the precession fields tested in this work.

6.2 Particle-level simulations

The simulations comprise $N = 1000$ randomly distributed monodispersed hard sphere particles, with unit diameter $D = 2a = 1$, in a 3D simulation box with side length L and volume $V = L^3$. We control the particle concentration of the system by adjusting L while maintaining constant N and the particle unit diameter D. The simulated box size used in the particle-level simulations was $L = 13.78$, which gives a 20 vol% concentration of particles. This is the same concentration used in the rheometry experiments (see Section 6.3.3). The top and bottom boundaries of the box are hard boundaries, whereas the vertical side boundaries have periodic boundary conditions. In non-shearing intervals of the simulation the top and bottom boundaries are stationary. The box therefore limits the maximum length of a vertically oriented linear aggregate to around 13 particles. In the case of shearing intervals such as a simulated start-up test, a uniaxial shearing direction is implemented by displacing the top boundary and assuming a linear velocity profile in the fluid. The simulations were carried out using Fortran as this programming language was deemed best for reducing computation times.

We follow the classical simulation approach by Klingenberg *et al.* (1990) neglecting inertia and Brownian motion [15]. This approach has been successfully employed in the past to explain the structure and dynamics of MR fluids [16-18].

In this manuscript we are interested in unsteady magnetic fields $\vec{H}$ constituted by the superposition of a uniaxial DC field in the z direction and a constant magnitude rotating field in the x,y-plane:

$$\vec{H} = H\{\sin\theta_f[\sin(2\pi ft)\hat{x} + \cos(2\pi ft)\hat{y}] + \cos\theta_f\hat{z}\} \qquad (6.1)$$

Here, θ_f is the precession angle (formed by the field $\vec{H}$ and the vertical direction $\hat{z}$) and f is the frequency of the rotating AC field in the x,y-plane. With this, magnetostatic forces are modeled under the Mean Magnetization Approximation in the linear magnetization regime [19].

Monodisperse spherical particles (with radius a) are treated as point dipoles having a magnetic moment:

$$m = \frac{4}{3}\pi a^3 M \tag{6.2}$$

where the particle magnetization $M = \chi H$. The magnetic susceptibility is defined as $\chi = 3\beta = 3(\mu_{\mathrm{pr}} - \mu_{\mathrm{cr}})/(\mu_{\mathrm{pr}} + 2\mu_{\mathrm{cr}})$, where μ_{pr} is the relative permeability of the particles and μ_{cr} is the relative permeability of the continuous phase.

The magnetostatic interaction force between two particles when the magnetic dipole moments are equal and aligned along the z-axis can be written as:

$$\vec{F}_i^m = \frac{3\mu_0\mu_{\mathrm{cr}}m^2}{4\pi r^4}\left[(3\cos^2\theta - 1)\hat{r} + \sin(2\theta)\hat{\theta}\right] \tag{6.3}$$

where r is the distance separating the two particles, θ is the angle formed between the direction of the external magnetic field and the center-to-center line between the particles, and $\mu_0 = 4\pi \times 10^{-7}$ Tm/A is permeability of vacuum. Stokes' drag force was used to define the hydrodynamic forces acting on a particle in suspension:

$$\vec{F}_i^h = 6\pi\eta a\left(\vec{v}_i - \frac{d\vec{r}_i}{dt}\right) \tag{6.4}$$

where η is the viscosity of the carrier fluid, $\vec{r}_i$ is the position of the particle and $\vec{v}_i$ is the fluid velocity, which is either zero in the absence of shear $\vec{v}_i = 0$, or only has an x-component in the presence of shear and depends only in the z-coordinate of the particle $\vec{v}_i = v_x(z_i)\hat{\imath}$.

Lastly, repulsive forces between individual particles and repulsive forces between particles and the hard boundary walls are assumed to be exponential with a decay ratio $\kappa = 100/D$ as used by Fernández-Toledano *et al.* (2015) [20]. It has been previously reported that these particular repulsive forces

successfully mimic the lateral coalescence of neighboring chains (see Klingenberg *et al.* (1990) [15]) in contrast to polynomial expressions or shorter ranged forces (e.g. $\kappa = 10/D$ in Melle *et al.* (2002) [21]).

The particle diameter, $2a$, and a time scale, $12^2\eta/(\mu_0 M^2)$, were used to non-dimensionalize the governing equations defining the particle evolution. Once the positioning of all the particles in the simulation box is determined, the total shear stress can be determined as follows:

$$\tau_{xz} = -\frac{1}{V}\sum_i z_i F_{xi}^{total} \tag{6.5}$$

where F_{xi}^{total} is the combined magnetostatic and repulsive forces acting on particle i along the x-axis shearing direction and z_i is the position coordinate of particle i along the z-axis. To dimensionalize this shear stress one only needs to multiply by $\pi\mu_0 M^2/48$.

When discussing rotating chain-like structures under the presence of an external magnetic field, we have the Mason Number to define the system:

$$\mathrm{Mn} = \frac{12^2\eta\omega}{\mu_0 M^2} \tag{6.6}$$

Here ω is the rotational field frequency. Mn is a non-dimensionalized number that compares the magnetostatic interaction forces holding a rotating aggregate structure together to the hydrodynamic forces acting counteractively to fracture the aggregate. For $\mathrm{Mn} < 1$ chains are expected to follow in line with the external field vector, whereas for $\mathrm{Mn} > 1$ linear chains will evolve into an S-shape, fracture, and ultimately degenerate into circular disk-like shapes for the largest $\mathrm{Mn} \gg 1$. We are interested in working with magnetic field configurations in the low Mn regime to ensure the particle structures do not prematurely fracture and hinder the desired lateral coalescence aggregation dynamics.

Table 6.1 defines the geometric parameters of the particle-level simulations discussed in the context of this work, including the number of isolated particles N_i, the number of clusters N_c, the average cluster size S, linearity Ln, zenithal angle Zn and connectivity $C(\theta)$. Results represented in this work were

Table 6.1 Geometric parameters used in particle-level simulations.

Geometry parameter	Symbol	Definition
Number of isolated particles	N_i	The number of isolated particles that are not part of a larger aggregate structure. Isolated particles are not counted as clusters in our results.
Number of clusters	N_c	The number of clusters with a minimum of at least two particles.
Average cluster size	S	$S = \frac{N-N_i}{N_c}$
Linearity	Ln	$Ln = \frac{(I_j^{\max})^{1/2} - (I_j^{\min})^{1/2}}{(I_j^{\max})^{1/2} + (I_j^{\min})^{1/2}}$ This linearity details the anisotropic morphology of particle clusters using the eigenvalues of the chain's inertia tensor. If the cluster is perfectly linear, the linearity is 1, whereas if the cluster has the shape of a perfect sphere, the linearity is 0.
Zenithal angle	Zn	The angle of the average cluster direction with respect to the vertical z axis.
Connectivity	$C(\theta)$	The mean number of particles in contact to a central one with an orientation between angles $\theta - d\theta$ and θ with respect to the z axis, where $d\theta = 10°$: $C(\theta) = N(\theta)/(N-1)$. Here, $N(\theta)$ is the number of connected particles oriented between angle $\theta - d\theta$ and θ, and N is the total number of particles in the system.

averaged from five simulation trials each starting from the same five random $N = 1000$ particle configurations.

6.3 Experimental

6.3.1 Materials

MR fluids investigated in this work were prepared by dispersing carbonyl iron (CI) particles (EW grade from BASF SE Germany) in a 1:1 water/glycerol (99% Fisher chemical) mixture with a viscosity of around 8.4 mPa·s. A centrifugal mixer (Thinky US) was used for 5 minutes followed by sonication for an additional 2 minutes to guarantee dispersion of particles.

6.3.2 Optical microscopy and triaxial magnetic field generator

Analysis of 3D structures in precession motion were carried out through optical microscopy experiments using a dilute ($\phi = 0.01$) dispersion of CI particles dispersed in a 1:1 by volume water/glycerol mixture.

We used a Leica Z6 APO stereomicroscope attached to a high speed (Photron MiniUX) camera. A homemade triaxial magnetic field generator was fitted below the microscope with an EFFILUX EFFI-BHS LED backlight illuminator (see Figure 6.1a) to best image capture the black CI particles. The generator consists of five coils in total, four having their axes situated in the x,y-plane and a fifth larger coil located beneath pointing upwards, which induces the uniaxial DC field in the z-axis. All coils were fitted with a mu-metal core to increase the external field strength induced at the center of the sample platform. Three current signals are provided to each of the three axis coils. A capacitor bank also is connected in series with the triaxial device to reach high frequencies upwards of 4 kHz, although the low experimental field frequencies applied in this work remained well below the minimum frequency threshold required to access the capacitor bank. The current flowing through each of the three independent circuits is continuously read and used in a custom-built feedback control loop to ensure that, first, the phase lag between the x- and y-components of H is always in quadrature phase, and, second, the magnitude of H fits the target one. Therefore, the possibility of changes in room temperature or coil heating causing a current drop is eliminated and the experimental conditions are kept consistent in all the experiments.

Using a teslameter (F.W. Bell 5170) the three axis coils were calibrated by measuring the field strength at the center of the triaxial sample holder while varying the DC current, I. A transverse probe attachment to the teslameter was used for measurements in the x,y-plane and an axial probe for the z-axis. An expected linear relationship was found between the field strength dependence on the intensity current as expressed through the following equations: $H_{x,y}(\mathrm{kA{\cdot}m^{-1}}) = 7.77\, I_{x,y}(\mathrm{A})$ for the x,y-axis and $H_z(\mathrm{kA{\cdot}m^{-1}}) = 2.80\, I_z(\mathrm{A})$ for the z-axis. The ratio factor is noticeably lower for the z-axis calibration due to the larger working distance between the coil and the center of the sample holder as compared to the coil positions in the x,y-plane. A DC current in the z-axis of $I_z = 2$ A (or $H_z = 5.6\ \mathrm{kA{\cdot}m^{-1}}$) was set as a limiting factor in designing all subsequent precession field configurations for the experimental work. This current was determined to be high enough to accurately measure a rheological

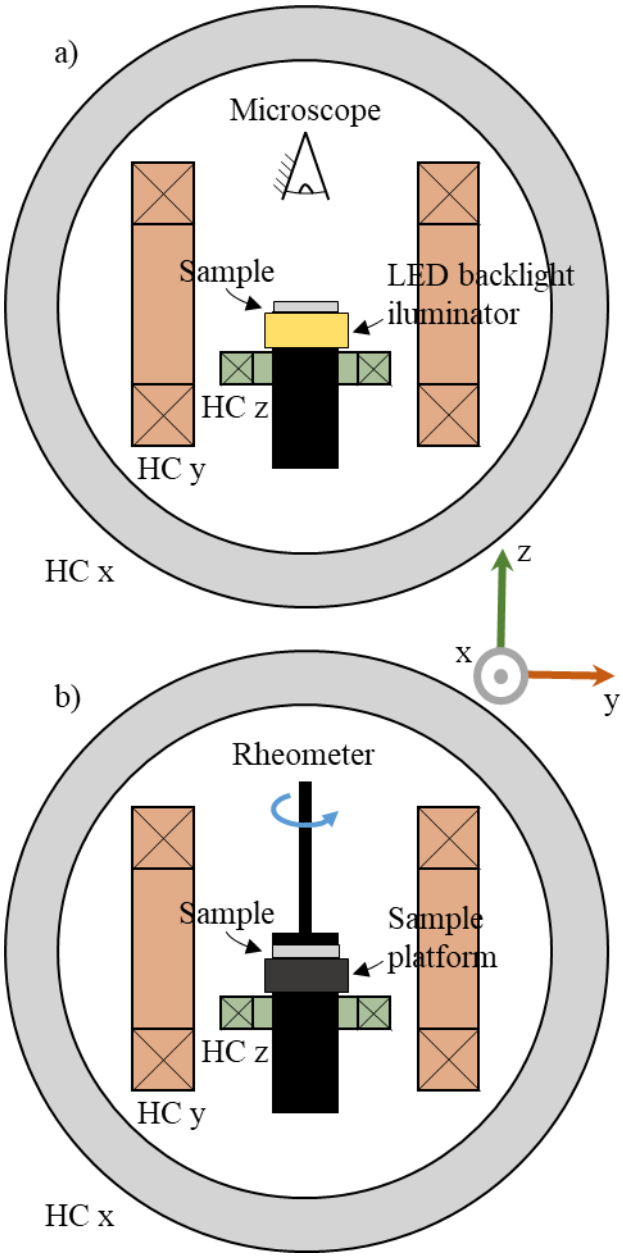

Figure 6.1 Schematics of the triaxial magnetic field generator. a) Adaptation to the stereomicroscope. b) Adaptation to the rheometer. The triaxial magnetic field generator consists of 4 coils of equal size situated in the x, y-plane and a fifth, larger coil situated beneath the MR fluid sample, which generates the field in the z-axis. The coils are depicted as different sizes for image clarity. The current (I) to field strength (H) conversion for each axis was calibrated at the center of the sample platform.

response without overworking the triaxial generator. To generate a precession field as a function of precession angle we use currents $I_{x,y}(\mathrm{A}) = 5.6 \sin\theta_f \,/7.77$ (in quadrature phase) and $I_z(\mathrm{A}) = 5.6 \cos\theta_f \,/2.80$ (in DC). For example, a precession field configuration with a precession angle $\theta_f = 15^{\circ}$ would require current components of $I_{x,y} = 0.19$ A and $I_z = 1.93$ A. A simple calculation would show that plugging these current values into $H_{x,y}$ and H_z and calculating the superposition field strength results in the desired 5.6 $\mathrm{kA \cdot m^{-1}}$.

In a typical experiment, we loaded 330 µL of the MR fluid into the sample chamber (a cylindrical recipient 20 mm in diameter and 1 mm in depth) situated at the center of the coils in the triaxial device. A glass cover-slip was then gently placed covering the chamber to enclose the fluid and avoid air bubbles. To avoid particle sedimentation and an uneven distribution of the suspended particles, the experimental protocol consisting of the application of the magnetic field configuration and the subsequent image capturing is immediately initiated.

6.3.3 Rheometry

Rheological experiments were carried out on concentrated CI particle suspensions ($\phi = 0.20$) in a 1:1 by volume mixture of water and glycerol. These higher concentrated MR fluids are typically used in industrial applications.

Experiments were performed using a modified MCR501 rheometer from Anton Paar. The homemade triaxial magnetic field generator was mounted on top of the rheometer (see schematics in Figure 6.1b). A sample platform is placed in the center of the coils (in lieu of the illumination setup) and a 20 mm diameter plate-plate geometry was used with a 0.5 mm gap. We loaded 150 μL of the CI MR fluid sample to the sample platform and immediately initiated the rheometry test, again to minimize particle sedimentation.

The protocol of the rheometry experiment was optimized as follows (see schematics in Figure 6.2a): I) First, after loading the MR fluid a shear rate of 100 $\mathrm{s^{-1}}$ for 60 seconds was applied to further ensure proper dispersion of the CI particles, II) then, the suspension is structured at rest 0 $\mathrm{s^{-1}}$ for 5 seconds to stabilize the system, III) next, the magnetic field configuration is applied to

induce particle self-assembly while a small-amplitude oscillatory shear (SAOS) was imposed (the details and motivation of the SAOS test during this step will be depicted later), and IV) finally, by steadily increasing the shear rate from 0.1 s^{-1} to 1000 s^{-1} a rheogram is obtained to determine the yield stress of the MR fluid.

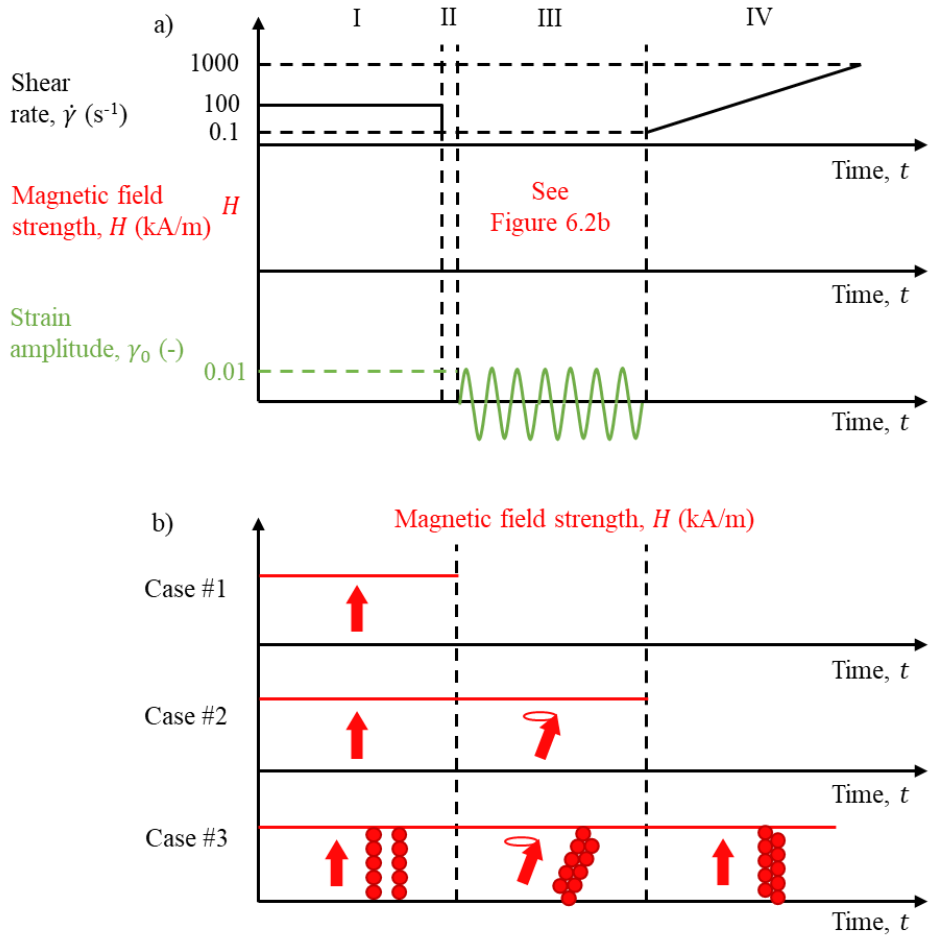

Figure 6.2 Schematics of the (a) rheological tests and (b) the magnetic field configuration protocol used both in the rheological tests as well as for the simulation protocol. For the rheometry tests first the MR fluid sample is presheared at $\dot{\gamma} = 100$ s^{-1} for 60s to ensure all particles are well dispersed and suspended. Next, the suspension is structured at rest for 5 seconds. Then the field configuration is applied. The complete field configuration consist of three field intervals, i) first a uniaxial DC field applied in the z-axis, ii) then the unsteady precession field, and iii) finally a uniaxial DC field is applied to reorient the structures in the z-axis. The last uniaxial DC field is maintained throughout the subsequent shearing interval where rheograms are produced as the shear rate increases from $\dot{\gamma} = 0.1$ s^{-1} to $\dot{\gamma} = 1000$ s^{-1}.

The three field configurations studied in this work are shown in Figure 6.2b. To summarize, we define Case #1 as our baseline case, which consists solely of a traditional uniaxial DC field applied in the z-axis to structure our basic columnar structures in line with the external field. Case #1 is our reference that Case #2 and Case #3 build on. Case #2 consists first of the uniaxial DC field applied in the z-axis followed by the precession field interval. Note that in Case #2 the precession field is maintained during the subsequent steady shearing step IV to study the MR response while the unsteady field is being applied. Lastly, Case #3 is the complete successive train of field intervals. In Case #3, first a uniaxial DC field is applied in the z-axis, then follows the precession field interval, and, finally, a uniaxial DC field is reapplied in the z-axis to reorient the newly fortified structures in the vertical direction prior to the start of the steady shearing step IV. Having the fortified structures stationary and fixed in the vertical position prior to being sheared allows us to directly compare any MR enhancements arising under precession fields with the baseline Case #1. This same nomenclature for defining each of the three cases is also used in the start-up simulation analysis in Section 6.4.1.2.

During step III a SAOS was imposed on the structuring MR fluid to explore the structural evolution over the course of the magnetic field configuration intervals by analyzing the storage modulus G'. The SAOS tests were done by applying a strain amplitude of $\gamma_0 = 0.01$ with a frequency of $f = 1$ Hz. When applying a SAOS we are concerned with not prematurely fracturing the structures while they are structuring under the magnetic field configuration. Under a SAOS a single chain is also expected to be strained. In a plate-plate geometry a single chain oriented in the vertical direction will experience greater strain along the radius of the plate the further out from the center reaching a maximum at the plate border. We can calculate the maximum angle of deviation with respect to the vertical axis a single linear chain will be deformed in a plate-plate geometry as $\theta' = \tan^{-1}[(2r'/h)\sin(\gamma_0 h/2r')]$. Here r' is the distance of the chain from the center of the plate, and h is the plate-plate gap. The direction of the chain will also oscillate back and forth under an oscillatory shear. We can estimate a new Mn for a chain under this oscillatory motion in a parallel plate geometry by substituting θ' into Eqn. 6.6 through $\omega = 2\pi f\theta'$ [12] and acknowledging that for small strain amplitudes the deviation angle can reduce through small angle approximations to $\theta' \approx \gamma_0$ resulting in the following equation:

$$\mathrm{Mn} = \frac{288\,\eta\pi f\gamma_0}{\mu_0 M^2} \tag{6.7}$$

A chain located at the plate border ($r' = 10$ mm) under SAOS and a 5.6 kA·m^{-1} field strength will have a maximum Mn = 0.0005 reaching an angle of deviation $\theta' = 0.57^{\circ}$. Given that Eqn. 6.7 does not depend on r' for small strain amplitudes, we can conclude that all structures exposed to a SAOS by applying a strain amplitude of $\gamma_0 = 0.01$ with a frequency of $f = 1$ Hz will not prematurely fracture given that all structures within the confines of the 20 mm plate diameter will have a Mn $\ll 1$.

Preliminary experiments were done to determine an appropriate time scale for each field interval in step III. Ultimately, 120 seconds was chosen because according to the G' data the structural evolution in each interval was determined as reaching steady-state when the G' curve sufficiently plateaued.

6.4 Results and discussion

6.4.1 Simulations

6.4.1.1 Field driven structuration

In this section we discuss the structuration of MR fluids under the presence of a sequence of steady and unsteady magnetic fields (see Figure 6.3).

Figure 6.3a shows the structuration process under a steady magnetic field. We plot the number of isolated particles N_i, number of clusters N_c, average cluster size S, and linearity Ln of the induced aggregates versus reduced time t for the N randomly configured particles in the presence of a uniaxial DC field. Figure 6.3a is divided into three sectors to break down the proposed mechanism for aggregate formation of a concentrated system in a uniaxial DC field. Sector A, $t = 0$ to $t = 0.3$, can be considered the small cluster formation period. During this short time the average cluster size increases from 2 to 3 and the number of clusters reaches a maximum. Due to the compact nature of the original particle distribution, these small clusters can take the shape of single-particle width chains or, more likely, clusters with mutually tangent particles in a "zippered" formation, which accounts for the initial linearity decrease in this sector. Sector B, $t = 0.3$ to $t = 1.7$, is when elongation occurs as small clusters attract

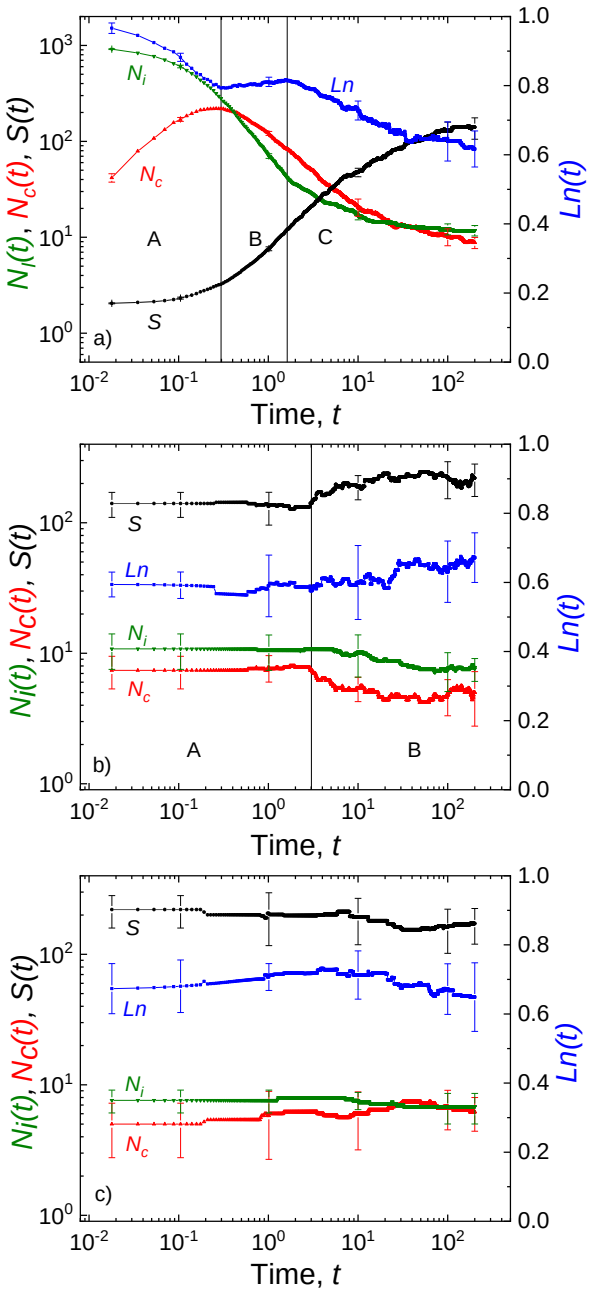

Figure 6.3 Simulated field driven structuration for N particles suspended in a 20 vol% simulation box. A selection of geometry parameters including the number of isolated particles N_i, the number of clusters N_c, the average cluster size S, and linearity Ln are shown first for (a) uniaxial DC field. In this field interval particles organize into anisotropic structures aligned with the external field. Then, during the (b) precession field interval (shown here for a 15º precession field angle, Mn = 0.005) structures coarsen through lateral coalescence. A final (c) uniaxial DC field is reapplied and the structures, for this particular field configuration, stabilize quickly.

neighboring small clusters and isolated particles increasing the average cluster size of the suspension. The constant linearity in this sector supports the mentioned tip-to-tip deterministic aggregation process as there is no indication of lateral coarsening as the average cluster size continues to increase. Sector C gives us an insight into the lateral coalescence aggregation dynamics that occur when a uniaxial DC field is imposed on a MR fluid. During this period, $t >$ 1.7, the average cluster size increases as the number of clusters and number of isolated particles decreases, all while the linearity begins to steadily decrease. The decline in linearity in Sector C suggests that lateral coalescence begins prior to the suspension being completely saturated with isolated linear columns spanning the boundary gap. The average cluster size has not yet surpassed the 13 particle box limit, which would indicate the presence of aggregates large enough, if linear, to span the length of the simulation box, however this is not the case. Moreover, a decay ratio $\kappa = 100/D$ in the exponential repulsive forces between particles was chosen for this reason, to more accurately simulate the likelihood of lateral coalescence early on in the structural evolution of particle aggregates. Aggregates in high concentrated MR fluids in experimental work would certainly laterally coalescence prior to the formation of a single particle width chain spanning the full depth of the sample chamber or rheometer plate gap. Lateral aggregation continues until a stable structure is reached as indicated by the plateauing average cluster size curve. The average cluster size grows above the box limit for linear chains, and the linearity continues to fall as well as the number of isolated particles and number of clusters. A general depiction of the structural evolution promoting lateral coalescence following the application of a precession field is shown in Figure 6.4a and an outlined segment of the 3D model structure in Figure 6.4b displays the vertically oriented aggregate in the aforementioned “zippered” formation.

Although these particle-level simulations are done in a 3D space and at high concentrations, we can still identify similarities with previous studies done simulating a low concentration MR fluid [22,23], and also compare the results with the extensively studied aggregation dynamics for uniaxial DC fields in a 2D plane [24,25]. First, by comparing the magnetic interaction energy between two magnetic moments to the thermal energy we can define the following ratio, $\lambda = \pi\mu_0\mu_{cr}\beta^2\alpha^3H_0^2/2\kappa_{\mathrm{B}}T$. For small values $\lambda \ll 1$ particle aggregation is diffusion-limited as the magnetostatic interaction energy between particles is not sufficiently large enough to undergo traditional dipole-dipole interaction aggregation. For our simulation studies $\lambda \gg 1$ to reflect particle interaction in

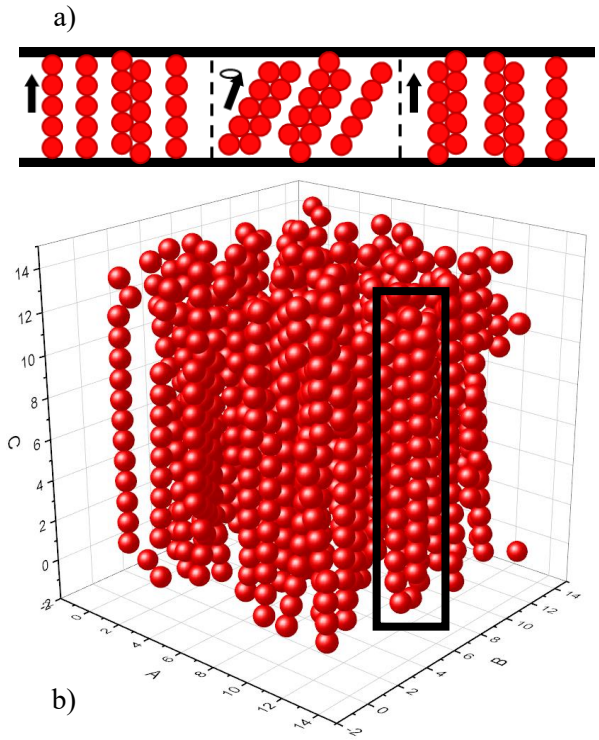

Figure 6.4 a) Schematic of the proposed structural evolution favoring lateral coalescence following the full magnetic field sequence of uniaxial DC field + precession field + uniaxial DC field. b) Simulation model of a $N = 1000$ particle system (20 vol% concentration of particles) taken following the initial uniaxial DC field interval. The outlined area shows two laterally coalesced chains in a "zippered" formation.

conventional MR fluids. Climent *et al.* (2004) shows the impact of their λ ratio on a 0.3 vol% particle concentration [22]. When $\lambda = 1$ the particles remain isolated and do not form aggregates as the magnetic interaction energy is still too weak for the low concentration randomly dispersed particles to attract one another. However, for $10 < \lambda < 10^4$ the cluster size begins to increase linearly with time on a logarithmic scale. The power law scaling of the cluster size $\langle S(t) \rangle \sim t^z$ yielded an exponent ranging from $z = 0.55$ to $z = 0.70$ with increasing λ. In Sectors B and C of Figure 6.3a we similarly witness power-law behavior for N_i, N_c and S. The power law scaling for S is shown to have an exponent $z = 0.92$, clearly above the values reported by Climent. Moreover, the onset of this power-law behavior subsequently follows the small cluster formation time region and lasts one full decade, which is in agreement with their results. For a high concentrated system, lateral coalescence dominates the aggregation process following the end of the power-law

behavior of the average cluster size. This is noted by the change in inflection of the curve at $t = 3.1$, which begins to level out as the structure of thick chain bundles ultimately stabilizes within the box confinement. The curve levels to an average cluster size of 140 ± 40 particles, or around 10 laterally coalesced, or partially coalesced, chains. Shahrivar *et al.* (2017) show the onset of this change in inflection of the mean cluster size after 100 s for their dilute 2D CI suspension ($\phi_{2D} = 0.0239$) in a 500 μm width microchannel (see Figure 3 in their paper) [24]. For comparison with another 2D simulation study, Domínguez-García *et al.* (2007) reported a power law behavior for the mean cluster size with an exponent $z = 0.77$ for a higher particle concentration of $\phi_{2D} = 0.12$ [25].

Figure 6.3b shows the influence of a precession field ($\theta_f = 15°$, $\mathrm{Mn} = 0.005$) on the self-assembled structure after an initial uniaxial DC field. At short times the parameters studied do not drastically change from the final configuration of the uniaxial DC field. For times $t > 3$ the Ln does trend upwards, which is contrary to what we expect. However, there are signs to suggest lateral aggregation is taking place given the decrease in N_c and an increase in S. In addition to aggregate coarsening, the uptick in linearity can be explained by possible chain aggregate elongation. A precession field increases the spanning distance between two hard boundaries, albeit subtle for a small θ_f. Of course, a larger precession angle could facilitate tip-to-tip chain elongation. However, when discussing low angle simulated precession fields, chain elongation is more likely the result of chain defects (individual particles oriented laterally to chains) restructuring as the aggregates "open" when tilted to be in line with the external field at θ_f. Furst and Gast reported on the restructuring of various defect types, such as satellites, cruciform, and double cruciform by applying a strain on a single chain [26]. The applied strain produces a linear tension on the chain that facilitates the incorporation of satellite particles into the body of the linear chain. The restructuring of chain defects into the lateral axis of the chain aggregate eliminates the localized weakness, thus strengthening the structure and would increase the overall linearity of the structure.

Finally, in Figure 6.3c we show the influence of a uniaxial DC field on the self-assembled structure after a sequence of uniaxial DC field + precession field. It is no surprise that the transition between a low angle $\theta_f = 15°$ precession field and a uniaxial DC field has very little impact on the simulated aggregate structures. All the measured parameters are relatively constant over the entire

simulated testing time. Considering the small distance that the chain bundles travel from a $\theta_f = 15°$ axial tilt to a $\theta_f = 0°$ vertical position, neither a radical rearrangement of particles nor additional chain coarsening is expected to derive from this abrupt field transition. The aggregates simply rotate to be in line with the external uniaxial DC field in the vertical position and immediately assume a stable structure. An experimental test replicating this field transition with a low concentration CI suspension confirms that the chain structures instantaneously realign vertically, forming a stable uniform distribution of chains that appear thicker in diameter compared to a baseline uniaxial DC field application, as seen in Figure 6.5c. While the transition between a low angle precession field and a uniaxial DC field may appear rudimentary, the transition from a high angle $\theta_f > 60°$ precession field is more complicated, and even more so working with high Mn where time-averaged magnetostatic interactions drive the formation of more complex structure types. Terkel *et al.* (2020) show segmented structures and wavy sheet structures of varying density due to this abrupt field transition from high angle precession fields with different Mn to a $\theta_f = 0°$ uniaxial DC field [27]. We continue this discussion in a more thorough analysis of the average cluster size.

A particularly interesting estimator of chain thickening is the average cluster size (see Figures 6.4a and 6.4b). We narrow our focus to the small precession angles $\theta_f < 45°$ for a low Mn $= 0.005$ case as the linear chain character of the aggregate structures is sustained throughout the entire sequence of uniaxial DC field + precession field + uniaxial DC field configurations. As expected from the discussion above, there is a similar trend in the average cluster size for these precession angles at the end of the precession field and at the end of the subsequent uniaxial DC field. The average cluster size is for the most part preserved during the small rotational movement of the chains from a slight axial tilt to the vertical position. The average cluster size peaks at $\theta_f = 15°$ with the aggregates averaging 200 ± 40 particles in size at the end of the precession field interval and at $\theta_f = 10°$ with 210 ± 40 particles in size following the final uniaxial DC interval. As alluded to earlier, smaller Mn leads to longer interaction times between neighboring chains in precession motion thus allowing sufficient time for chains to laterally coalesce. The precise reason as to why the average cluster size peaks during a precession field at $\theta_f = 15°$ for a 20 vol% simulation is less clear, although the following two arguments must be integral in understanding the optimized aggregation dynamics: first, an $\theta_f = 15°$ axial tilt can bring neighboring chains from an in-registry to

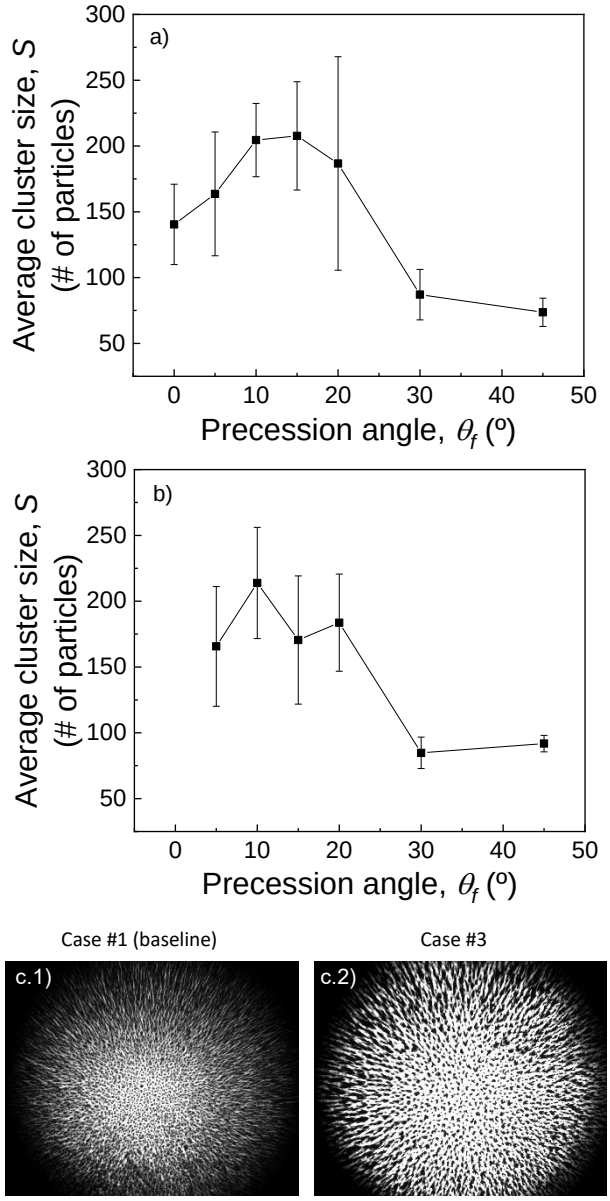

Figure 6.5 Final average cluster sizes S versus precession angle θ_f for Mn = 0.005 (a) at the end of the precession field interval, and (b) at the end of the following uniaxial DC field. For low angle precession fields aggregates keep their chained structure. In the low angle range aggregates reach a maximum cluster size under a 15º angle precession field at the end of the AC field interval. For low Mn there is a longer interaction time between neighboring chains which promotes lateral coalescence and the formation of larger clusters. In (c) we show thicker chain aggregates formed after a 15º precession field is applied on a 1 vol% concentration CI suspension.

out-of-registry spatial configuration that promotes lateral coalescence at small interchain distances [28], and second, for such a high volume particle concentration the $\theta_f = 15°$ precession movement could lead to lateral coalescence due to a more direct collision contact of neighboring chains.

Experimentally it is difficult to capture lateral coalescence of a 20 vol% MR fluid using traditional optical microscopy techniques as light cannot penetrate such densely packed structures. Terkel *et al.* (2020) outlines a meticulous process for solidifying high concentrated structures in PDMS that are then later imaged using x-ray microtomography [27]. In this work to reveal the structural changes as a result of inducing a precession field we have simply captured a top view of our CI suspension before and after a $\theta_f = 15°$ precession field using a reduced 1 vol% CI suspension as shown in Figure 6.5c. At the center of the images the individual black dots represent a top view of vertical chains spanning the depth of the sample chamber. One can easily deduce that the precession field yielded thicker chains as the black dots in the second image are thicker in diameter and there is a greater separation distance between neighboring chain bundles.

6.4.1.2 Start-up simulations

The particle dynamics simulations shown in Figure 6.5a and 6.4b have indicated that a precession motion at a $\theta_f = 15°$ maximized the increase in average cluster size compared to the uniaxial DC field simulation set-up. To further understand the effect precession motion has on enhancing the rheological response of a MR fluid, a more complete and in-depth study was done for a $\theta_f = 15°$ precession field simulation. It was designed to compare the yield stress response as well as observing other relevant geometry parameters including N_i, N_c, S, Ln, Zn, and $C(\theta)$. In this discussion, emphasis will be made on comparing and contrasting the results of Case #1 and Case #3 shear simulations, which correspond to the interval at which the start-up shear interval is applied, in the former Case #1 after a uniaxial DC field interval and in the latter Case #3 following the complete sequence of uniaxial DC field + precession field + uniaxial DC field configuration intervals. These simulations were designed such that we could easily replicate them experimentally using the triaxial field generator, as well as clearly attribute any yield stress enhancement to the precession motion itself as it is the only differentiating factor between Case #1 and Case #3.

Upon initial inspection of the stress and geometry parameters versus strain curves it became clear that the degeneration of the field induced microstructure follows a similar trend independent to the shear rate. Figure 6.6a shows the stress versus strain curves comparing Case #1 and Case #3 shear simulations for a shear rate of 1 s^{-1}, with the other shear rate curves shown in the Supplementary Material. We can calculate the shear modulus, G, from the slope of the stress-strain curve in the linear viscoelastic region (small strains). Case #1 and Case #3 have a shearing modulus of $G = 0.74$ and $G = 0.78$, respectively. The larger shearing modulus for Case #3 indicates a more solid-like behavior, meaning the structures must be stronger and more resilient to shearing deformation.

From the data shown in Figure 6.6a the static yield stress was determined as the maximum point of the stress versus strain plots. The dynamic yield stress was also computed from this plot by visual inspection of the stress plateau at high strains and averaging these stress values from the plateau onset to the end of the simulated interval. For each tested shear rate the static yield stress is consistently larger for the Case #3 simulated trials, and increases linearly with the shear rate as seen in Figure 6.6b. The static yield stress peaks at a strain of γ = 0.39 for both Case #1 and Case #3 at all shear rates tested. For this particular strain, a zenithal angle of 21.3º is calculated from $\alpha = \tan^{-1}(\gamma)$. This is consistent with the plateau of the zenithal angle at a similar angle in Figure 6.7a (see below).

There is, however, no distinct difference between the Case #1 and Case #3 dynamic yield stresses due to a similar fractured state of the aggregate structures near the onset of the dynamic yield stress plateau. For high strains in both cases 3D models would suggest that near the onset of the dynamic yield stress plateau the aggregates have already fractured to low particle number clusters or even reduced completely to isolated particles. Moreover, the number of isolated particles and the average cluster size curves in Figure 6.7a reach a minimum and maximum, respectively, at the onset of the dynamic yield stress plateau further supporting a similar structure breakdown. If both Case #1 and Case #3 aggregates similarly fracture to simple structures then we would not expect a big difference in the dynamic yield stress region.

Figure 6.7a furthers our understanding of the aggregation dynamics and fracturing under a start-up test. In this figure we show the evolution of the structural parameters with strain. The increase in N_c and decrease in S during

the linear regime prior to the yield stress peak reflects the idea that laterally aggregated chains are disconnecting during these early shear times. We speculate that strained structures are more susceptible to lateral offsets between neighboring chains. Even a minor lateral offset of one particle radius in length can spatially change two off-registered chains to an in-registry position, which

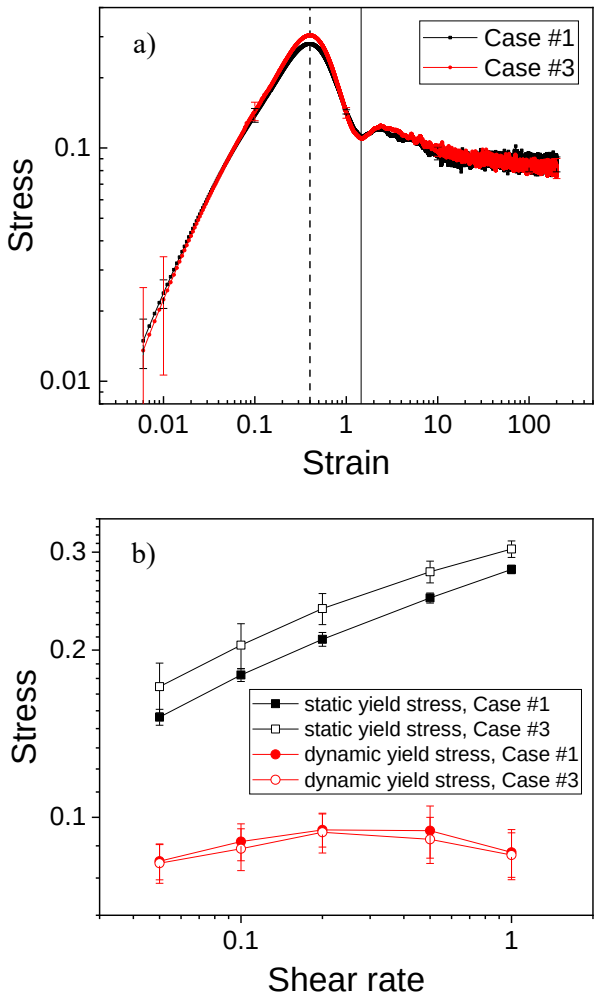

Figure 6.6 (a) Stress-strain curves for Case #1 and Case #3 ($\theta_f = 15°$, Mn $= 0.005$) structures under a shear rate $\dot{\gamma} = 1$ s^{-1} simulated start-up test. The shearing behavior is similar between each case. The static yield stress (dashed vertical line) and the onset of the dynamic yield stress plateau (solid vertical line) are summarized in (b) for varying shear rates $\dot{\gamma} = 0.05$ - 1 s^{-1}. The static yield stress is consistently larger for Case #3 structures, indicating they are more robust to deformation. The dynamic yield stress for both Case #1 and Case #3 are more or less equal pointing out that in each case the applied strain breaks down the structures to a similar state.

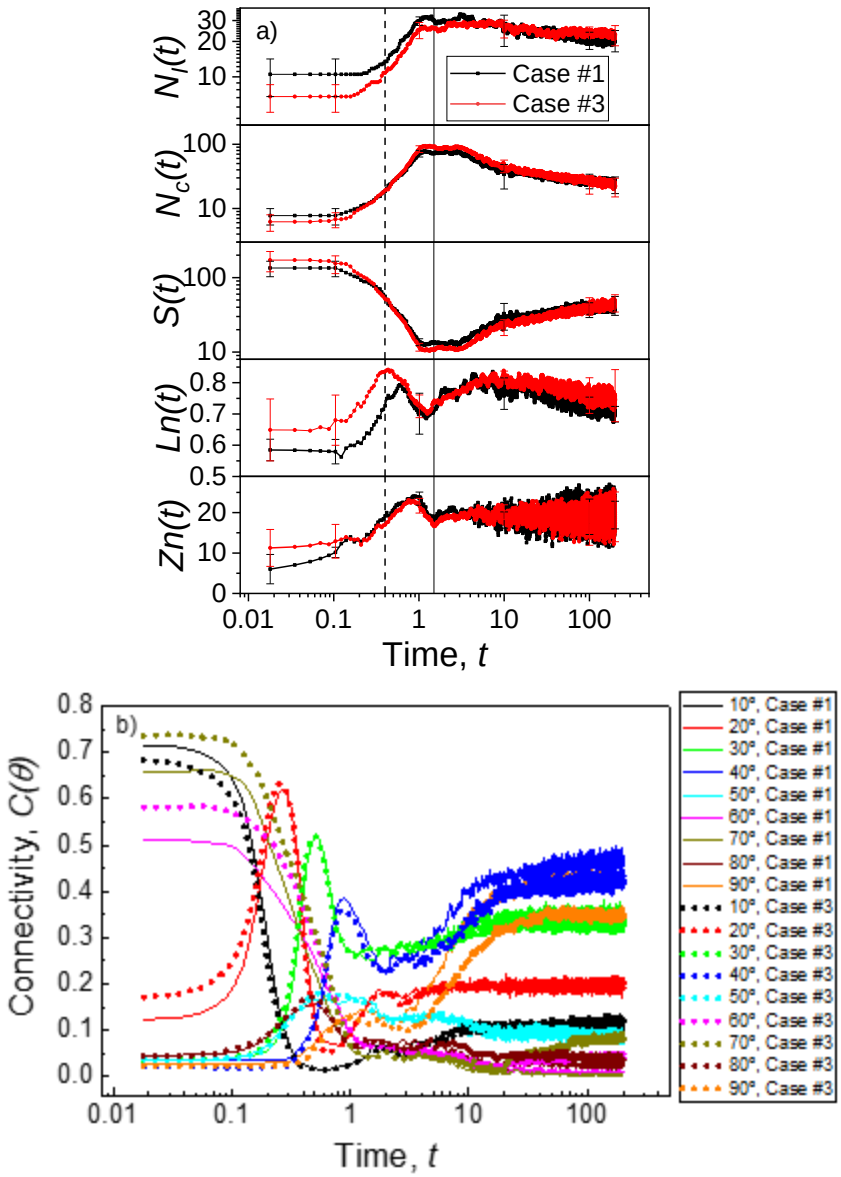

Figure 6.7 (a) A selection of geometry parameters display the fracturing process of aggregate structures during a simulated start-up test. Case #3 field configurations were run with a $\theta_f = 15°$ precession field and Mn $= 0.005$. As the strain increases with time the average cluster size decreases as aggregates fracture and number of clusters increase. The increase in linearity at early times is due to aggregates losing lateral connections when a constant shear rate (1 s^{-1}) is applied. (b) A detailed display of the particle connectivity evolution during the start-up test. At early times the 10º, 60º, and 70º connectivities are high representing the presence of aggregates oriented in the vertical direction and lateral connections between chains in a "zippered" formation. These lateral connections (60º, 70º) are greater for the Case #3 (dashed lines) structures, indicating precession fields promote lateral coalescence behavior.

would drastically change the force interaction between chains from being attractive to repulsive. Continuing, the linearity peaks with the static yield stress. Prior to the yield stress peak in the linear regime we expect the aggregates do not fracture in length, therefore an increase in linearity during this shearing period likely concerns thick aggregates (consisting of multiple gap-spanning linear chains) losing their lateral connections, as well as satellite particles integrating into the central body of the chain. As mentioned, a maximum zenithal angle of around 20º is reached before the chains begin to fracture, first near the shearing boundary where the interparticle strain is greatest.

Tracking the particle connectivity during the shearing step of the simulation supplements our understanding of strained aggregates and gives rise to a peculiar trend occurring at high strains. Figure 6.7b illustrates the connectivity for all angles comparing Case #1 and Case #3 simulations for a shear rate of 1 s^{-1}. At early times (low strains) we can interpret the connectivity data as a means to understand the final structural evolution of the Case #1 (solid lines) and Case #3 (dashed lines) field configurations that were imposed prior to the shearing step. At low strains connections at 10º, 60º, and 70º are highly present for both cases. This represents that the aggregates are predominantly aligned in the vertical position (10º) and the accompanying angle positions (60º, 70º) are indicative of the lateral coalescence of chains with an out of register alignment in a “zippered” formation. Moreover, inspection of Figure 6.7b shows that at low times the 60º and 70º curves are greater for the Case #3 simulation than Case #1. This confirms that there is more lateral connectivity between aggregates forming during the precession field interval yielding larger clusters. We believe thicker initial clusters are one aspect of the starting conditions that produces a higher yield stress peak for Case #3 as shown in Figure 6.6b. More interconnectivity amongst aggregates restricts fluid flow and bolsters fracturing resistance of the aggregates to induced strain. Continuing, the successive rise and fall of the 20º, 30º, and 40º curves indicates that the chains are in fact tilting as the strain increases. At large strains we see a rise in the horizontal connectivity (90º) and its complimentary “zippered” formation connections (30º, 40º). This is due to the interesting shear banding phenomenon experienced by MR fluids under shear [29].

There is not a sizable difference in the 10º angle connectivity between Case #1 and Case #3 at early times. This is not due to a lack of enhanced aggregation dynamics with the presence of a precession field, but rather a limitation set by

the box size of the performed simulation. The box has hard top and bottom boundaries and it is understood that after the first uniaxial DC field interval the system is saturated with gap-spanning aggregates and has reached a maximum 10º angle connectivity and therefore any cluster size increase is due to lateral coalescence.

6.4.2 Experimental

6.4.2.1 Linear viscoelasticity under field driven structuration

SAOS tests were carried out during the structuration process (prior to the start-up shearing tests) in order to monitor the structural evolution of MR fluids in the presence of the three distinct field configurations. The storage modulus, G', captures the solid-like characteristics of the MR fluid arising from the application of an external magnetic field on the MR sample. We run these SAOS tests to obtain qualitative information about the MR response to the magnetostatic interactions at play without prematurely fracturing the structuring aggregates. Under the influence of an external magnetic field, columnar aggregates spanning the top and bottom plates consisting of a complex network of interconnected laterally aggregated chains impede fluid movement and thus leads to the apparent yield stress increase due to this flow restriction and the particle structure itself.

The experimental storage modulus behavior of the field induced structures is shown in Figure 6.8. The plot is partitioned into the three field configurations (see Figure 6.2b). First, the sample structures under a 5.6 kA·m^{-1} uniaxial DC field in the z-axis for 120 seconds. Then, the precession field is applied with a $\theta_f = 15°$ angle movement for 120 seconds while maintaining the 5.6 kA·m^{-1} field strength. Finally, the precession field is suppressed and another 120 seconds of a 5.6 kA·m^{-1} uniaxial DC field is applied. Again, a precession field with $\theta_f = 15°$ was chosen for a more in-depth study as the simulation work showed an average cluster size peak for this angle of precession. The clear increment in the G' between the first and second interval of uniaxial DC field (separated by the precession field interval) strongly proposes a key structural evolution takes place during the precession field interval. It is during this interval that the aggregation dynamics favor lateral coalescence of chains and chain bundles into thicker chain bundles as well as possible chain lengthening, which combined we attribute the storage modulus increase in the final uniaxial

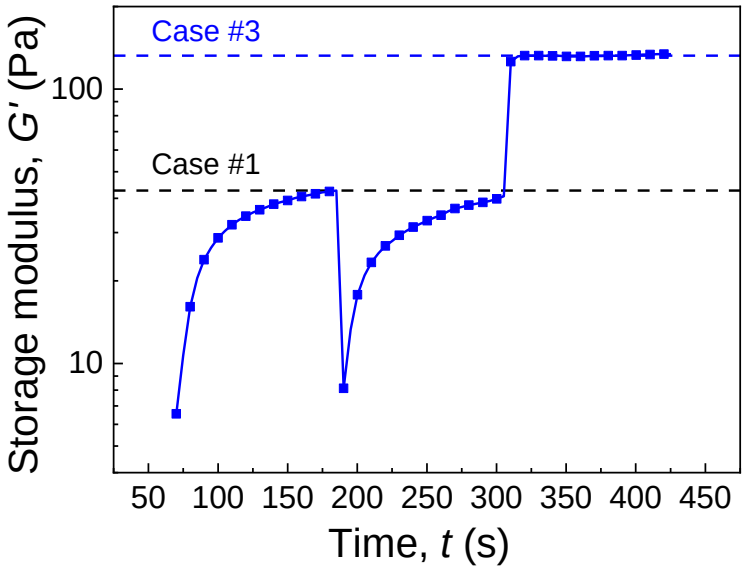

Figure 6.8 SAOS test during step III in Figure 2 of a CI particle suspension ($\phi = 0.20$). We observe a clear increase in the storage modulus, G', for the Case #3 ($\theta_f = 15°$, Mn $= 0.5$) field configuration if compared to Case #1. A greater G' response means the Case #3 structures are sturdier and more robust to fracturing under controlled strain.

DC interval. Also, the transition between the precession field interval and the final uniaxial DC interval is notably very fast and the G' immediately plateaus at its final value. This is consistent with the simulation data and low concentration aggregation experiments discussed in Section 6.4.1.1 in which those structures also immediately formed a stable structure oriented in the vertical direction following the field transition.

6.4.2.2 Steady simple shear

In this section we show the steady shear rheological behavior of the structured MR fluids. In Figure 6.9 we show results for Case #1, Case #2 and Case #3 tests. The enhancement of the stress in Case #3 if compared to Case #1 must be a result of the structuration of the MR fluid due to the $\theta_f = 15°$ precession field configuration interval. The precession field applied to our CI colloidal suspension must have yielded coarsened structures that bolstered their resistance to chain fracturing. A microstructure consisting of vertically-oriented chains benefits from having interchain connections. The shearing

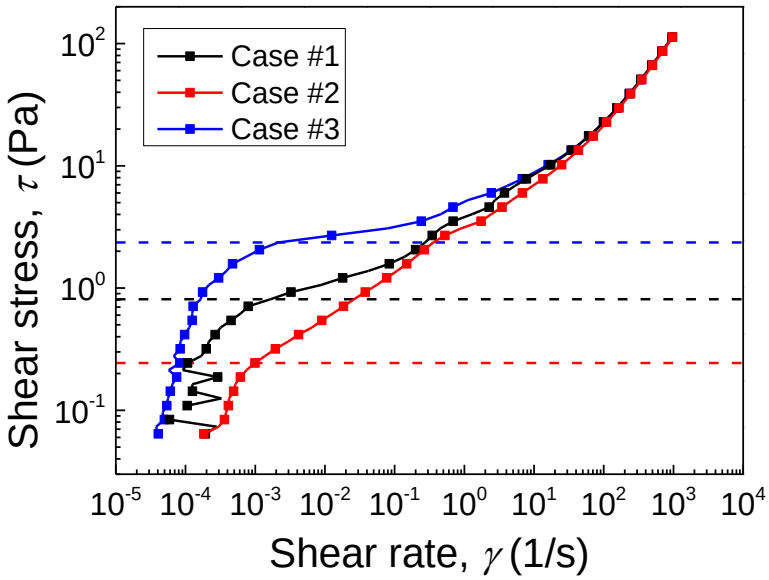

Figure 6.9 Experimental steady shear flow curves for Case #1, Case #2 and Case #3 field configurations on a 20 vol% concentration CI suspension. The horizontal dotted lines indicate the static yield stresses for each case. As expected, Case #3 results in the largest static yield stress. Case #2 dips below the others because the shear measurements we captured during the precession field interval, where structures could potentially disconnect from the top and bottom plates of the rheometer and thus weaken the measured response.

force must simultaneously rupture the interchain connections and fracture the chains along their lateral axis, thus leading to the increase in the stress of these strengthened MR fluids. The stress values for Case #2 are lower in comparison to both Case #1 and Case #3. We theorize that some aggregates may disconnect from the top and bottom surfaces of the plate-plate rheometer setup while exposed to a precession field (with the uniaxial DC field component aligned orthogonal to the shearing surface) and therefore consequently repressing the shear stress response while the precession field is active.

6.5 Conclusions

It has been determined that precession magnetic fields can drive the formation of thicker chain bundles, which ultimately leads to an increase in the MR response of the fluid. We propose that lateral chain coalescence in high particle concentration MR fluids is motivated by the combination of out-of-registry chains in close proximity aggregating due to attractive magnetostatic

interactions as well as direct chain collision contact. Low Mn precession fields increase the likelihood of structuring thicker and more robust chains given the additional interaction time between neighboring chains in precession motion. Additional, geometry parameters including particle connectivity were studied in the simulations to compare the static and dynamic yielding behavior of structured systems for both the uniaxial DC field only and precession field cases. Experiments were in agreement with the particle level simulations, as observed by the stress increase of the tested CI suspension following the complete sequence of uniaxial DC field + precession field + uniaxial DC field for a low angle $\theta_f = 15°$ precession field.

A foreseeable extension into the investigation of unsteady magnetic fields and their impact on rheological behavior will concern a greater range and diversity in triaxial field control. Furthermore, MR enhancement beyond lateral coalescence is also being studied – particle compactness within aggregate structures can also be controlled using unsteady triaxial magnetic fields.

Supplementary Material

A selection of geometry parameters display the fracturing process of aggregate structures during a start-up test for the other simulated shear rates $\dot{\gamma}$ = 0.05 - 0.5 s^{-1}. Case #3 field configurations were run with a $\theta_f = 15°$ precession field and Mn = 0.005. These curves show similar trends displayed in Figure 6.7a.

Acknowledgements

This work was supported by MICINN PID2019-104883GB-I00 project (Spain) Junta de Andalucía P18-FR-2465 project and European Regional Development Fund (ERDF). M. Terkel acknowledges BES-2017-079891 fellowship.

References

[1] Martin, J. E., and A. Snezhko, "Driving self-assembly and emergent dynamics in colloidal suspensions by time-dependent magnetic fields," Rep. Prog. Phys. **76(12)**, 126601 (2013).

[2] de Vicente, J., D. J. Klingenberg, and R. Hidalgo-Alvarez, "Magnetorheological fluids: a review," Soft Matter *7***(8)**, 3701-3710 (2011).

[3] Morillas, J. R., and J. de Vicente, "Magnetorheology: a review," Soft Matter **16(42)**, 9614-9642 (2020).

[4] Ulicny, J. C., K. S. Snavely, M. A. Golden, and D. J. Klingenberg, "Enhancing magnetorheology with nonmagnetizable particles," Appl. Phys. Lett. **96(23)**, 231903 (2010).

[5] Wereley, N. M., A. Chaudhuri, J. H. Yoo, S. John, S. Kotha, A. Suggs, ... and T. S. Sudarshan, "Bidisperse magnetorheological fluids using Fe particles at nanometer and micron scale," J. Intel. Mat. Syst. Str. **17(5)**, 393-401 (2006).

[6] de Vicente, J., J. P. Segovia-Gutiérrez, E. Andablo-Reyes, F. Vereda, and R. Hidalgo-Álvarez, "Dynamic rheology of sphere-and rod-based magnetorheological fluids," J. Chem. Phys. **131(19)**, 194902 (2009).

[7] Bombard, A. J., F. R. Gonçalves, J. R. Morillas, and J. de Vicente, "Magnetorheology of dimorphic magnetorheological fluids based on nanofibers," Smart Mater. Struct. **23(12)**, 125013 (2014).

[8] Morillas, J. R., A. J. Bombard, and J. de Vicente, "Magnetorheology of Bimodal Fluids in the Single–Multidomain Limit," Ind. Eng. Chem. Res. **57(40)**, 13427-13436 (2018).

[9] Tang, X., X. Zhang, R. Tao, and Y. Rong, "Structure-enhanced yield stress of magnetorheological fluids," J. Appl. Phys. **87(5)**, 2634-2638 (2000).

[10] Ruiz-López, J. A., R. Hidalgo-Alvarez, and J. de Vicente, "A micromechanical model for magnetorheological fluids under slow compression," Rheol. Acta **55(3)**, 215-221 (2016).

[11] Ruiz-López, J. A., Z. W. Wang, R. Hidalgo-Alvarez, and J. de Vicente, "Simulations of model magnetorheological fluids in squeeze flow mode," J. Rheol. **61(5)**, 871-881 (2017).

[12] Donado, F., U. Sandoval, and J. L. Carrillo, "Kinetics of aggregation in non-Brownian magnetic particle dispersions in the presence of perturbations," Phys. Rev. E **79(1)**, 011406 (2009).

[13] de Vicente, J., J. A. Ruiz-López, E. Andablo-Reyes, J. P. Segovia-Gutiérrez, and R. Hidalgo-Alvarez, "Squeeze flow magnetorheology," J. Rheol. **55(4)**, 753-779 (2011).

[14] Moctezuma, R. E., F. Donado, and J. L. Arauz-Lara, "Lateral aggregation induced by magnetic perturbations in a magnetorheological fluid based on non-Brownian particles," Phys. Rev. E **88(3)**, 032305 (2013).

[15] Klingenberg, D. J., and C. F. Zukoski IV, "Studies on the steady-shear behavior of electrorheological suspensions," Langmuir **6(1)**, 15-24 (1990).

[16] Fernández-Toledano, J. C., J. Rodríguez-López, K. Shahrivar, R. Hidalgo-Álvarez, L. Elvira, F. Montero de Espinosa, and J. de Vicente, "Two-step yielding in magnetorheology," J. Rheol. **58(5)**, 1507-1534 (2014).

[17] Segovia-Gutiérrez, J. P., J. de Vicente, A. M. Puertas, and R. Hidalgo-Alvarez, "Describing magnetorheology under a colloidal glass approach," Phys. Rev. E **95(5)**, 052601 (2017).

[18] Morillas, J. R., and J. de Vicente, "DEM and FEM simulations in magnetorheology: aggregation kinetics and yield stress," in Magnetorheological Materials and Their Applications **58**, 19 (2019).

[19] Ruiz-López, J. A., J. C. Fernández-Toledano, R. Hidalgo-Alvarez, and J. de Vicente, "Testing the mean magnetization approximation, dimensionless and scaling numbers in magnetorheology," Soft Matter **12(5)**, 1468-1476 (2016).

[20] Fernández-Toledano, J. C., J. A. Ruiz-López, R. Hidalgo-Álvarez, and J. de Vicente, "Simulations of polydisperse magnetorheological fluids: A structural and kinetic investigation," J. Rheol. **59(2)**, 475-498 (2015).

[21] Melle, S., O. G. Calderón, M. A. Rubio, and G. G. Fuller, "Rotational dynamics in dipolar colloidal suspensions: video microscopy experiments and simulations results," J. Non-Newton. Fluid **102(2)**, 135-148 (2002).

[22] Climent, E., M. R. Maxey, and G. E. Karniadakis, "Dynamics of self-assembled chaining in magnetorheological fluids," Langmuir **20(2)**, 507-513 (2004).

[23] Liu, D., M. R. Maxey, and G. E. Karniadakis, "Simulations of dynamic self-assembly of paramagnetic microspheres in confined microgeometries," J. Micromech. Microeng. **15(12)**, 2298 (2005).

[24] Shahrivar, K., E. Carreón-González, J. R. Morillas, and J. de Vicente, "Aggregation kinetics of carbonyl iron based magnetic suspensions in 2D," Soft Matter **13(14)**, 2677-2685 (2017).

[25] Domínguez-García, P., S. Melle, J. M. Pastor, and M. A. Rubio, "Scaling in the aggregation dynamics of a magnetorheological fluid," Phys. Rev. E **76(5)**, 051403 (2007).

[26] Furst, E. M., and A. P. Gast, "Micromechanics of magnetorheological suspensions," Phys. Rev. E **61(6)**, 6732 (2000).

[27] Terkel, M., and J. de Vicente, "Magnetorheology of exotic magnetic mesostructures generated under triaxial unsteady magnetic fields," Smart Mater. Struct. **30(1)**, 014005 (2020).

[28] Mohebi, M., N. Jamasbi, and J. Liu, "Simulation of the formation of nonequilibrium structures in magnetorheological fluids subject to an external magnetic field," Phys. Rev. E **54(5)**, 5407 (1996).

[29] Volkova, O., S. Cutillas, and G. Bossis, "Shear banded flows and nematic-to-isotropic transition in ER and MR fluids," Phys. Rev. Lett. **82(1)**, 233 (1999).

[30] See the supplementary material at https://www.scitation.org/doi/suppl/10.1122/8.0000356 for a selection of geometry parameters that display the fracturing process of aggregate structures during a start-up test for the other simulated shear rates $\dot{\gamma}$ = 0.05–0.5 s^{-1}. Case #3 field configurations were run with a $\theta_f = 15^{\circ}$ precession field and Mn = 0.005. These curves show similar trends displayed in Fig. 6.7a.

Chapter 7

Magnetorheology in unsteady fields: From uniaxial DC to rotating AC fields

Matthew Terkel, Robert Wright and Juan de Vicente

F2N2Lab, Magnetic Soft Matter Group and Excellence Research Unit 'Modeling Nature' (MNat), Department of Applied Physics, Faculty of Sciences, University of Granada, C/Fuentenueva s/n, 18071 Granada, Spain

Published in

JOURNAL OF RHEOLOGY®

J. Rheol. **2023**, 67, 833-848
Selected front cover paper

Abstract

Magnetorheological fluids structured under precession fields are thoroughly investigated. Having complete dynamic triaxial magnetic field control, we are able to study both the structural and magnetorheological response via videomicroscopy and rheometry integration for a wide range of magnetic field configurations, once previously limited to traditional uniaxial fields. Optimal precession fields for driving the formation of more robust particle structures enhancing yield stress response are identified. It is believed that structural reinforcement comes from chain coarsening through lateral chain coalescence and particle compactness within the structures such that a lower energy configuration is found for certain field configurations. Particle level simulations supplement our understanding of lateral chain coalescence and structure strengthening.

7.1 Introduction

The instantaneous response to an external magnetic field makes magnetorheological (MR) fluids one of the most fast reacting smart materials. Typically consisting of micron-sized magnetic particles suspended in a non-magnetic carrier fluid, MR fluids appreciate a drastic increase of multiple orders of magnitude in viscosity in the presence of a magnetic field [1]. This external stimulus induces a magnetic moment in the particles which then drives particle aggregation and structure elongation in line with the external field [2-4]. When magnetized, the structure formation and consequential fluid confinement gives rise to an apparent yield stress, i.e. a minimum shear stress to break the particle microstructure and induce flow [5].

For particles with low coercivity, commonly referred to as being magnetically "soft", the liquid-to-solid transition is reversible making them highly suitable for industrial applications [6]. Dampers and shock absorbers neutralize kinetic energy via field-controlled damping forces, MR fluid braking systems reduce rotary torque through magnetic field strength manipulation, and abrasive MR fluids can be used for surface polishing devices [7-11]. Particle sedimentation and re-dispersibility is a common issue in the design and implementation of commercial MR fluids due to the mismatch between particle and carrier fluid densities. A vast number of studies have been dedicated to optimizing MR fluid formulations to combat particle sedimentation [see Morillas (2020) for a

detailed review on this aspect] [12]. Bidisperse suspensions incorporating micron- and nano-sized magnetic particles reduces the sedimentation rate of the former due to the Brownian energy exerted by the latter [13-15]. Core-shell particles greatly reduce particle density, albeit accompanied by a commensurate loss in magnetization, by isolating the magnetic content to an outer coated layer [16]. Steric stabilization through surfactants and functional groups is known to reduce particle agglomeration in the absence of a magnetic field [17-20]. Ionic liquids, polymeric gels, and fumed silica additives can also be considered for formulating optimal carrier fluids that would impede particle sedimentation [21-27]. While all these studies address the issue of sedimentation, many do not necessarily enhance the MR response. Additionally, certain additives increase the fluid viscosity in the absence of a magnetic field which can be undesirable for certain applications, and can be especially counterintuitive when working with time-dependent fields.

MR fluids have traditionally been studied under uniaxial DC fields using a single coil or a magnetorheometry cell for generating higher field strengths [28-30]. These experimental setups are adequate for forming gap-spanning columnar aggregate structures and measuring the MR response but are limited to that one structure type. Biaxial and triaxial magnetic field configurations have been used to drive the formation of much more exotic aggregate structures [31]. For low frequency rotational and balanced triaxial fields, small chained structures known as micromixers are highly effective at mixing in microchannels or suspensions [32-33]. High frequency rotational fields are known to form disk-like (low particle concentration) and layered structures (high particle concentration) by cause of the time-averaged repulsive interaction orthogonal to the field direction and an attractive interaction in the plane of the field [34-36]. Crosshatched structures are known to form in perturbating fields when directing a uniaxial AC field perpendicular to a uniaxial DC field [37]. Porous foam-like and cellular structures have been fixed in polymerizing resins while subjecting the particle suspension to field heterodyning, a triaxial field configuration with at least two of the field components having nearly identical but distinguishable field frequencies in the time-average interaction regime [31, 38-39]. Moreover, unique snake-like and aster particle clusters form when applying an oscillatory field to particles resting at a liquid-air and liquid-liquid interface, respectively, both with interesting cargo transport capabilities [31, 40-41]. Additionally, recent studies have shown that oscillating fields acting as a mechanical stimulus on magnetic responsive biomaterials can regulate encapsulated cell behavior [42]. Studies

have also shown that a number of these anisotropic mesostructures improve Laplacian properties, including the magnetic susceptibility, thermal conductivity, and electrical conductivity biased in the direction(s) of structure aggregation [31, 39, 43]. In the case of suspended platelet particles, multiaxial fields generate vigorous flow patterns due to the coupled torque and hydrodynamic response of these particles. This phenomena is referred to as Isothermal Magnetic Advection, and certain flow patterns have been suggested to mimic countercurrent heat exchangers with heat and mass transport properties [31, 44].

There are several papers today addressing aggregation kinetics under time-dependent, or unsteady fields. However, the literature on the magnetorheology of structured MR fluids under these field configurations have yet to be explored in a meaningful way in a complete study. Donado *et al.* initially explored the aggregation dynamics under perturbation fields and the viscosity increase of a MR fluid by applying a low angle perturbation field [45-46], and Terkel *et al.* began the study of applying triaxial precession-like magnetic field configurations to enhance the MR response of these fluids [47-48]. In this paper we lay out a complete MR response analysis of our system structured under uniaxial DC to rotating AC including an array of intermediate precession fields. First we introduce the magnetic and hydrodynamic forces at play in our system and define the dimensionless Mason number, Mn, which is crucial for explaining the response of our MR fluid. Then we detail the various structure types one can form by applying precession fields based on our videomicroscopy experiments. Following is the rheometry analysis showing that precession fields do yield an MR enhancement. We end this study with a focused examination of field transitions and a brief discussion of simulation work that supplements our rheometry findings.

7.2 Simulations and Mason number definition

We follow a similar method as previously used by Fernández-Toledano *et al.* (2015) in defining the time evolution of a $N = 1000$ particles suspended in a Newtonian liquid as follows [49]:

$$M_i \frac{d^2\vec{r}_i(t)}{dt} = \vec{F}_h + \vec{F}_i + \vec{F}_B(t) \tag{7.1}$$

where M_i is the mass of a particle, and the three terms on the RHS are the hydrodynamic, particle-particle/particle-wall, and Brownian forces, respectively, acting on our system. The hydrodynamic forces acting on a particle with a radius a in suspension can be defined by Stokes drag force:

$$\vec{F}_h = 6\pi\eta a\left(\frac{d\vec{r}_i(t)}{dt} - \vec{u}_i^{\infty}\right) \tag{7.2}$$

where η is the viscosity of the Newtonian carrier, $\vec{r}_i$ is the particle position, and $\vec{u}_i^{\infty}$ is the fluid velocity at the particle position. To simplify, for non-shearing systems we consider the system as a quiescent suspension ($\vec{u}_i^{\infty} = 0$), although we will later discuss the unique ability of some precession fields to provoke flow in ideal vortex mixing configurations.

The magnetostatic forces are summed up in the force variable, $\vec{F}_i$, as follows:

$$\vec{F}_i(\vec{r}_i) = \vec{F}_i^{mag}(\vec{r}_i) + \vec{F}_i^{rep}(\vec{r}_i) + \vec{F}_i^{wall}(\vec{r}_i) \tag{7.3}$$

where $\vec{F}_i^{mag}$ is approximated as the magnetostatic dipole-dipole force acting on particle i from its interaction with the dipole moments of all the other particles in the system. $\vec{F}_i^{rep}$ is a short-ranged exponential repulsive force between particles accounted for to avoid interpenetration of hard sphere particles. A similar repulsive force, $\vec{F}_i^{wall}$, is also defined to express the short-range interactions between every particle and the hard boundaries.

The force component introduced to the system by Brownian motion, $\vec{F}_B$, is often integral for nanosized particle suspensions where thermal fluctuations dominate the systems behavior. In using micronsized particles in our work, $\vec{F}_B$ can be neglected as we expect a sufficiently large λ ratio, $\lambda = \pi\mu_0\mu_{cr}\beta^2 a^3 H_0^2/2\kappa_B T$, indicating that the magnetostatic particle interactions significantly overcome the motion induced by thermal fluctuations [12].

Unless otherwise specified, the unsteady precession magnetic fields studied in this work consist of an alternating rotational field in the x, y-plane superimposed with a DC field in the vertical z-axis direction:

$$\vec{H} = H_0\{\sin\theta_f\,[\sin(\omega t)\hat{x} + \cos(\omega t)\hat{y}] + \cos\theta_f\hat{z}\} \tag{7.4}$$

Here, θ_f is the precession angle of the field vector deviating from the vertical z-axis, $\omega = 2\pi f$ is the angular speed and f is the frequency of the rotating field. In the presence of a low-strength external field, a magnetic dipolar moment is induced in the particles in line with the field:

$$m = \frac{4}{3}\pi a^3 M \tag{7.5}$$

where the particle magnetization $M = \chi H_0$ and the magnetic susceptibility defined as $\chi = 3\beta = 3(\mu_{pr} - \mu_{cr})/(\mu_{pr} + 2\mu_{cr})$, μ_{pr} is the relative permeability of the particles, and μ_{cr} is the relative permeability of the continuous phase. Carbonyl iron particles (CIPs) employed in this work have a contrast factor $\beta = 0.65$, with similar values previously reported by Gorodkin (2009) and Shahrivar (2017) [50-51].

We can define the force interaction between two magnetic dipoles, $\vec{m}_1$ and $\vec{m}_2$, induced by a stationary field as follows:

$$\vec{F}_2^{mag} = \mu_0 \nabla(\vec{m}_2 \cdot \vec{H}_1) \tag{7.6}$$

Here the magnetic field, $\vec{H}_1 = 1/4\pi r^3\,[3(\vec{m}_1 \cdot \hat{r})\hat{r} - \vec{m}_1]$, acting on $\vec{m}_2$ is induced by the point dipole $\vec{m}_1$, where $\mu_0 = 4\pi \times 10^{-7}$ Tm A^{-1} is the permeability of a vacuum, and r is the distance between dipoles. In this case that $m_1 = m_2 = m$ and the dipoles are aligned with the z-axis, we can define the general force vector between two dipoles $\vec{F}^{mag}$:

$$\vec{F}^{mag} = -f_c\left[(3\cos^2\theta - 1)\hat{r} - \sin 2\theta\,\hat{\theta}\right] \tag{7.7}$$

where $f_c = (3\mu_0/4\pi r^4)m^2$ is the force prefactor, and θ is the angle between the line of centers of the dipoles and the direction of the dipoles.

Let us move now to the case of unsteady magnetic fields, in particular precession fields. For a single particle width chain with a particle at the origin and two half chain segments of N particles each (see Figure 7.1), the velocity of particle j from the origin can be defined as $v_j = \omega R_j \hat{\phi}$ where $R_j = (2j - 1)a \sin\theta_f$. The hydrodynamic force between two particles j and j+1 can

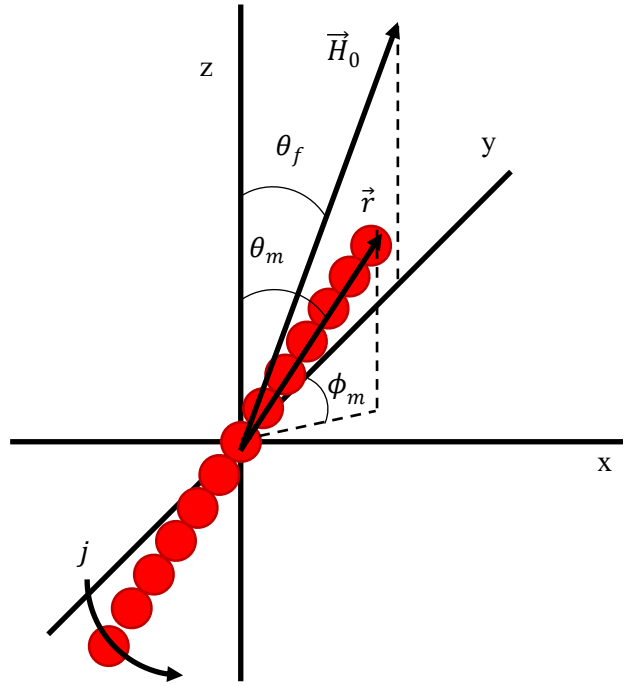

Figure 7.1 Schematic of the chain and field vectors for a chain in a precession field. The curved arrow on particle j indicates the direction of precession. The velocity, and thus the viscous drag acting on a particle in a chain, increases further out from the origin. As the hydrodynamic forces overcome the magnetic forces, the chain vector drags behind the field vector at the azimuthal angle ϕ_m and the polar angle deviates from the field precession angle $\theta_m < \theta_f$. This figure is adapted from Martin (2009) [53].

be written by plugging the velocity into Stokes drag force (Equation 7.2) and calculating the force difference:

$$F_H = 12\pi\eta a^2 \omega \sin\theta_f \, \hat{\phi} \tag{7.8}$$

By comparing the hydrodynamic force to the magnetostatic forces, $\mathrm{Mn} = F_H / f_c$, we can define the Mason number for a chain in a precession field:

$$\mathrm{Mn} = \frac{12^2 \eta \omega \sin\theta_f}{\mu_0 M^2} \tag{7.9}$$

For a purely rotational field, $\theta_f = 90^\circ$, the hydrodynamic force component used in determining the traditional Mn is recovered as previously used by Melle [52]. We can see in Equation 7.9 that $\sin\theta_f$ naturally decreases for lower

θ_f. In order to maintain a constant Mn without having to adjust the fluid viscosity or the magnetic field strength, the field frequency must increase to compensate for this change. Note that for the theoretical derivation of Mn we have chosen to use the angle of the precession field vector, θ_f, in Equations 7.8 and 7.9 rather than the angle of the chain vector, θ_m, to simplify the calculation. Martin goes into detail of the instability conditions that would lead to θ_m deviating from θ_f [53].

In Section 7.4.4 we carry out an analysis of the average cluster size, $S = (N - N_i)/N_c$, for our simulation study of the effect of Mn and θ_f on particle structure formation. Here N_i and N_c are the number of isolated particles and number of clusters, respectively. Terkel *et al.* previously studied additional simulation parameters for a system under shear [48].

7.3 Experimental

Conventional MR fluids were prepared by dispersing carbonyl iron particles (CIPs) in equal volume glycerol/water mixtures using a centrifugal mixer. CIPs used in this work were kindly provided by BASF SE Germany. In particular, we used an EW grade carbonyl iron powder (mean diameter ~3 μm) at 20 vol% concentration for rheometry tests and 1 vol% concentration for videomicroscopy tests. Glycerol (99%) was obtained from Sigma-Aldrich and used without further purification.

Rheological tests were carried out in a commercial magnetorheometer (MCR501, Anton Paar, SE Germany) with a homemade triaxial magnetic field generator designed to be mounted on top. The field generator consists of two pairs of coils in the x- and y-axis and a fifth coil situated beneath and oriented upward, which generates the field component in the vertical z-axis [more details can be found in Tajuelo (2023 under revision), Terkel (2022), and the supplementary material] [48, 54, 58]. A parallel plate configuration (z-axis in the velocity gradient direction) was used with a 20 mm diameter and 0.5 mm gap. We carefully micropipetted 150 μL of the MR fluid onto the center of the sample platform and immediately initiated the experimental protocol. In contrast to earlier work carried out by Terkel *et al.* [47-48] in these experiments the preshear interval has been eliminated, meaning upon loading the MR fluid sample and lowering the upper plate geometry to its measuring position the

magnetic field configuration protocol is immediately initiated. Even though a preshear interval is a logical step to remove the mechanical history of a sample, we found that this additional time prior to applying an external field affected the reproducibility of our results. In the absence of an external field CIPs ($\rho = 7.86$ g cm^{-3}) will begin to sediment with or without applied shear leading to a concentration gradient that can vary between experimental trials and thus in turn affect the magnetorheological response. By removing the preshear interval we limit this sedimentation period and found the rheometry results to be more self-consistent.

The rheometry tests were performed in two intervals. In the first interval, a three-step magnetic field configuration is applied to induce the self-assembly of particle structures. In each of the steps the external field strength has been programmed such that H_0 is constant, therefore we can directly compare the MR response as a result of structural changes rather than due to fluctuations in the field strength. The three steps were as follows: i) First, the MR fluid was allowed to structure under a uniaxial DC field applied in the vertical z-axis to form gap-spanning columnar structures, then ii) a precession field of determined Mn and θ_f is imposed on the system, and iii) finally, a uniaxial DC field is reapplied to reorient the evolved structures in the vertical direction. It was designed in a way such that we could directly compare the MR enhancement (in step iii) brought on by the application of a precession field (step ii) to a baseline reference, the traditional uniaxial DC response (step i). The structural and mechanical evolution of the system was studied throughout these three steps by applying a small-amplitude oscillatory shear (SAOS) test and measuring the storage modulus G' response. Each step had a duration of 120 s, which was deemed sufficient for reaching a steady-state or stabilized structure formation. In step ii the DC-component of the precession field is aligned in the vertical z-axis and the rotational field component is induced in the x, y-plane. Then, in the second interval a steady shear test was carried out still in the presence of the uniaxial DC field to measure the shear stress response. All tests were carried out at 25 ºC. For clarity, the field transitions between steps i and ii and steps ii and iii will be referred to as the DC-AC and AC-DC transitions, respectively, throughout the manuscript.

For the videomicroscopy experiments the three-step magnetic field configuration protocol was repeated for the 1 vol% concentration MR fluid samples. In these experiments, the sample platform of the triaxial device was swapped out for a hollow one. Additionally, an EFFILUX EFFI-BHS LED

Table 7.1 Field strengths H_0 and field frequencies f used to generate each precession angle θ_f for its corresponding Mason number Mn. The individual field strength components were programed to generate a consistent resultant field strength $H_0 = 5.54$ kA m^{-1} for all Mn and θ_f tested. The frequencies for Mn = 0.02, 2, and 20 have been calibrated for a 1:1 by volume water and glycerol mixture (η =8.4 mPa s), and for Mn = 2000 has been calibrated for a pure glycerol solution (η =1.41 Pa s). This change in the carrier fluid was necessary to reach the highest tested Mn without adjusting the field strength.

Precession angle, θ_f (deg)	$H_{0,z}$ (kA m^{-1})	$H_{0,x,y}$ (kA m^{-1})	Frequency, $f_{x,y}$ Mn = 0.02 (Hz)	Frequency, $f_{x,y}$ Mn = 2 (Hz)	Frequency, $f_{x,y}$ Mn = 20 (Hz)	Frequency, $f_{x,y}$ Mn = 2000 (Hz)
5	5.52	0.48	4.43	442.80	3542.43[a]	2630.89
10	5.46	0.96	2.22	222.25	2222.47	1320.47
15	5.35	1.43	1.49	149.11	1491.11	885.94
20	5.21	1.90	1.13	112.84	1128.38	670.42
30	4.80	2.77	0.77	77.19	771.86	458.59
45	3.92	3.92	0.55	54.58	545.79	324.27
60	2.77	4.80	0.45	44.56	445.63	264.77
75	1.43	5.35	0.40	39.95	399.54	237.39
90	0	5.54	0.39	38.59	385.93	229.30

[a]Due to a maximum 4 kHz frequency set by the triaxial hardware, this $\theta_f = 5°$ field configuration yields a Mn = 16.

backlight illuminator was carefully threaded into the triaxial situated above the z-coil and beneath the sample to enhance the image capturing. The MR fluid sample was loaded to a cylindrical sample chamber of 10 mm in diameter and 0.5 mm in height (same as the rheometry plate gap). The sample was enclosed by placing a glass cover slip on top. Step i of the field configuration protocol was immediately applied following the sample loading to avoid particle sedimentation. A Photron MiniUX high speed camera was used attached to a Leica Z6 APO stereomicroscope. In order to capture the DC-AC and AC-DC transitions we began image capturing during the last 10 s of each step and continuing 40 s into the following step. A final image was also taken at the end of steps ii and iii once the structures had completely stabilized.

Table 7.1 summarizes the precession magnetic field configurations studied in this work for the different Mn and θ_f tested.

7.4 Results and discussion

In studying the MR response throughout the three-step structuration period we can identify the G' dependence on Mn and θ_f. We know Mn to be a dimensionless number comparing the hydrodynamic forces acting on a magnetically responsive system to the magnetostatic forces driving the precession motion, which is dependent on the viscosity, frequency, and

magnetization through Equation 7.9. In each configuration the magnitude of the field strength is maintained constant at $H_0 = 5.54$ kA m^{-1} for all precession angles tested by adjusting the individual field components, $H_{0,z}$ and $H_{0,x,y}$ (see Table 7.1). The fluid medium is also consistent, meaning the viscosity of the MR fluid in the absence of an applied external field is the same for all experiments and is considered to behave like a Newtonian fluid. Therefore, the remaining variable, the angular frequency, $\omega = 2\pi f$ where f is the frequency of the rotating field components applied in the x, y-plane, is the sole parameter used to differentiate the experimental tests. In the first study, Mn was chosen to purposely span three distinct configuration regions. We have chosen to examine these cases where the magnetostatic forces dominate the hydrodynamic forces (Mn = 0.02), the hydrodynamic forces dominate the system (Mn =20), and a configuration in which these forces are considerably balanced around unity (Mn = 2). We have found that the MR enhancement strongly depends on the structuring mechanisms under each Mn as well as the structural evolutions that take place due to the DC-AC and AC-DC field transitions in the three-step structuration period of the experimental protocol. Later, an additional Mn = 2000 set of experiments were carried out. However, to increase the Mn two additional orders of magnitude we were met with limitations set by the triaxial magnetic field generator. Thus, these experiments were done employing pure glycerol as the suspending fluid ($\eta = 1.41$ Pa s) to reach higher Mn using lower, attainable field frequencies accessing the generator capacitor bank. We continue this analysis in a discussion on the G' response for each Mn case for θ_f spanning from 5º to 90º.

Analogous videomicroscopy experiments were carried out using lower 1 vol% concentration samples to visualize the structures formed under each Mn and θ_f. The various structure types are defined and identified in the following section. While the more concentrated MR fluids are necessary to carry out the rheometry experiments, they are unsuitable for bright-field optical microscopy tests. The dense particle structures impede light diffusion and obscure the sample. For this reason the lower concentration samples are utilized for image capturing experiments.

Although comparing the low concentration structure formations with the high concentration MR responses may seem unreasonable given the likely differences in the aggregation mechanisms at play for dilute and concentrated systems, our analysis shows compelling trends in the MR response that is only

reinforced by the videomicroscopy experiments especially when coupled with the analysis of the rheology data. These comparisons are later discussed in Section 7.4.2. Additionally, Terkel *et al.* carried out micro-CT experiments on a 20 vol% MR sample and showed similar analogous structures between the low and high concentrations MR fluids for a selection of structure types [47].

7.4.1 Structure types: videomicroscopy

In carrying out precession field videomicroscopy experiments on the 1 vol% MR fluid we identified the following structure types as represented in Figure 7.2:

(1) *Dynamic columnar structures*: For $\mathrm{Mn} \ll 1$ columnar chain-like structures move in line with the external field vector. The columnar structure characteristic is preserved during the AC-DC field transition. $\mathrm{Mn} = 0.02$, $\theta_f = 5^{\circ}$- 45°.

(2) *Segmented structures*: These structures similarly follow the external field vector. However, the abrupt AC-DC field transition for large θ_f leads to chain fragmentation as the hydrodynamic forces inhibit chain repositioning during the field transition. As a result, large chains fracture into smaller segments which then align with the external field. $\mathrm{Mn} = 0.02$, $\theta_f = 60$-75°.

Figure 7.2 Structure phase diagram following a) the DC-AC precession field application (end of step ii), and b) the AC-DC field transition (end of step iii) for each indicated Mason number Mn and precession angle θ_f. The structure types are mapped out and identified as follows: (1) *dynamic columnar structures* are formed for low Mn and θ_f where the magnetic forces dominate the hydrodynamic forces and the columnar structures can move in line with the external field, (2) *segmented structures* are a result of an abrupt field transition from a high angle precession field to uniaxial DC forcing the particle structure to fracture, or segment, due to the repulsive magnetostatic interactions and restructure in line with the external field, (3) *sedimented transition structures* similarly fracture and restructure with the field transition but are more prone to gravitational forces causing a particle concentration gradient, (4) *static collapsed columnar structures* are collapsed structures formed for high Mn and low θ_f where the polar angle θ_m = 0º as the phase lag between the chain and field vector increases to 90º, (5) *dynamic collapsed columnar structures* form for mid-range $\mathrm{Mn} \approx 1$, low θ_f field configurations and balanced forces, (6*) spiral structures* are shown to structure for a single tested field configuration where this unique formation appears out of a collapsed state when the precession field is applied, and lastly (7) *time-averaged to DC transition structures* form as a result of the field transitioning from a time-averaged magnetostatic interaction regime to a deterministic tip-to-tip dipolar interaction. Structure types 1, 4-6 are formed during the precession field application and conserved following the AC-DC field transition, whereas structure types 2-3, 7 form because of the AC-DC field transition.

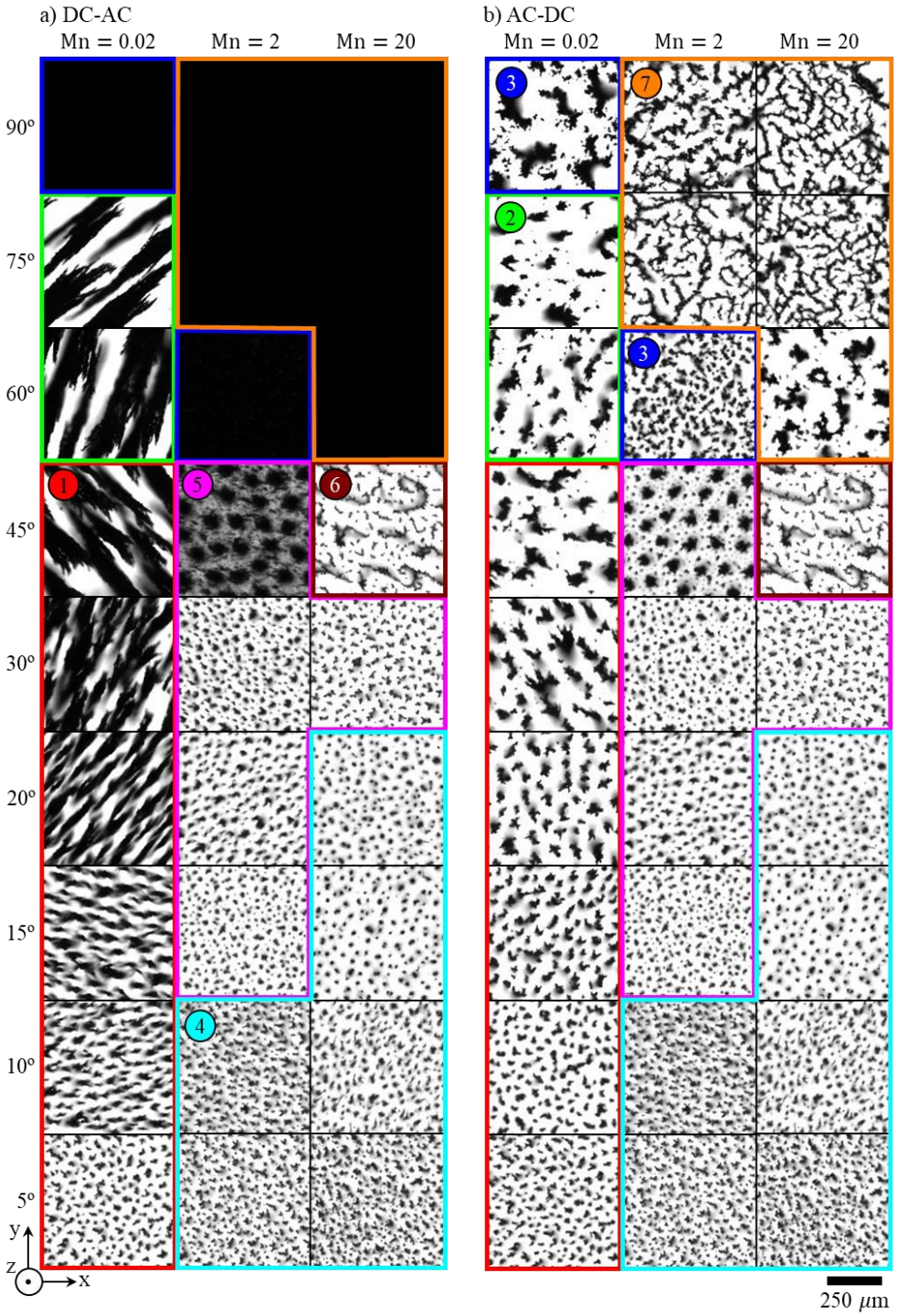
a) DC-AC
Mn = 0.02
Mn = 2
Mn = 20
b) AC-DC
Mn = 0.02
Mn = 2
Mn = 20
90º
75º
60º
45º
30º
20º
15º
10º
5º
y
z
x
1
2
3
4
5
6
7
3
250 μm

Figure 7.2

(3) *Sedimented transition structures*: These structures are unique in their aggregation dynamics. They seem to appear when the gravitational forces play a key role in the particle dispersion within a sample. Chain structures are susceptible to sedimentation for both low Mn rotational fields and mid-range Mn near the critical angle $\theta_f = 54.7^o$. In the latter case, small chains, often ideal for vortex mixing, lack gap-spanning connections to keep the structure erect in suspension. Moreover, for mid-range Mn the time-averaged repulsive magnetostatic interaction forces are not sufficiently strong enough to maintain defined elevated layers. In both cases a particle gradient arises due to gravity and a porous complex microstructure gives way to buckled or short columnar structures following the AC-DC field transition. Mn $= 0.02$, $\theta_f = 90^o$; Mn $= 2$, $\theta_f = 60^o$.

(4) *Static collapsed columnar structures*: For large Mn $\gg 1$ as the phase lag between the chain and field vector increases to 90º the polar angle of the chain vector θ_m decreases to 0º, meaning it collapses on the z-axis **[53]**. Often for low θ_f the structures are completely stationary with little to no structural evolution beyond the baseline structure formed under a traditional uniaxial DC field. Mn $= 2$, $\theta_f = 5^o$ - 10^o; Mn $= 20$, $\theta_f = 5^o$ - 20^o.

(5) *Dynamic collapsed columnar structures*: For mid-range Mn ≈ 1, low θ_f structures also appear to collapse on the vertical axis, however, they appear to still be dynamic in nature. In general, when the hydrodynamic and magnetostatic forces are more or less balanced, we witness interesting responses in the structures. In the Mn $= 2$ case, for example, for $15^o \leq \theta_f \leq 20^o$ collapsed structures are prone to translational movement and for $30^o \leq \theta_f \leq 45^o$ we witness increasingly disordered vertical columnar structures. Mn $= 2$, $\theta_f = 15^o$ - 45^o; Mn $= 20$, $\theta_f = 30^o$.

(6) *Spiral structures*: Perhaps the most unique discovered structure in the study is the spiral structure. These structures were only identified under one field configuration in the high Mn regime. Here the columnar structures are similarly collapsed, but the translational movement yields a complex spiral-like mesotructure. Mn $= 20$, $\theta_f = 45^o$.

(7) *Time-averaged to DC transition structures*: For large Mn and precession angles $\theta_f > 54.7^o$ the magnetostatic interaction between particles becomes repulsive, which drives the formation of layered

structures. Therefore, in the AC-DC field transition the layered structures immediately fracture and restructure with an anisotropic orientation in the direction of the external DC field. These final structures were found to vary in density depending on the precession field applied. Mn = 2, θ_f = 75º-90º; Mn = 20, θ_f = 60º-90º.

The structural evolution of a chain in a 2D rotational field ($\theta_f = 90°$) is simple, as shown in Figure 7.3. For low Mn $\ll 1$ the chain follows in line with the external field. Then, for increasing Mn, the hydrodynamic forces acting on a chain begin to deform the structure into an S-like shape. At a critical Mn ≈ 1 the chain will fracture lowering the hydrodynamic force on each half chain. For large Mn $\gg 1$ the structure loses its chain shape and ultimately devolves into a disk-like form of chaotically moving individual particles. Massana-Cid *et al*. (2021) have studied the cluster size of spinning ferromagnetic colloids dependence on field frequency and tracked the movement, or tangential velocity, of particles moving further out from the cluster center [55]. Recent experimental work using toggled fields to mimic thermal relaxation processes has led to more structural control over a 2D particle system (Camacho *et al.* (2023) in preparation) [56].

The impact of increasing Mn on a chain structure in the presence of a 3D precession field is more complex. A 3D precessing chain will similarly fracture under field configurations with Mn $\approx$ 1 for angles of precession near the critical angle $\theta_f = 54.7º$. This configuration is optimal for making small micro-mixer chains ideal for vortex mixing [33]. The disk-like form for 2D structures takes on the form of layered structures, given sufficient particle concentration, for high Mn $\gg$1 and $\theta_f > 54.7º$. In these configurations the repulsive time-average magnetostatic interactions encourage the aggregation of particles into layer formations.

In Figure 7.3 we also highlight a broad selection of particle structures types (*dynamic columnar structures, dynamic collapsed columnar structures, spiral structures,* and *static collapsed columnar structures*) formed under the same precession angle, θ_f = 45º, with increasing Mn distinguishing the type of aggregation structure. A video representation of these structure types in motion can be found in the supplementary material (Video S1) [58]. *Dynamic columnar structures* form for low Mn as the chain structure is able to follow in line with the field vector. Terkel *et al.* (2022) have made the argument that this

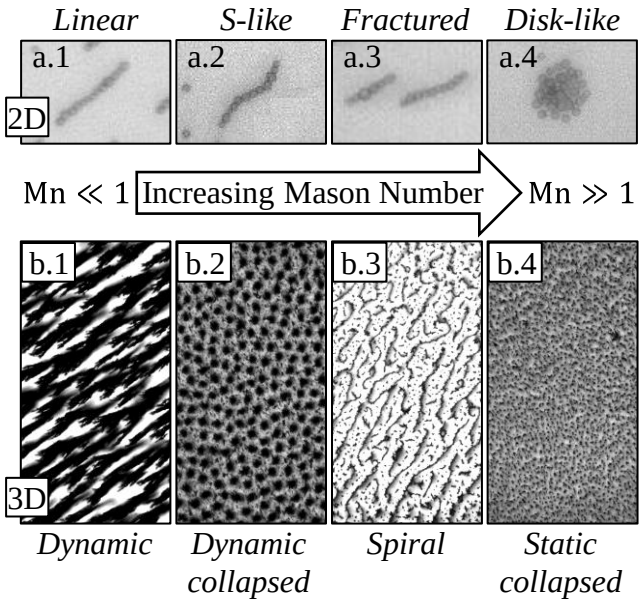

Figure 7.3 In a 2D system a chain of particles will rotate in line with a low Mn rotational field. As the Mn increases and the hydrodynamic drag acting on the chain increases, the chain will begin to deform into an S-like shape, fracture, and form disk structures for Mn ≫ 1. For low θ_f in a 3D system as Mn increases, the phase lag between the chain and field vectors increases to 90º, and the polar angle of the chain will collapse on the axis of the DC field component of the precession field, in this case directed coming out of the plane of the paper. Here we show the structure collapse for $\theta_f = 45º$ with increasing Mn. Video S1 in the supplementary material shows panels b.1 through b.4 in motion [58].

field configuration promotes chain thickening via lateral chain coalescence [48]. Typically low field frequencies are employed to generate these structures, as a result we do not witness a strong vortex mixing response in the videomicroscopy experiments despite the dynamic nature at play. For mid-range Mn ≈ 1, the hydrodynamic forces cause a lag between the field and chain vector leading to the columnar chain structures collapsing on the axis of the DC component of the precession field. These *dynamic collapsed columnar structures* are loosely packed and highly disordered and under visual inspection still show movement with an axial rotation around the lateral chain axis. *Spiral* structures form as the Mn continues to increase and for large Mn ≫1 we form *static collapsed columnar structures*, where the hydrodynamic forces completely dominate the system and inhibit structure transformation. These structures show no signs of movement and maintain the same structural characteristics of an MR fluid structured under a traditional DC

uniaxial field. To understand the dynamic and static nature of these structure types we must consider particle magnetic relaxation.

The Brownian type remagnetization mechanism is defined by a particles' ability to rotate and align with the external field with a fixed internal magnetization with respect to the multi-domain crystalline lattice. Particle rotation, however, does not happen under the Néel relaxation mechanism. In this case the internal magnetization rotates independent of the crystalline lattice. For collapsed structures the Mn, controlled through the frequency of the rotational field component of the precession fields, will dictate the relaxation type. We expect for the *dynamic collapsed columnar struc*tures the Brownian relaxation time is faster, which would allow the axial rotation. It should be noted that the frequency of the axial rotation was observed to be less than the programmed field frequency. On the contrary the Néel relaxation time must be faster for the *static collapsed columnar structures*, where the internal magnetization changes direction without causing structural movement. Working with micron-sized CIPs, it is expected that both the Brownian (τ_{B}) and Néel (τ_{N}) relaxation times contribute to varying degrees of uniformity throughout a multi-domain lattice, with the net-fastest response dominating through $\tau_{\mathrm{eff}} = \tau_{\mathrm{B}}\tau_{\mathrm{N}}/(\tau_{\mathrm{B}} + \tau_{\mathrm{N}})$ [57].

7.4.2 Rheometry

7.4.2.1 Storage modulus

In the low $\mathrm{Mn} = 0.02$ case it is expected that a chain of particles will move in line with the external field, meaning there is no phase lag between the chain and field vector. This is due to the magnetostatic forces playing a more important role in the particle aggregation dynamics than the hydrodynamic forces. Chain or aggregate fracturing due to the velocity of the precession motion itself is minimized under this configuration regime for all precession angles; however, large angle field transitions are still prone to fracture the structures. In Figure 7.4a we plot the storage modulus G' versus time t during the three-step structuration period for the $\mathrm{Mn} = 0.02$ case. The response in the first interval when the initial DC field is applied is similar as indicated by the overlapping curves, which is expected as the first step is identical in each test. In the presence of the initial DC field the particles are driven to form anisotropic gap spanning structures. Following the second step when the

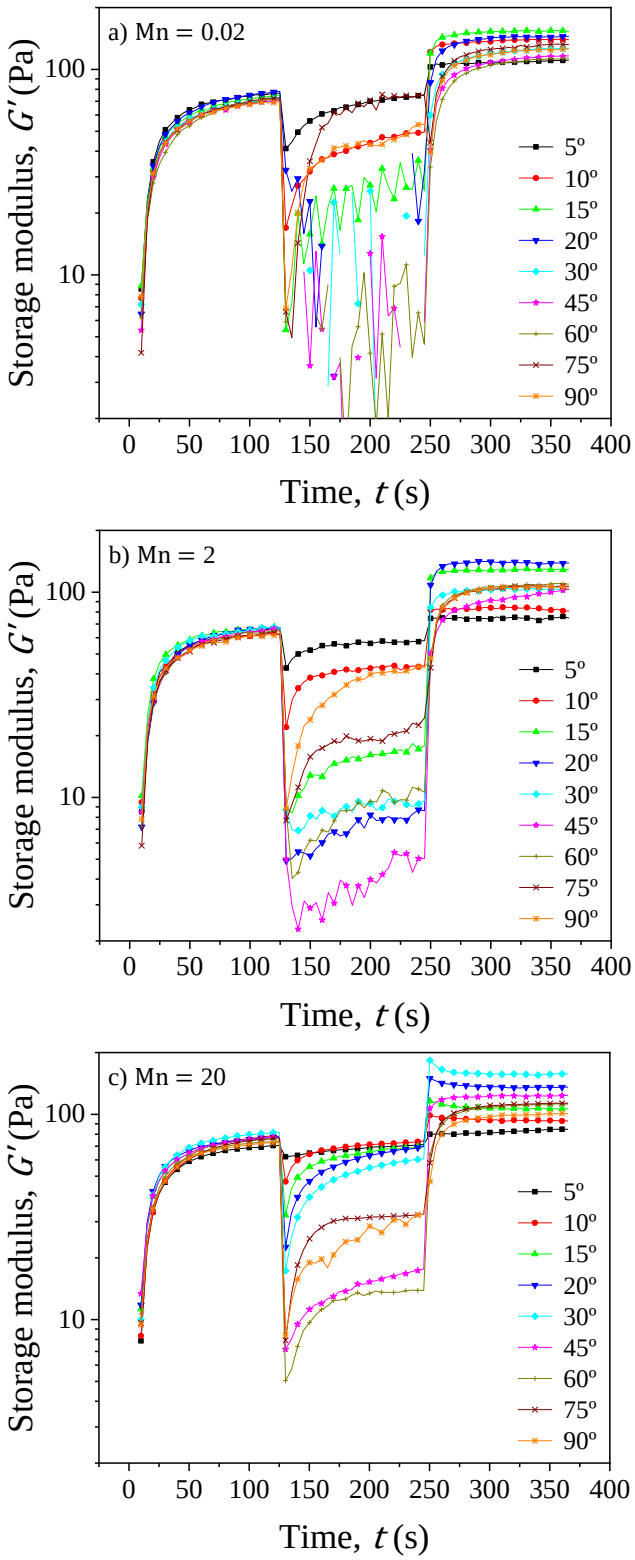
a) Mn = 0.02
b) Mn = 2
c) Mn = 20
Storage modulus, G' (Pa)
Time, t (s)
100
10
0
50
100
150
200
250
300
350
400
5º
10º
15º
20º
30º
45º
60º
75º
90º

Figure 7.4

distinct precession field at its programmed Mn and θ_f is applied, a subsequent DC field step is applied to reorient the structures in the direction perpendicular to the rheometry plates, the z-axis, to best quantify the MR enhancement. Theoretically, the MR fluid for the more optimal field configurations is strengthened by the end of the middle AC step. However, the G' results do not necessarily reflect this showing values equal or below the plateau value of the first step. Primarily this is due to the unfixed dynamic nature of the precession motion, but also because for larger precession angles the DC field component of the precession field aligned in the z-axis is lower (see Table 7.1). For this reason, the clear MR response is not fully realized until the final DC field is reapplied and the strengthened structure within the MR fluid reorients. It appears for the low Mn experiments, a precession field applied at $\theta_f = 15°$ has the largest response as indicated by the highest reported values in the third step. Apart from comparing the final storage modulus value, G'_f, to the initial curve plateau value, G'_i, which is later discussed in more detail in the summary Figure 7.5, we can also take a closer look at the curve trends to more thoroughly understand the aggregation mechanisms taking place throughout the entire structuration evolution and more importantly during the AC-DC field transition.

We begin this closer analysis of the curve trends for the Mn = 2 results in Figure 7.4b as the trends are more clearly defined in this Mn configuration. According to the videomicroscopy experiments we know that the low θ_f and high θ_f field configurations yield *static collapsed columnar structures* and *time-averaged to DC transition structures*, respectively. In the former case, there is no structural evolution following the AC-DC transition. The collapsed structure remains vertically oriented and the G' curve abruptly increases and reaches its final plateau value within one data point acquisition, as clearly seen for $\theta_f = 5°$-$15°$. On the contrary for the latter case following the AC-DC transition the final *time-averaged to DC transition structures* have completely fractured and reformed and do not retain any structural identity of the layered structures formed during the precession field application. This restructuration

Figure 7.4 Analysis of the time, t, dependence of the storage modulus, G', during the three-step structuration process for a) Mn = 0.02, b) Mn = 2, and c) Mn = 20 field configurations. Overlapping curves in the first step indicates good reproducibility in sample formulation and loading. Higher G' response in the third interval gives evidence that certain triaxial precession field configurations enhance the MR response beyond the limited response set by traditional uniaxial fields.

is proved by the gradual G' increase over 50 second to reach the plateau value in the final interval for the $\theta_f = 75^o$-90^o configurations.

In Figure 7.4c we see similar abrupt and gradual G' transitions for the $\mathrm{Mn} = 20$ case, employing the fastest field frequencies. These two trends reinforce the case that the higher concentration MR fluids used in the rheometry experiments respond in their more dense state to field transitions similarly as the lower concentration MR fluid used for microscopy tests.

7.4.2.2 MR effect

In Figure 7.5 we summarize the storage modulus enhancement, $\left(G'_f - G'_i\right)/G'_i$, by comparing the final G'_f to the initial baseline G'_i responses for each of the initial three Mn tested as well as the higher $\mathrm{Mn} = 2000$ case carried out with the modified more viscous sample. First we will discuss the low $\mathrm{Mn} = 0.02$ (light gray) and high $\mathrm{Mn} = 20$ (dark gray) cases, then followed by a discussion of the mid-range $\mathrm{Mn} = 2$ (gray) case. As previously mentioned, our analysis of the videomicroscopy tests supplements our understanding of the results shown here.

For the $\mathrm{Mn} = 0.02$ case the G' response increases with the precession angle and peaks at $\theta_f = 15^o$ then consistently decreases until $\theta_f = 60^o$. In this low Mn regime the magnetostatic forces dominate the hydrodynamic forces and for low concentration MR fluids the structures are expected to move in line with the external field vector. Moreover, for angles of precession $\theta_f \leq 45^o$ there is no loss in structural identity according to visual inspection of the videomicroscopy experiments during the DC-AC or AC-DC field transitions as the transition angular rotation is small. As previously reported by Terkel (2022), this low Mn and low precession angle configurations are optimal for structural strengthening through chain coalescence, as they reported a maximum particle average cluster size for a simulated low Mn, $\theta_f = 15^o$ precession field [48]. During the application of the precession field, neighboring chain structures are susceptible to lateral coalescence. Two identical neighboring chains in parallel will experience a repulsive interaction due to the repulsive nature of side-by-side magnetic dipole moments of each respective chain particle aligned in the same direction [4]. This is known as chains being in-registry. Under a uniaxial DC field a homogenously dispersed

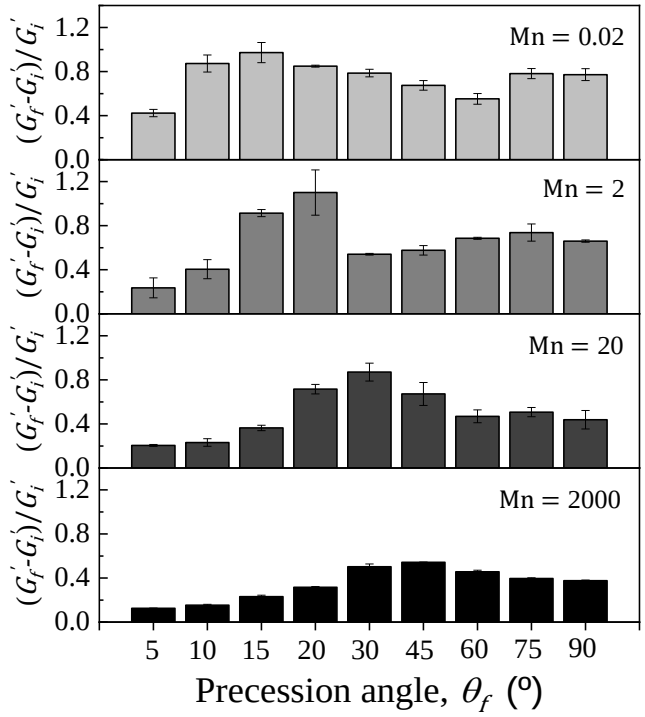

Figure 7.5 Summary plot of the storage modulus enhancement $(G'_f - G'_i)/G'_i$. We identify a peak response at $\theta_f = 15º$ for the low Mn $= 0.02$ case and the overall greatest response at $\theta_f = 20º$ for the Mn $= 2$ case. We expect lateral chain coalescence and particle compactness as the key factors in reinforcing the aggregate structures. In general, the peak response occurs at larger precession angles with increasing Mn. This is because the structures are more prone to collapse in the direction of the DC field component of the precession field for low θ_f, essentially becoming completely static with no structural evolution for large Mn $\gg 1$. Only as θ_f approaches the critical angle do we witness structural movement for large Mn values.

system of single particle width chains or columnar structures, depending on the particle concentration, is stabilized for a closed system. The most indisputable benefit of working with triaxial fields is overcoming the limitations set by traditional DC fields. When a precession field is applied two neighboring chains can coalesce through direct collision, which is more likely for densely populated systems, and also through minor displacements in the spatial orientation of the chains. In these low Mn configurations, chains rotate in the x, z plane (for example) to align with the external field at the programmed precession angle. This realignment of the polar angle also induces a lateral displacement between neighboring chains. A simple lateral

displacement of a, i.e. a particle radius length, can move neighboring chains from an in-registry positioning to and out-of-registry positioning, which for low separation distances is attractive and thus leads to lateral chain coarsening. Thicker structures are more robust to deformation and therefore have a larger MR enhancement. It is therefore expected that the Mn $= 0.02$, $\theta_f = 15^o$ configuration is optimal for promoting lateral connections throughout the particle structure.

For larger precession angles there is a clear break in the G' response trend between $\theta_f = 60^o$ and $\theta_f = 75^o$. The previous discussion on the *segmented structure* type in Section 7.4.1 can help explain the response, which shows the G' enhancement having increased for $\theta_f \geq 75^o$. For larger precession angles, chained structures rotate and the polar angle deviates further from the axis of the DC component of the precession field. As a result, connections between the top and bottom plate of the rheometer setup are likely to disconnect leaving the structures free to sediment at the will of gravitational forces. Note that CIPs are much denser ($\rho = 7.87$ g cm^{-3}) than the fluid medium in which they were dispersed ($\rho = 1.14$ g cm^{-3}). The t =120 s interval that the precession field interval is applied is sufficient for particle sedimentation creating a gradient in the particle concentration with more densely packed structures near the bottom plate and a particle poor region near the top plate. This was clearly witnessed in the videomicroscopy experiments and rationally makes sense for the higher concentration rheometry tests as well. During the AC-DC field transition the abrupt large angular rotation would also cause structural segmentation or structural realignment that would not necessarily result in the major axis of the anisotropic elongation being aligned with the external field. The combination between the particle concentration gradient and the segmenting structures is responsible for this break in the G' response trend, with storage modulus values falling below the peak precession angles response but above the response for precession angles just below the critical angle.

Continuing with the Mn $= 20$ experiments, across all precession angles the response is low. For precession angles less than the critical angle of $\theta_f < 54.7^o$, we witnessed *static collapsed columnar structures* in the videomicroscopy experiments. Similarly expected in the high concentration rheometry tests, for high Mn the polar angle of the precessing structures collapses on the vertical axis as the phase lag between the structure and field vector increases to $\phi_m = 90^o$ (see Figure 7.1). The high field frequencies applied in the rotational field

components in the x, y-plane are far too fast for the structures to respond to given the hydrodynamic forces eclipsing the magnetostatic forces in the higher Mn configurations. Additionally, we expect an inner remagnetization of the Néel type inhibits structural movement. As a result, the structures mostly remain stationary (apart from the $\theta_f = 45^{\circ}$ *spiral structures*) showing little evolution beyond the DC field-driven columnar structures. Thus, the G' response likewise shows little improvement beyond the baseline uniaxial DC case.

On the other hand, for Mn $= 20$ experiments and precession angles greater than the critical angle of $\theta_f > 54.7^{\circ}$ the MR response is also low, although for a completely different cause. During the application of these high Mn precession fields, time-averaged repulsive forces drive the formation of layered structures. Visualization of the layers in our traditional setup is difficult as the layered structures perpendicular to the axis of the camera setup appear completely opaque as seen in the upper right quadrant of Figure 7.2a. In Figure 7.6 we show these layered structures by changing the field orientation such that the DC component was applied in the y-axis and the rotational field component was applied in the x, z-plane. Expectantly, layers (here identified as black lines) were formed in the x, z-plane. From this perspective the light passes through the voided space between the layers and can easily be image captured for low particle concentrations. The conservation of these layers is inevitably impossible following the AC-DC field transition. The transition from the time-averaged repulsive forces aggregation mechanism (high Mn, $\theta_f > 54.7^{\circ}$) to a typical tip-to-tip deterministic aggregation mechanism (uniaxial DC) results in the spontaneous fracturing of the horizontal layers and restructuring into vertically oriented aggregates. The low G' response for these configurations suggests that the restructured aggregations pale in comparison in strengthening the MR fluid to some of the other tested configurations.

As a brief aside, the Mn $= 2000$ G' results shown in Figure 7.5 share the same trend as the Mn $=20$ case, but more exaggerated. The MR response peak continues its trend of moving to higher precession angles closer to the critical angle and the response for lower precession angles continues to decrease. Indeed, one would expect that for very high Mn $\gg 1$ and θ_f less than the critical angle, the MR response would be indistinguishable from the uniaxial DC field response.

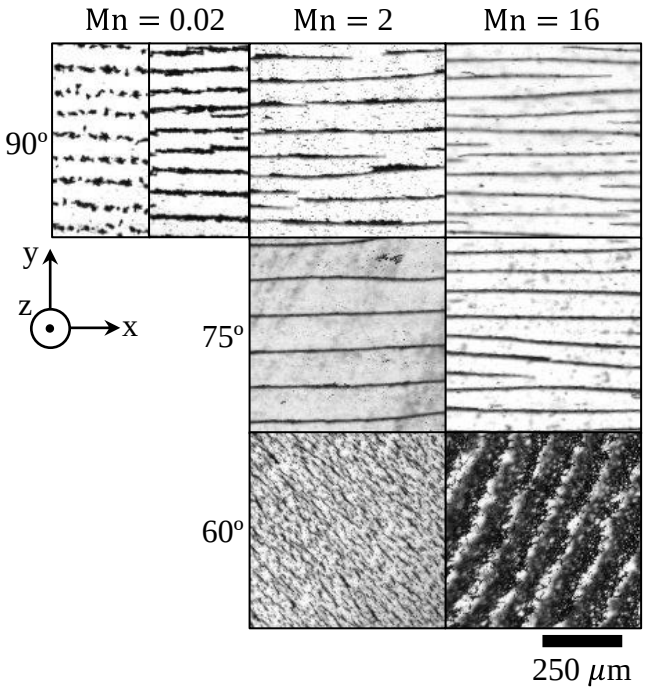

Figure 7.6 By reorienting the precession field such that the rotational field component is in the x,z-plane, $\vec{H} = H_0\{\sin\theta_f\,[\sin(\omega t)\hat{x} + \cos(\omega t)\hat{z}] + \cos\theta_f\hat{y}\}$ we can visualize the layered structures that otherwise would be visually obstructed due to poor light penetration in the normal microscopy setup (see upper right hand quadrant of Figure 7.2a). Here we clearly see which configurations result in well define layered structures, which appear as solid black lines for this field orientation. For the purely rotational field ($\theta_f = 90º$) Mn = 0.02 case we show the structure at two time frames. On the left the chainlike structures are oriented coming out of the plane of the page and on the right are oriented along the x-axis and should not be mistaken as layered structures. The $\theta_f = 60º$, Mn = 2 configuration yields a suspension of small chain length micromixers, and the $\theta_f = 60º$, Mn = 16* configuration yields a disordered layered structure where the surface normal of the layers does not align in the direction of the DC field component of the precession field. **Due to a limitation set by the triaxial magnetic field generator, we were unable to reach high enough field frequencies to reach the* Mn = *20 configurations, therefore the maximum we show is for* Mn = *16 without having to adjust any other variables in the Mn calculation (Equation 7.9).*

In general we have found that the MR response is lower for the field configurations in which particle structures are unable to preserve columnar characteristics throughout the complete three step field protocol. The *time-averaged to DC transition structures* and the *segmented structures* both suffer from severe restructuration brought on by the field transitions. A method for preventing the formation of *segmented* and *sedimented transition structures* is explored in Section 7.4.3.

We continue the analysis of Figure 7.5 with a discussion on the Mn = 2 results. For mid-range Mn, where the hydrodynamic and magnetostatic forces are relatively balanced, the results are interesting. In fact, the largest measured G' response of all configurations tested was documented for the $\theta_f = 20^o$ case. Again we correlate these results with the videomicroscopy experiments to more clearly interpret the structural responses under this Mn regime. For low precession angles $\theta_f < 15^o$ we formed *static collapsed columnar structures* akin to the Mn = 20 configurations of the same precession angles. Between $\theta_f = 10^o$ and $\theta_f = 15^o$ there is a stark increase in the G' response. Therefore, we can expect a different structural mechanism is at play. For $\theta_f = 15^o$-45^o we formed *dynamic collapsed columnar structures* with the structures for $\theta_f = 15^o$ and $\theta_f = 20^o$ being more ordered than the $\theta_f = 30^o$ and $\theta_f = 45^o$ configurations.

We identified two types of movements, the columnar chains themselves rotate around their lateral axis and a more collective movement in which the structures rotate around the center of the sample chamber. The latter translational movement led to some lateral coalescence in the more ordered $\theta_f = 15^o$-20^o configurations; although, an aerial view of the columnar structures shows thinner chain diameters than the chains formed in the peak Mn = 0.02 field configuration at $\theta_f = 15^o$, and yet the MR enhancement is superior for $\theta_f = 20^o$ in the mid-range Mn = 2 regime. Our original theory that thicker chains equate to a more robust response to deformation may be true for the low Mn regime where the structural evolution is defined by precession field induced lateral connections. However, we posit a different aggregation mechanism is responsible for the strong response unique to these configurations where the hydrodynamic and magnetostatic forces border on being in equilibrium.

For these $\theta_f = 15^o$-20^o angles of precession in the Mn = 2 case the hydrodynamic forces acting on the columnar chains are strong enough to collapse the structures. As previously discussed in Section 7.4.1, the likely Brownian relaxation of the inner magnetization of the particles would allow this continued axial rotation, differentiating them from the *static collapsed columnar structures*. We suspect that the translational movement of the structures is a result of friction brought on by the axial rotation between the chain extremities and the top and bottom boundaries of the sample chamber. Despite the apparent thinner columnar structures, we believe particle

compactness within the structure is a key factor for the greater MR response under these precession field configurations. Using traditional bright-field microscopy we can only visualize the axial rotation around the lateral collapsed columnar structures. However, it is possible that the individual particles themselves, both in the low concentration videomicroscopy and high concentration rheometry experiments, similarly rotate as a response of Brownian relaxation. This particle movement unique to these field configurations could promote localized agitations allowing the particles to find a more tightly packed metastable lower energy state. This lower energy state would then be trapped and stabilized following the AC-DC transition and thus yielding a more robust structure.

7.4.3 Field transitions

Figure 7.7 summarizes the structure phase diagram following the precession field application as composed from the videomicroscopy images displayed in Figure 7.2a. Here we can easily identify the field configurations in which chain aggregation and layered structures are formed. Four generalized quadrants (in gray) are relatively defined by Mn = 1 and the precession angles $\theta_f = 45^o$ and $\theta_f = 54.7^o$ separating quadrants I/II and III/IV, respectively. In discussing the MR response up until now we have pointed out the importance of maintaining structural integrity throughout the three-step field structuration process. In Figure 7.8 we highlight the rheological response of one field configuration representing each of the seven structure types discussed in this work and compare their improvement over the baseline uniaxial DC field configuration. The field configurations that drive the *dynamic columnar structure* and *dynamic collapsed columnar structure* types consistently perform the best with the greatest G' increase in Figure 7.8a and yield stress increase in Figure 7.8b as indicated by the largest measured stress in the low stress plateau of the rheogram. On the other hand the *time-averaged to DC transition structure* type, where no structural identity is conserved shows less rheological enhancement over the uniaxial field case.

In quadrant I chains are expected to follow the external field, and for precession angles $\theta_f \leq 45^o$ the transition angular rotation is small enough that chains can make that rotation without fracturing. In quadrant III, collapsed chains already aligned on the axis of the DC-field component of the precession field, will remain aligned in this axis when the field transitions to DC uniaxial. However,

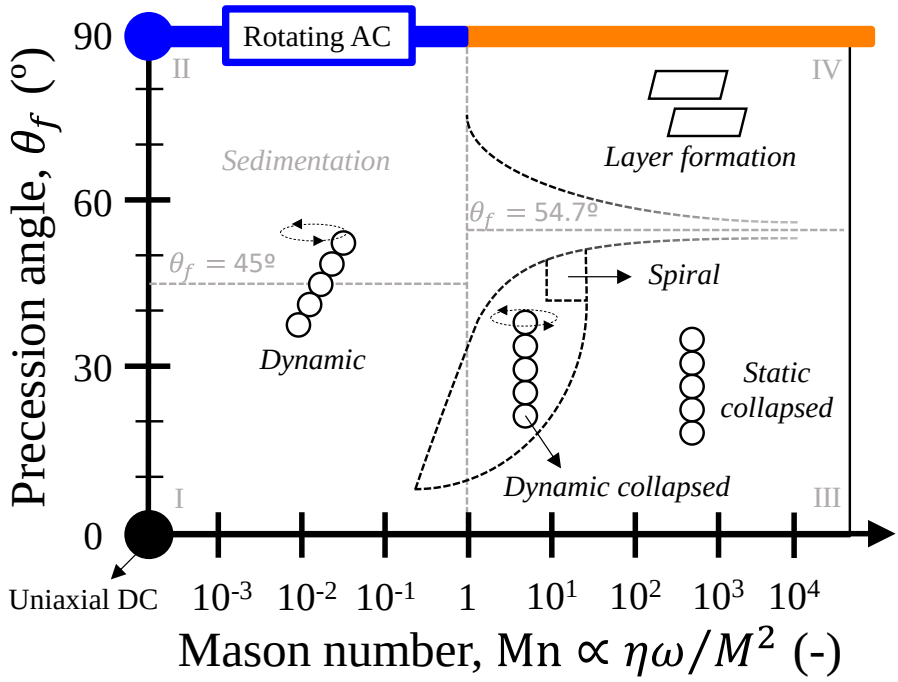

Figure 7.7 Structure phase diagram following the precession field application. We indicate in light grey four generalized quadrants as well as the structure types found in each of them.

for certain field configurations and precession angles the abrupt AC-DC field transition can lead to aggregate fracture and restructuration. This is inevitable for the layered structures formed in quadrant IV. The transition between a field configuration which drives time-averaged repulsive magnetostatic interactions between particles to one driven by dipolar interactions will surely cause a drastic structural turnover.

This leaves quadrant II to be discussed in further detail. Quadrant II is defined by precession field configurations with low Mn and high θ_f. In Figure 7.2a these configurations are well represented by the structures formed in the Mn $=$ 0.02, $\theta_f =$ 60-75º and $\theta_f =$ 90º cases, and the resultant *segmented* and *sedimented transition structures* shown in Figure 7.2b following the AC-DC field transition. The reason for the structure fracturing is twofold. First, lets consider two adjacent particles in a chain moving in line with an external precession field at $\theta_f = 75º$. Here the Mn can be considered Mn $\ll 1$, with no phase lag between the field and chain vector, and the angle between the field vector and the line of centers between particles $\theta = 0º$, thus indicating their dipolar attractive magnetostatic interaction. Upon abruptly transitioning the

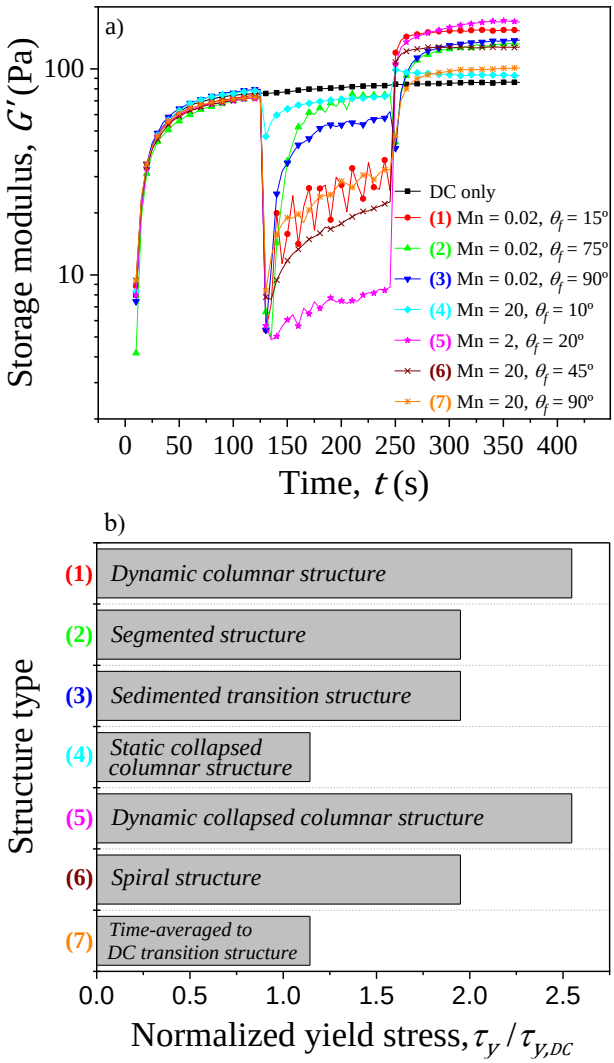

Figure 7.8 Comparison of the a) storage modulus G' and b) normalized yield stress enhancement $\tau_y/\tau_{y,DC}$ for the specified field configuration examples that drive the formation of each structure type. The (1) *dynamic columnar structure* and (5) *dynamic collapsed columnar structure* have the highest improvement over the uniaxial DC only case. Meanwhile the (4) *static collapsed columnar structure* and (7) *time-averaged to DC transition structure* have the poorest response. Color code is the same as in Figure 7.2 and $\tau_{y,DC} = 0.62$ Pa.

external field to uniaxial DC would result in the individual magnetic moments of the two particles similarly emulating the field change. Now, the angle between the external field and the line of centers between the particles immediately jumps to $\theta = 75^{o}$ and changing the spatial positioning of the particles into a repulsive magnetostatic interaction, which would facilitate structure segmentation. Secondly, one may consider that a particle's slight magnetic remanence would support chain realignment with the external field rather than individual particle realignment. In this case, hydrodynamic forces would be the leading factor in chain segmentation.

In order to determine whether the magnetostatic or hydrodynamic forces would prevail in this specific field transition we can substitute $\omega = \Delta\theta/\Delta t$ as the newly defined stepped transition rate into Equation 7.9 for the Mn for purely rotational fields, $\theta_f = 90°$, where $\Delta\theta = \theta_f/n$ we define as the stepped transition angle that is equal to the precession angle divided by some integer, n, and Δt is some characteristic response time for a chains ability to realign from a precession field to a uniaxial field, which we consider to be on the order of a couple of milliseconds for our system. This interpretation of the Mn allows us to weigh the magnetostatic and hydrodynamic forces acting on a chain during the AC-DC field transition, or any field transition for that matter. In a similar manner as before, for $\mathrm{Mn} < 1$ the magnetostatic forces are strong enough to rotate a chain without breaking in the field transition, and for $\mathrm{Mn} > 1$ chain segmentation is expected as the hydrodynamic forces will dominate.

Up until now we have only considered abrupt field transitions in our experimental work meaning $n = 1$ and $\Delta\theta = \theta_f$. The field configurations defined by quadrant II of Figure 7.7 were of interest to incorporate the concept of stepped transition angles, given they are the only configurations whose final MR response could realistically benefit. A slow enough stepped transition rate would increase the likelihood of maintaining structural integrity through the AC-DC field transition by incrementally transitioning the polar angle of the precession angle from $\theta = \theta_f$ to $\theta = 0°$ in n intermediate steps. In Figure 7.9 we plot the Mn as a function of the stepped transition angle. The Mn expectantly increases with $\Delta\theta$ and crosses unity at around $\Delta\theta = 20°$. In theory, stepped transition angles less than this critical value (for our studied CIP and glycerol/water system) should be more likely to retain structural integrity and avoid segmentation.

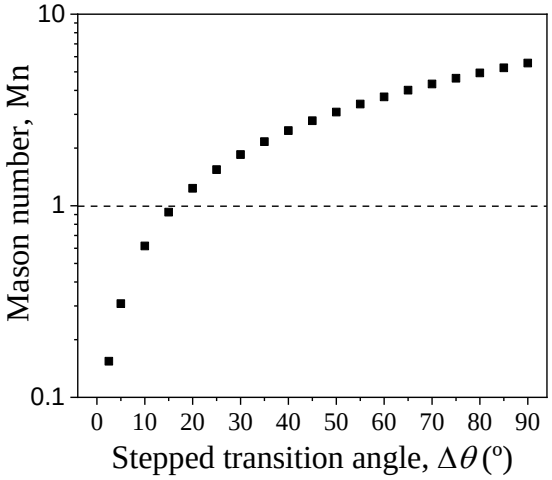

Figure 7.9 Estimation of the Mn for the magnetostatic and hydrodynamic forces acting on a chain, in our CIPs and water/glycerol system, during the field transition between two configurations directed in different directions. Rather than abruptly transition between field configurations, these results suggest that a meticulously controlled field transition with stepped angle transitions of $\Delta\theta \leq 20^{\circ}$ could potentially reduce the likelihood of chain fracturing, or segmentation.

We repeated the rheometry experiments for a selection of $\Delta\theta \leq 20°$ for the Mn = 0.02, $\theta_f = 75^{\circ}$ and $\theta_f = 90^{\circ}$ configurations. The storage modulus analysis of these experiments is displayed in Figure 7.10. For both the $\theta_f = 75^{\circ}$ and $\theta_f = 90^{\circ}$ configurations the response hovers around the initial MR response of the abrupt case. There is no indication that our effort to conserve the particle aggregations during the field transition yielded a more robust structure. Despite these findings, we are reminded of another contributing factor acting on the particle structures in this configuration quadrant – gravity. The effect of gravitational forces is minimized for structures formed in quadrant I and III and it is expected that the repulsive forces between particle layers formed in quadrant IV counteract the downward pull of gravity. However, as a chain transitions from quadrant I to quadrant II, at precession angles $\theta_f > 45^{\circ}$ the field amplitude in the x, y-plane becomes greater than the DC field component in the z-axis. As a result, the structures are especially prone to disconnect from the upper plate and sediment due to gravity leading to a gradient in particle concentration. While introducing stepped transition angles into the experimental protocol may promote chain or columnar-like structure conservation through a field transition, this stepped method cannot evade gravity. Video S2 in the supplementary material directly compares the

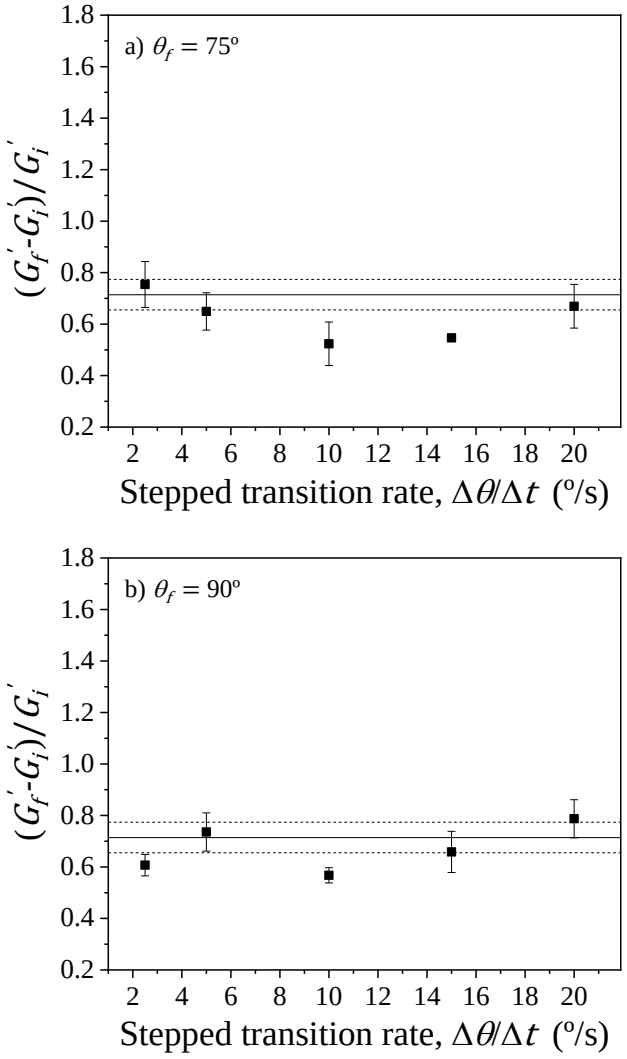

Figure 7.10 The storage modulus G' response for stepped transition angle experiments for both (a) $\theta_f = 75°$, Mn = 0.02 and (b) $\theta_f = 90°$, Mn = 0.02 configurations do not show any enhancement over the abrupt transition case (solid horizontal line, dotted line is the error range). The results at each of the stepped transition rates tested fall around or below the abrupt transition results. Despite our attempt to conserve the structural integrity of the particle aggregates in these DC-AC and AC-DC stepped field transitions, it was determined that particle sedimentation due to gravity is inescapable for precession fields in the Mn $\ll 1$ regime with precession angles $\theta_f > 45°$, thus cancelling out any structural gain from the stepped transition.

segmented structure formation for an Mn = 0.02, $\theta_f = 75^o$ to uniaxial DC abrupt transition to the columnar-like structure conservation for a stepped field transition ($\Delta\theta/\Delta t = 2.5$ °/s) of the same configuration [58]. Additionally, for these low Mn precession field configurations, there are no repulsive particle interactions keeping the particles elevated in suspension. Therefore, regardless of an abrupt or stepped field transition, a particle gradient arising from gravity ultimately levels the MR response.

7.4.4 Simulations

Particle-level simulations were carried out for a similar range of Mn spanning from Mn = 0.005 (magnetostatic dominated system) to Mn = 50 (hydrodynamic dominated system) to study the structural response. In Figure 7.11 we show the average cluster size, S, for a MR fluid following the application of the precession field (end of step ii) and following the AC-DC transition (end of step iii). These simulations support our videomicroscopy and rheometry results, and were programmed with abrupt field transitions.

Particular attention is paid to this specific simulation parameter given that larger cluster sizes, especially for low angles of precession, corresponds to structural strengthening via increased lateral connections as seen in *dynamic columnar structures.* Moreover, drastic changes in the average cluster size between the end of step ii and the end of step iii is a clear indication of a loss of structural identity due to field transitions, as seen in *segmented structures* and *time-average to DC transition structures.* By comparing a selection of these simulated field configurations to our experimental work, we can better appreciate the interactions between particles and chain-like structures that drives structural reinforcement or fracturing.

In Figures 7.11a and 7.11b the average cluster size peaks at $\theta_f = 10^o$ for these lower Mn *dynamic columnar structures* where lateral coalescence of neighboring chains promotes chain thickening [48]. In Figures 7.11c and 7.11d we see the average cluster size is constant for low $\theta_f = 5^o$ - 20^o, which is expected as the structures collapse for higher Mn and have less interaction with nearby chains and thus less lateral connectivity. Of course for the highest tested Mn for these low θ_f we expect *static collapsed columnar structures* with no structural evolution beyond their initial alignment under a uniaxial DC field.

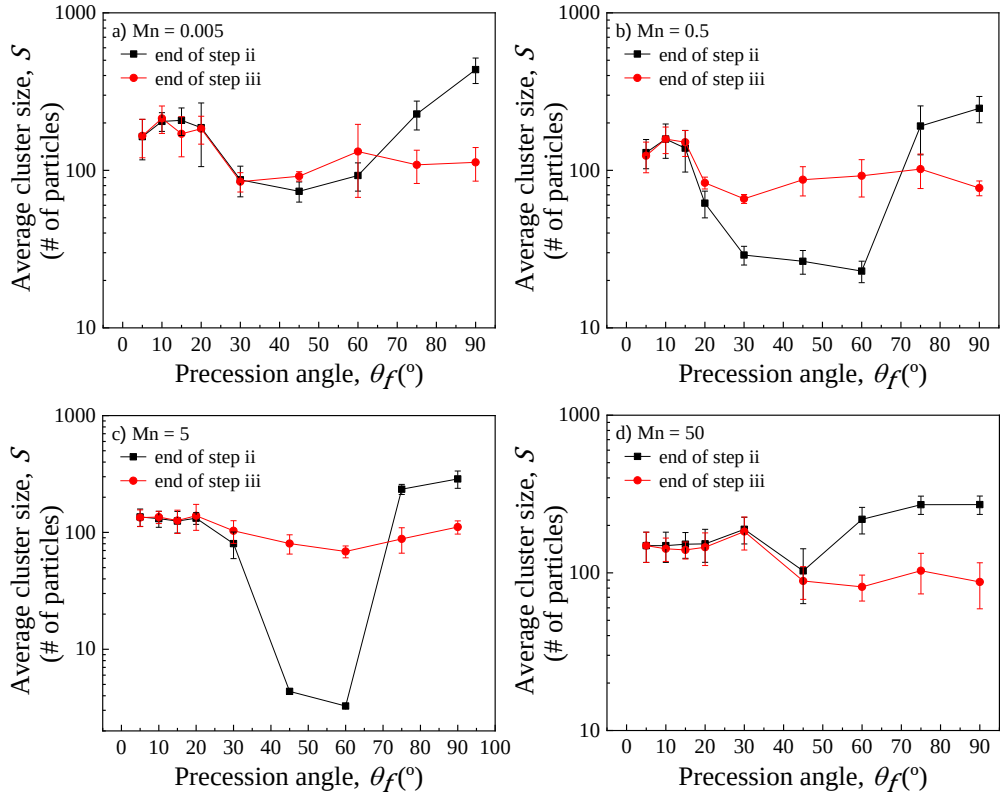

Figure 7.11 Particle-level simulations of the average cluster size, S. Here we show the average cluster sizes for the system following the precession field application (black, end of step ii) and following the AC-DC field transition (red, end of step iii) for a) Mn = 0.005, b) Mn = 0.5, c) Mn = 5, and d) Mn = 50 cases. Considering the precession angles below the critical angle, the average cluster size peak increases at higher precession angles for higher Mn configurations similarly to Figure 7.5.

We provide in the supplementary material a look at a simulated *dynamic columnar structure* (Video S3) and *dynamic collapsed columnar structure* (Video S4) [58]. For both simulations the angle of precession is set to $\theta_f = 20^{\circ}$ with the Mn = 0.1 for the former and Mn = 5 for the latter. In the Mn = 0.1 case the magnetic forces still dominate the hydrodynamic forces and the chains clearly orient at the programmed precession angle inducing chain-chain interaction. However, the structures collapse in the Mn = 5 simulation with θ_m nearly equal to zero. The limited mobility of the chains under this configuration inhibits chain-chain interaction, although particle restructuring within the individual columnar structures can potentially lead to the aforementioned lower energy relaxation.

Continuing, the stark drop in the average cluster size for mid-range precession angles in the Mn = 0.5 (Figure 7.11b) and Mn = 5 (Figure 7.11c) case at the end of the precession field step alludes to the formation of short chains that are ideal for certain applications such as vortex mixing, but not necessarily for strengthening the MR fluid. Video S5 in the supplementary material for a simulated Mn = 0.5, $\theta_f = 45^{\circ}$ configuration shows the formation of these micromixers, with small chain lengths averaging 3-4 particles constantly forming, fracturing, and restructuring [58]. Due to the hydrodynamic forces acting on these chains they are unable to fully connect the length of the simulation box, which we know from experiments can lead to sedimentation and a less responsive MR enhancement.

The large deviation between S at the end of the precession field interval and following the AC-DC transition for large θ_f for every Mn reinforces the impact that abrupt field transitions can have on a particle structure for large angles of precession. For the low Mn = 0.005 case this field transition yields the *segmented structures* whereas for the Mn = 50 case fracturing layered structures yield the *time-average to DC transition structures* and drives the average cluster size decrease. Videos showing the structural evolution of layer formation and subsequent fracturing for a Mn = 20, $\theta_f = 75^{\circ}$ simulation can be seen in the supplementary material (Video S6a and Video S6b) [58]. Continuing the discussion from Section 7.4.3 on field transitions, the simulation considers each particle as an instantaneous responsive dipole. The video showing the AC-DC transition (Video S6b) has been slowed down to emphasize the immediate response this field transition has on the system. As the external field returns to a uniaxial DC field oriented in the z-axis, the magnetic dipole of each particle orients vertically as well. As a result, the interaction between every particle in the horizontal layered structures becomes repulsive, rupturing the structures, and then leading to the restructuration of vertically aligned chains, which accounts for the drop in average cluster size.

In general, there is a trend of the cluster size peak shifting to larger precession angles for higher Mn, a similar trend witnessed in Figure 7.5 for the MR enhancement analysis. In theory as the Mn increases to infinity all field configurations with precession angles $\theta_f < 54.7^{\circ}$ will yield completely static columnar structures with a constant S, and with $\theta_f > 54.7^{\circ}$ will yield layered structures simply due to the respective attractive and repulsive magnetostatic interactions at play.

7.5 Conclusions

In this paper we have studied the structural and MR response of an MR fluid under a complete array of precession fields from uniaxial to rotational. By meticulously controlling the field strength components we are able to generate these precession fields by superimposing DC and rotational fields using a homemade triaxial magnetic field generator. We compared the structural response of the magnetically-responsive particles from videomicroscopy experiments to the rheometry tests where we quantified the MR enhancement through a close analysis of the storage modulus. Four experimental Mn scenarios, spanning five orders of magnitude, were tested to capture a thorough understanding of the complex magnetostatic and hydrodynamic forces that factor into the MR response.

We have found that the unsteady precession field configurations in which the columnar chain-like structure remains intact and endures the field transitions often lead to the highest MR enhancement over traditional uniaxial fields. For low Mn we have confirmed that lateral coalescence through chain interactions strengthens the structures. We also made an argument for Brownian relaxation playing an important role for $Mn \approx 1$ low angle precession fields where localized particle movement can encourage lower energy structuration that in turn would bolster its resistance to deformation. Finally, although the rheological response for high Mn pale in comparison to the other tested field configurations, the layered structures formed under rotational fields still hold great interest in a more bio-centric future work we plan to investigate.

Supplementary Material

In Section I we provide detailed information on the calibration of the triaxial magnetic field generator. In Section II we include supplementary material for videos referenced in the text.

Acknowledgements

This work was supported by MICINN PID2019-104883GB-I00 and TED2021-129384B-C22 projects, Junta de Andalucía P18-FR-2465 and A-FQM-396-UGR20 projects and European Regional Development Fund (ERDF). M.T. acknowledges FPI fellowship (BES-2017-079891).

References

[1] de Vicente, J., D. J. Klingenberg, and R. Hidalgo-Alvarez, "Magnetorheological fluids: a review," Soft Matter **7**, 3701-3710 (2011).

[2] Ginder, J. M., "Behavior of magnetorheological fluids," MRS Bull. **23**, 26-29 (1998).

[3] Bossis, G., O. Volkova, S. Lacis, and A. Meunier, "Magnetorheology: Fluids, structures and rheology," in *Ferrofluids: Magnetically Controllable Fluids and Their Applications*, Lecture Notes in Physics Vol. 594, edited by S. Odenbach (Springer-Verlag, Berlin, 2002), 202–230.

[4] Furst, E. M., and A. P. Gast, "Dynamics and lateral interactions of dipolar chains," Phys. Rev. E **62**, 6916 (2000).

[5] Wollny, K., J. Läuger, and S. Huck, "Magneto sweep–A new method for characterizing the viscoelastic properties of magneto-rheological fluids," Appl. Rheol. **12**, 25-31 (2002).

[6] Ashtiani, M., S. H. Hashemabadi, and A. Ghaffari. "A review on the magnetorheological fluid preparation and stabilization." J. Magn. Magn. Mater. **374**, 716-730 (2015).

[7] Sidpara, A., and V. K. Jain, "Experimental investigations into surface roughness and yield stress in magnetorheological fluid based nano-finishing process," Int. J. Precis. Eng. Man. **13**, 855-860 (2012).

[8] Bica, I., Y. D. Liu, and H. J. Choi, "Physical characteristics of magnetorheological suspensions and their applications," J. Ind. Eng. Chem. **19**, 394-406 (2013).

[9] Ahamed, R., S. B. Choi, and M. M. Ferdaus, "A state of art on magneto-rheological materials and their potential applications," J. Intel. Mat. Syst. Str. **29**, 2051-2095 (2018).

[10] Bombard, A. J. F., and J. de Vicente, "Boundary lubrication of magnetorheological fluids in PTFE/steel point contacts," Wear **296**, 484-490 (2012).

[11] Rosa, W. O., F. Vereda, and J. de Vicente, "Tribological behavior of glycerol/water-based magnetorheological fluids in PMMA point contacts," Front. Mater. **6**, 32 (2019).

[12] Morillas, J. R., and J. de Vicente, "Magnetorheology: a review," Soft Matter **16**, 9614-9642 (2020).

[13] Wereley, N. M., A. Chaudhuri, J. H. Yoo, S. John, S. Kotha, A. Suggs, ... and T. S. Sudarshan, "Bidisperse magnetorheological fluids using Fe particles at nanometer and micron scale," J. Intel. Mat. Syst. Str. **17**, 393-401 (2006).

[14] Li, W. H., and X. Z. Zhang, "A study of the magnetorheological effect of bimodal particle based magnetorheological elastomers," Smart Mater. Struct. **19**, 035002 (2010).

[15] Morillas, J. R., A. J. F. Bombard, and J. de Vicente, "Enhancing magnetorheological effect using bimodal suspensions in the single-multidomain limit," Smart Mater. Struct. **27**, 07LT01 (2018).

[16] Fang, F. F., J. H. Kim, and H. J. Choi, "Synthesis of core–shell structured PS/Fe3O4 microbeads and their magnetorheology," Polymer **50**, 2290-2293 (2009).

[17] Wu, W. P., B. Y. Zhao, Q. Wu, and K. A. Hu, "The strengthening effect of guar gum on the yield stress of magnetorheological fluid," Smart Mater. Struct. **15**, N94 (2006).

[18] López-López, M. T., J. de Vicente, F. González-Caballero, and J. D. G. Durán, "Stability of magnetizable colloidal suspensions by addition of oleic acid and silica nanoparticles," Colloid Surface A **264**, 75-81 (2005).

[19] Liu, Y. D., H. J. Choi, and S. B. Choi, "Controllable fabrication of silica encapsulated soft magnetic microspheres with enhanced oxidation-resistance and their rheology under magnetic field," Colloid Surface A **403**, 133-138 (2012).

[20] Morillas, J. R., A. J. F. Bombard, and J. de Vicente, "Preparation and characterization of magnetorheological fluids by dispersion of carbonyl iron microparticles in PAO/1-octanol," Smart Mater. Struct. **25**, 015023 (2016)

[21] Zrinyi, M., "Intelligent polymer gels controlled by magnetic fields," Colloid Polym. Sci. **278**, 98-103 (2000).

[22] Lim, S. T., M. S. Cho, I. B. Jang, and H. J. Choi, "Magnetorheological characterization of carbonyl iron based suspension stabilized by fumed silica," J. Magn. Magn. Mater. **282**, 170-173 (2004).

[23] Viota, J. L., J. de Vicente, J. D. G. Duran, and A. V. Delgado, "Stabilization of magnetorheological suspensions by polyacrylic acid polymers," J. Colloid Interf. Sci. **284**, 527-541 (2005).

[24] Guerrero-Sanchez, C., T. Lara-Ceniceros, E. Jimenez-Regalado, M. Raşa, and U. S. Schubert, "Magnetorheological fluids based on ionic liquids," Adv. Mater. **19**, 1740-1747 (2007).

[25] Bombard, A. J. F., F. R. Gonçalves, and J. de Vicente, "Magnetorheology of carbonyl iron dispersions in 1-alkyl-3-methyl-imidazolium ionic liquids," Ind. Eng. Chem. Res. **54**, 9956-9963 (2015).

[26] Shahrivar, K., and J. de Vicente, "Thermoresponsive polymer-based magneto-rheological (MR) composites as a bridge between MR fluids and MR elastomers," Soft Matter **9**, 11451 (2013).

[27] Shahrivar, K., and J. de Vicente, "Thermogelling magnetorheological fluids," Smart Mater. Struct. **23**, 025012 (2014).

[28] Laun, H. M., C. Kormann, and N. Willenbacher, "Rheometry on magnetorheological (MR) fluids," Rheol. Acta **35**, 417-432 (1996).

[29] Laun, H. M., G. Schmidt, C. Gabriel, and C. Kieburg, "Reliable plate–plate MRF magnetorheometry based on validated radial magnetic flux density profile simulations," Rheol. Acta **47**, 1049-1059 (2008).

[30] Morillas, J. R., J. Yang, and J. de Vicente, "Double-gap plate-plate magnetorheology," J. Rheol. **62**, 1485-1494 (2018).

[31] Martin, J. E., and A. Snezhko, "Driving self-assembly and emergent dynamics in colloidal suspensions by time-dependent magnetic fields," Rep. Prog. Phys. **76**, 126601 (2013).

[32] Biswal, S. L., and A. P. Gast, "Micromixing with linked chains of paramagnetic particles," Anal. Chem. **76**, 6448-6455 (2004).

[33] Martin, J. E., L. Shea-Rohwer, and K. J. Solis, "Strong intrinsic mixing in vortex magnetic fields," Phys. Rev. E **80**, 016312 (2009).

[34] Halsey, T. C., R. A. Anderson, and J. E. Martin, "The rotary electrorheological effect," Int. J. Mod. Phys. B **10**, 3019-3027 (1996).

[35] Martin, J. E., R. A. Anderson, and C. P. Tigges, "Simulation of the athermal coarsening of composites structured by a biaxial field," J. Chem. Phys. **108**, 7887-7900 (1998).

[36] Melle, S., O. G. Calderón, M. A. Rubio, and G. G. Fuller, "Microstructure evolution in magnetorheological suspensions governed by Mason number," Phys. Rev. E **68**, 041503 (2003).

[37] Nagaoka, Y., H. Morimoto, and T. Maekawa, "Ordered complex structures formed by paramagnetic particles via self-assembly under an ac/dc combined magnetic field," Langmuir **27**, 9160-9164 (2011).

[38] Martin, J. E., R. A. Anderson, and R. L. Williamson, "Generating strange magnetic and dielectric interactions: Classical molecules and particle foams," J. Chem. Phys. **118**, 1557-1570 (2003).

[39] Martin, J. E., E. Venturini, G. L. Gulley, and J. Williamson, "Using triaxial magnetic fields to create high susceptibility particle composites," Phys. Rev. E **69**, 021508 (2004).

[40] Snezhko, A., M. Belkin, I. S. Aranson, and W. K. Kwok, "Self-assembled magnetic surface swimmers," Phys. Rev. Lett. **102**, 118103 (2009).

[41] Snezhko, A., and I. S. Aranson, "Magnetic manipulation of self-assembled colloidal asters," Nat. Mater. **10**, 698-703 (2011).

[42] Pardo, A., M. Gómez-Florit, S. Barbosa, P. Taboada, R. M. Domingues, and M. E. Gomes, "Magnetic nanocomposite hydrogels for tissue engineering: design concepts and remote actuation strategies to control cell fate," Acs Nano **15**, 175-209 (2021).

[43] Martin, J. E., and G. Gulley, "Field-structured composites for efficient, directed heat transfer," J. Appl. Phys. **106**, 084301 (2009).

[44] Solis, K. J., and J. E. Martin, "Isothermal Magnetic Advection: Creating functional fluid flows for heat and mass transfer," Appl. Phys. Lett. **97**, 034101 (2010).

[45] Donado, F., U. Sandoval, and J. L. Carrillo, "Kinetics of aggregation in non-Brownian magnetic particle dispersions in the presence of perturbations," Phys. Rev. E **79**, 011406 (2009).

[46] Moctezuma, R. E., F. Donado, and J. L. Arauz-Lara, "Lateral aggregation induced by magnetic perturbations in a magnetorheological fluid based on non-Brownian particles," Phys. Rev. E **88**, 032305 (2013).

[47] Terkel, M., and J. de Vicente, "Magnetorheology of exotic magnetic mesostructures generated under triaxial unsteady magnetic fields," Smart Mater. Struct. **30**, 014005 (2020).

[48] Terkel, M., J. Tajuelo, and J. de Vicente, "Enhancing magnetorheology with precession magnetic fields," J. Rheol. **66**, 67-78 (2022).

[49] Fernández-Toledano, J. C., J. A. Ruiz-López, R. Hidalgo-Álvarez, and J. de Vicente, "Simulations of polydisperse magnetorheological fluids: A structural and kinetic investigation," J. Rheol. **59**, 475-498 (2015).

[50] Gorodkin, S. R., R. O. James, and W. I. Kordonski, "Magnetic properties of carbonyl iron particles in magnetorheological fluids," J. Phys. Conf. Ser. **149**, 012051 (2009).

[51] Shahrivar, K., E. Carreón-González, J. R. Morillas, and J. de Vicente, "Aggregation kinetics of carbonyl iron based magnetic suspensions in 2D," Soft Matter **13**, 2677-2685 (2017).

[52] Melle, S., O. G. Calderón, G. G. Fuller, and M. A. Rubio, "Polarizable particle aggregation under rotating magnetic fields using scattering dichroism," J. Colloid Interf. Sci. **247**, 200-209 (2002).

[53] Martin, J. E., "Theory of strong intrinsic mixing of particle suspensions in vortex magnetic fields," Phys. Rev. E **79**, 011503 (2009).

[54] Tajuelo, J., Ó. Martínez-Cano, J. R. Morillas, J. Yang, and J. de Vicente, "Generation of Synchronized High-frequency Triaxial Magnetic Fields using Fractal Capacitors Banks," 2023 under revision.

[55] Massana-Cid, H., D. Levis, R. J. H. Hernández, I. Pagonabarraga, and P. Tierno, "Arrested phase separation in chiral fluids of colloidal spinners," Phys. Rev. Research, *3*(4), L042021. (2021)

[56] Camacho, G. "Magnetorheology under toggled fields" In preparation

[57] Schmidt, A. M., "Thermoresponsive magnetic colloids," Colloid Polym. Sci. **285**, 953-966 (2007).

[58] See supplementary material https://www.scitation.org/doi/suppl/10.1122/8.0000646 for videos referenced in the text and a PDF document discussing them in more detail.

Chapter 8

Magnetic Self-Assembled Particle Scaffolds in Hydrogels for Regenerative Medicine

Manuscript *in preparation*

Abstract

Muscle, nerve, and cartilage cells are all known to have a complex hierarchical organization in native biological tissues. Imitating cellular alignment in a compatible extracellular matrix that mimics native tissues is a difficult task, especially in hydrogels whose randomly crosslinked polymer network inherently takes on an isotropic matrix. Here, we propose an innovative method of formulating biocompatible structured hydrogels with magnetic particles under high frequency magnetic fields. Through triaxial magnetic field control we show a pathway to generating anisotropic structural self-assembly in an amine-reactive oxidized laminarin and gelatin hydrogel precursor solution. Upon gelation, the external field can be removed, and a 3D particle structure remains stabilized. This structure, in turn, provides the necessary directional cues for guided cell growth. The unique ability of structuring these hydrogels in their liquid phase would make them applicable for less invasive in vivo cell regeneration treatments.

8.1 Introduction

Injectable hydrogels intended for tissue regeneration applications pose a compelling pathway for less invasive biomedical therapies [1-2]. Transplantation of externally constructed bioengineered tissue scaffolds to the injured site requires a surgical procedure that risks additional tissue damage. An injectable hydrogel solution containing the necessary biological precursors to mimic native tissue would conform and mold to the damage site and solidify *in situ* [3]. One major limitation working with traditional hydrogels is the randomly oriented polymer network, whose isotropic properties differ from native tissue, which typically possess a highly anisotropic ordered structure in both cellular alignment and the surrounding extracellular matrix [4-5]. Therefore, developing experimental techniques to induce anisotropic structuring in hydrogels through an external stimulus is vital particularly for their successful implementation *in situ*.

Recently magnetic particles have been incorporated into the design of magnetic hydrogels [6]. Magnetic particles can be highly responsive to magnetic fields and are known to structure in line with the external field giving rise to an anisotropic architecture – the desirable component missing from unmodified polymer hydrogels [7]. Oriented cell structuring assisted by

magnetic particles can be executed through direct (i.e. active) or indirect methods. In the former case, cells can intake superparamagnetic iron oxide nanoparticles via endocytosis thus giving them a magnetic functionality [8]. An external magnetic field would induce a dipole in the cell that would then lead to the active oriented structuring of the cells in line with the external field. The formation of magnetic nanoparticles' embedded cell clusters, or spheroids, prior to spheroid alignment also showed success in structuring tissue fibers of different scales [9].

Indirect methods to oriented cell alignment would involve cells subsequently being structured as the result of actively structuring the microenviroment surrounding the cells [10]. High intensity magnetic fields, sometimes even upwards of 10 T, can orient what one would consider a non-magnetic anisotropic material such as collagen fibrils or cellulose nanocrystals, due to their diamagnetic susceptibility [4]. While not ideal given the extreme fields necessary, there has been some success in structuring these diamagnetic materials that in turn provides an anisotropic architecture for cell seeding and alignment. In recent years, a new type of injectable hybrid hydrogels known as anisogels have shown anisotropic structuring using more magneto-receptive elongated microelements requiring less intense field strengths on the order of 100-300 mT [4,11]. For example, guided neuron alignment and neurite outgrowth was shown to follow in parallel with magnetic particle-doped rod-shaped microgels previously aligned during the uncrosslinked hydrogel gelling phase [12-13]. In fact, it is believed that cells can sense these microelements in the surrounding extracellular matrix and grow in parallel without direct physical interaction. Electrospun and cryosectioned poly (lactide-co-glycolide) (PLGA) and polycaprolactone (PCL) microfibers containing magnetic nanoparticles have also demonstrated induced oriented cell growth in anisogels and 3D bioprinted anisotropic hydrogels, respectively [14-15].

In this work we aim to self-assemble complex anisotropic particle scaffold microstructures spanning the entirety of our injectable hydrogels for cell seeding and oriented cell growth applications using uniaxial and time-varying biaxial and triaxial magnetic fields. Advance particle structuring has typically been studied for colloidal suspensions and magnetorheological (MR) fluid systems, and less so for gelling systems and to our knowledge not attempted on biological hydrogels. A constantly evolving carrier fluid driven by polymer crosslinking and increasing viscosity until complete gelation could certainly impede dynamic particle structuring. Martin et al. have extensively studied

particle dynamics under time-dependent magnetic fields and the particle microstructures that emerge [16]. In their work, heterodyned fields induce the formation of 3D particle foams and honeycomb structures, and were able to arrest these structures in a polyester liquid polymer casting resin in order to carry out measurements of the magnetic susceptibility, as well as the electrical and thermal conductivities, which all showed appreciative increases in the anisotropic composites [17]. Terkel et al. similarly worked with biaxial and triaxial fields to enhance the rheological response of their MR fluid system. In doing so they analyzed both chain-like and banded structures for low and high particle concentrations in a polydimethylsiloxane (PDMS) polymeric gel [18]. Both Martin and Terkel's structured gels could be considered nonviable for biological systems and the polymers were cured using high temperatures, which is not feasible for in situ tissue regeneration applications. However, motivated by the possibility to structure more intricate and unique anisotropic particle scaffolds, we have adapted their work for our natural crosslinking injectable hydrogel.

In this manuscript, we demonstrate a promising route to formulate injectable magnetic hydrogels with anisotropic particle microstructures prime for cell deposition and made possible with our homemade triaxial magnetic field generator. First we define our hydrogel system, the oxidized laminarin (oxLAM) and gelatin polymer components, and identify a viable concentration of the former component for particle structuring. Then we detail the fundamental background of dipolar and time-averaged magnetostatic interactions for the simple uniaxial case, and for the more complicated biaxial and triaxial field configurations employed in this work. The main objective of the experimental work is to promote the formation of anisotropic particle scaffolds only made possible with more advance multidimensional and time-varying external fields, to provide an ideal microenvironment for cell seeding and intended for eventual oriented cell growth studies. Finally, we present optical and confocal microscopy results of our structured hydrogels for an array of exciting scaffold types and demonstrate structural endurance and cell viability over a multi-day study.

8.2 Results and discussion

In recent years magnetically responsive particles have been incorporated into hydrogels with the intention to drive oriented cell growth. Magnetic particles

are added to the hydrogel precursor solution and structured prior to the polymer crosslinking. These experiments typically have been carried out using a magnet, or a pair of magnets in parallel, to generate a uniaxial (DC) external field that induces a dipolar moment in the suspended particles. Whether these particles are freely suspended in the hydrogel precursor solution, encapsulated in microelements (anisotropic microgels, for example), or within cells, an external field application will drive directional alignment [4,6]. In some cases a coil, or a looped conducting wire, has been used to generate the magnetic field. When a current is applied through the coil a magnetic field is produced in the direction through the center following the right hand rule. While coils can be used for structuring purposes, many studies have solely utilized them for post-gelation magnetomechanical stimulation [19]. The benefit of working with coils is the ability to generate time-varying magnetic fields through alternating currents (AC), with control over both the field frequency and field intensity. In particular, Helmholtz coils have been shown to generate nearly uniform field lines, an advantage over magnets, which typically have a narrower region of homogenous fields.

While magnets or single coils are effective experimental setups for inducing an external field, they are limited to the uniaxial kind. Biaxial and triaxial magnetic manipulation of suspended particles in a carrier fluid have yielded a number of more complex particle mesostructures, made possible by capitalizing on the versatility of more advanced field generators capable of generating three-dimensional DC and AC fields, and superimposing a combination of the two [17-18]. Magnetic particles of the micron size are also far more responsive to static and time-varying fields, whereas in the case of nanoparticles, interactions are predominantly governed by Brownian motion and lack the necessary field-driven response for the formation of complex particle scaffolds. For this reason, we have employed micron-sized particles in this work.

When working with dispersions of micronsized magnetic particles one must consider the relation between the magnetostatic (F_M) and hydrodynamic (F_H) forces at play. The Mason number is a nondimensional parameter defined as the ratio of these two forces, $\mathrm{Mn} = F_H/F_M$. For $\mathrm{Mn} < 1$ the magnetic forces dominate the system, whereas for $\mathrm{Mn} > 1$ the system is dominated by the hydrodynamic forces. This relation is pivotal for predicting whether magnetic particles suspended in a carrier fluid will aggregate according to a deterministic dipolar tip-to-tip mechanism ($\mathrm{Mn} < 1$) under uniaxial fields or be driven to

structure by means of time-averaged interactions ($\mathrm{Mn} > 1$) when exposed to high-frequency biaxial and triaxial fields. In addition to the applied magnetic field configuration, F_M is strongly dependent on the particle size, $F_M \propto a^6$. On the other hand, F_H acting on a spherical particle is primarily influenced by the viscosity of the carrier fluid and the particle velocity via the field frequency, $F_H \propto \eta\omega$.

Structuring magnetic particle scaffolds in a gelling hydrogel precursor solution is not trivial. The crosslinking between the oxidized laminarin (oxLAM) and gelatin polymer components increases the hydrogel viscosity physically, and therefore Mn, hence restricting particle movement. In this work, the initial viscosity of the hydrogel precursor solution and the gelling time is controlled by adjusting the laminarin concentration. A schematic of the hydrogel formulation is shown in Figure 8.1 and a summary of the individual component concentrations of the hydrogels employed in this work is detailed in Table 8.1. In Figure 8.2 we show the measured viscosity of our gelling solution for four different laminarin concentrations. By reducing the oxLAM concentration the initial viscosity value similarly decreases. Furthermore, this lower measured viscosity value is constant for upwards of 50 s for the 1.25% and 300 s for the 0.5% and 0.625% oxLAM samples, respectively, before we witness the rapid crosslinking process takes place as represented by the viscosity increase of two orders of magnitude. As a note, an additional 90 s should be added to these times to more accurately represent the total time from polymer mixing to reaching the gelling point given the time it takes to load and initiate the rheometer program. A similar loading time was measured for the videomicroscopy experiments later discussed. Logically, particle scaffold structuration would ideally take place during these early gelling times to take advantage of the lower viscosity, which benefits both dipolar and time-averaged magnetostatic interactions. oxLAM concentrations for 0.625% and 0.5% have the lowest measured initial viscosities of 0.028 Pa s and 0.016 Pa s, respectively, with an estimated overall gelling time of 20-25 minutes. These longer gelling times could put non-magnetic additives (under the field), such as cells, at risk of sedimentation leading to a non-homogenous dispersion throughout the resultant hydrogel. Therefore, there is some margin to delay the sample loading and subsequent structuration after mixing the polymers until 5 min into the gelling time to reduce the likelihood of cell sedimentation.

The most novel aspect of working with our triaxial magnetic field generator is the ability to generate meticulously programmed field configurations and

Table 8.1 Formulations of the final precursor solutions for the various hydrogels prepared in this work.

Acronym	oxLAM (w/v %)	Gelatin (w/v %)	MP EW (w/v %)	HA (v/v %)	Ca (v/v %)	DMEMsup (v/v %)	Gel time (min)	Location
L2.5G5HA1	2.5	5	-	1	-	99	2-3	Fig. 8.2
L1.25G5HA1	1.25	5	-	1	-	99	4-5	Fig. 8.2
LGHACa	0.625	2.5	-	5	2.4	92.6	15-20	Fig. 8.2, 8.4
L0.5GHACa	0.5	2.5	5.5	5	2.4	92.6	20-25	Fig. 8.2, 8.5
LGHACaMP5.5	0.625	2.5	5.5	5	2.4	92.6	15-20	Fig. 8.3, 8.4
LGHACaMP10*	0.625	2.5	10*	5	2.4	92.6	15-20	Fig. 8.3
L0.5GHACaMP5.5	0.5	2.5	5.5	5	2.4	92.6	20-25	Fig. 8.5

*In this hydrogel formulation we employed 1 μm size magnetic latex Dynabead particles rather than carbonyl iron (grade EW) particles

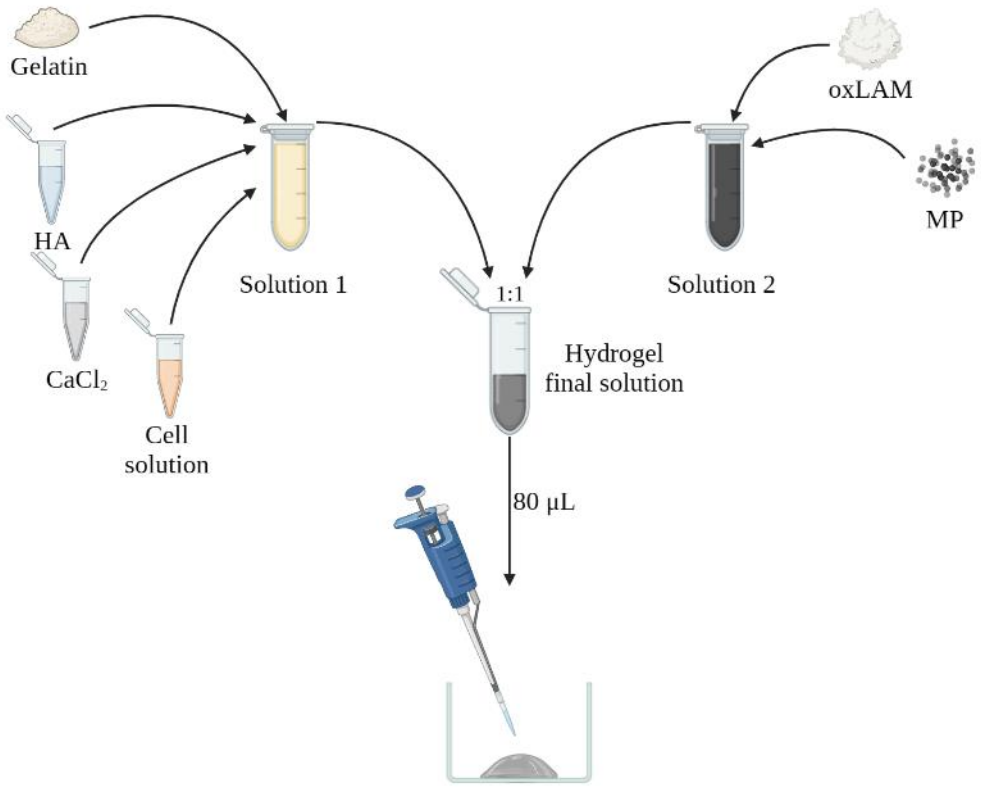

Figure 8.1 Schematic of the oxLAM and gelatin polymer mixture, and their additional components, used to synthesize our magnetic hydrogels. The cell culture is added to the gelatin solution while the magnetic particles are added to the oxLAM solution prior to combining the two solutions in a 1:1 by volume mixture. DMEMsup is the continuous phase of each solution component.

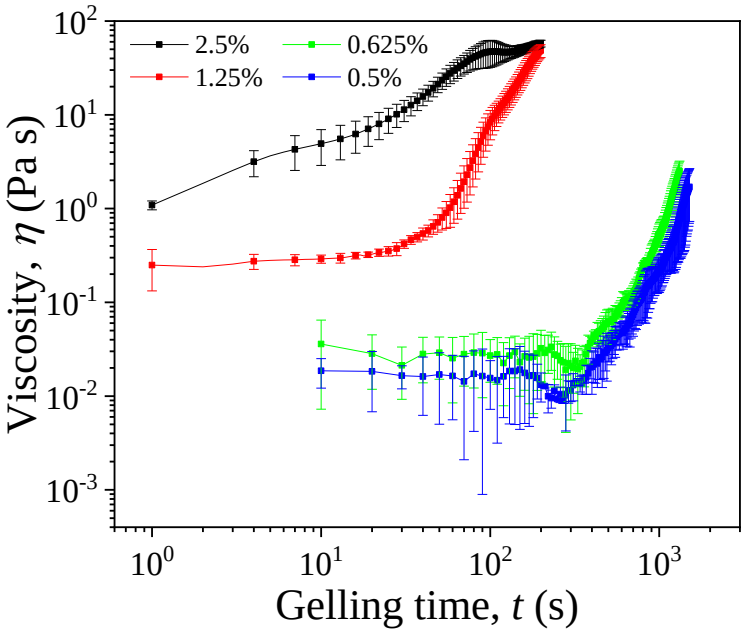

Figure 8.2 Time dependent viscosity curves at a shear rate of 1 s^{-1} for different oxLAM concentrations in the hydrogel precursor solution. We identify the ideal structuring time interval for each concentration as the length of time in which the viscosity remains steadily constant. For the 0.5% (L0.5GHACa) and 0.625% (LGHACa) this time is around 300 s, and for the 1.25% (L1.25G5HA1) around 50 s. Beyond this time crosslinking rapidly increases and thus increases the measured viscosity until reaching the gelling point. The 2.5% (L2.5G5HA1) oxLAM concentration already shows signs of gelation at the start of the rheometry measurements and was determined unsuitable for magnetic structuring. Both the 0.5% and 0.625% concentrations are appropriate candidates for magnetic structuring given their low initial viscosities being about one magnitude greater than water. Each oxLAM concentration was measured three times.

induce the formation of 3D particle scaffolds spanning the entirety of our hydrogel samples. In this work we have chosen to highlight the following selection of field configurations of increasing complexity and order, and the distinct emergent particle structure types that form in our hydrogels as illustrated in Figure 8.3. Here, each structure type is shown from a top view (z-axis directed coming out of the plane of the paper) in brightfield microscopy (panels 1) and confocal microscopy (panels 2). An angled perspective of the 3D confocal renderings is shown in panels 3. Then, in the following Figure 8.4 we show cell encapsulation for our structured hydrogels as well as a control (without magnetic particles) and unstructured case.

Uniaxial field and columnar structures

The simplest, and most straightforward, configuration is the uniaxial magnetic field (Fig. 8.3, panels A1-A3). A constant DC field, although traditional, is effective in inducing a magnetic moment in a particle aligned in the direction of the external field:

$$m = \frac{4}{3}\pi a^3 M \tag{8.1}$$

where the particle magnetization $M = 3\beta H_0$ with the contrast factor, β, indicating how susceptible a magnetic particle is to an external field depending on its material and composition. The carbonyl iron particles (CIPs, grade EW) used in our hydrogels have a relatively high contrast factor of $\beta = 0.65$ (magnetic particles in conventional MR fluids have a maximum contrast factor of 1 for low field strengths), which aids in their swift structuring response. To maintain elevated particle structures we imposed the uniaxial field in the vertical direction $\vec{H} = H_z\hat{z}$. The angled images in Fig. 8.3 clearly show that the particle scaffolds fill the volume of the sample chamber.

When applied, a uniaxial field will drive individual particles to structure in line with the external field forming chains or thicker columnar structures. Depending on the concentration of particles and the resulting spatial distribution of columnar structures, encapsulated cells within the particle scaffold could, in theory, be predisposed to grow parallel to the columns given their lateral restriction. In our experiments working with a particle concentration of $\phi = 5.5$ w/v % we estimated inter-column distances of 10-100 μm, which is large enough for an individual fibroblast cell of 5 μm in diameter to settle. In Fig. 8.4 (panels A1-A2) we see the fibroblasts cells mostly appear to be anchored to the particle scaffold.

High-frequency biaxial perturbation field and layered structures

High frequency biaxial rotational and perturbation fields are known to drive the formation of layered structures as a result of the time-averaged magnetostatic interactions. We have chosen to work with perturbation fields, instead of rotating fields, to maximize the field strength output of our field generator. These time-varying fields consist of an oscillatory field applied orthogonal to a static field:

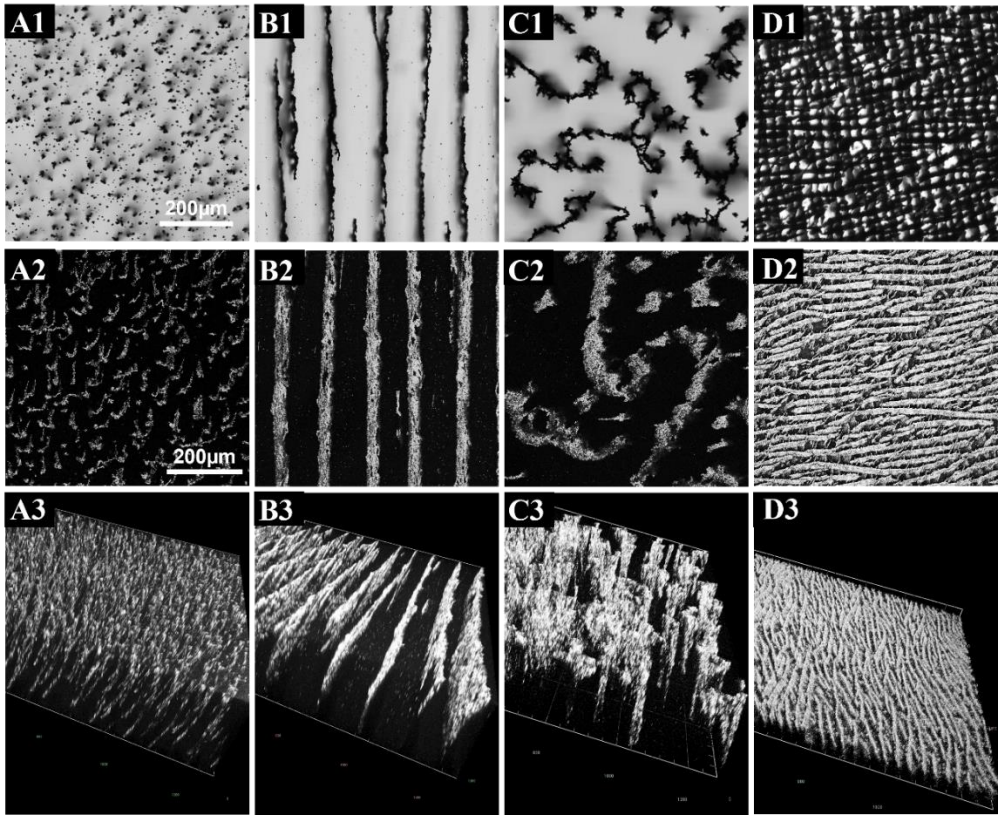

Figure 8.3 Bright-field (1) and confocal (2,3) microscopy of four different structured hydrogels, including a) chains, b) bands, c) spirals, and d) crosshatch. These hydrogels contain 0.625% oxLAM concentration with an initial viscosity of the hydrogel precursor solution of 0.028 Pa s. The chains and bands hydrogels were structured 5 minutes after combining the two solution components, whereas the spirals and crosshatch were structured immediately after mixing the final solution. The carbonyl iron particle structures in A-C (LGHACaMP5.5) span the entirety of the 300 µm in height sample chamber. However, the magnetic latex particles of the crosshatch structure in D (LGHACaMP10) are shown to have sedimented.

$$\vec{H} = H_z\hat{z} + H_x \sin 2\pi f t\, \hat{x} \tag{8.2}$$

where H_z and H_x are the static and oscillating field strength components, respectively, and f the field frequency of the latter. Here, by imposing the static field in the vertical direction we observed more erect and well-defined layered structures than in the case of employing a rotational field. For our experiments $H_z = 5.6$ kA m^{-1}, $H_x = 15.5$ kA m^{-1}, and $f = 100$ s^{-1}. The resultant perturbation angle using these field strengths is around $\theta_f = 70^o$ deviating from the z-axis.

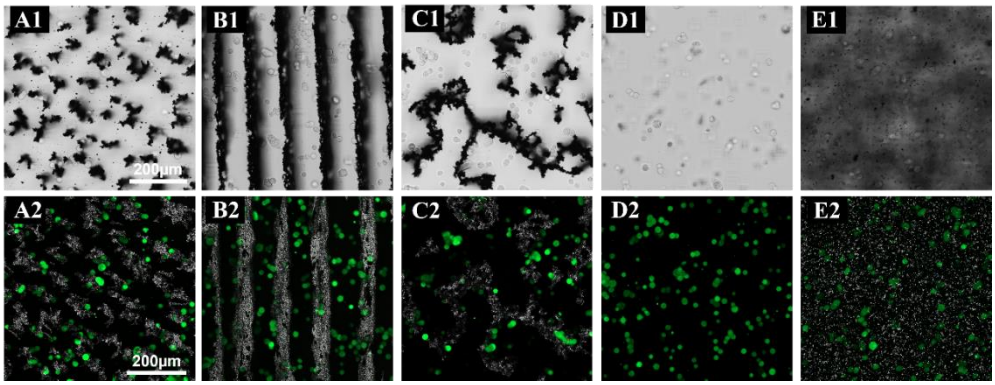

Figure 8.4 Bright-field (1) and confocal (2) microscopy images of the three distinct magnetic hydrogels (LGHACaMP5.5) consisting of a) chains, b) bands, and c) spiral structures with encapsulated fibroblast cells. In d) we show the control hydrogel (LGHACa) containing cells but without particles, and in e) the hydrogel contains cells and unstructured magnetic particles. The embedded cells were stained with 1 μL/mL of Calcein and observed under an excitation and emission wavelength of 494 nm and 517 nm, respectively. These images were captured on the day the hydrogels were fabricated and we note a similarly uniform dispersion of cells among the structured hydrogels as in the control case. In some cases, the cells appear to adhere to the particle scaffold and in other cases are completely isolated between the neighboring particle structure.

In any external field application two magnetic dipoles, m_1 and m_2, interact according to the following potential equation:

$$V(r) = \frac{3(m_1 \cdot \hat{r})(m_2 \cdot \hat{r}) - m_1 \cdot m_2}{4\pi r^3} \tag{8.3}$$

Where r is the distance of the line of centers between the two dipoles, and $\hat{r} = \vec{r}/r$ being the radial unit vector, with $\vec{r} = x\hat{x} + y\hat{y} + z\hat{z}$ in cartesian coordinates.

As mentioned, the formation of layered structures is due to the time-averaged magnetostatic interactions between particles under these high-frequency perturbation fields, where the hydrodynamic forces acting on the particles overcome the magnetic forces and inhibit chain formation. In the case that m_1 is located at the origin and $m_1 = m_2 = m$ (Eqn. 8.1) the above equation can be reduced for the time-averaged potential for a perturbation field configuration (Eqn. 8.2) to the following:

$$\langle V(r)\rangle = \frac{(4\pi a^3\beta)^2}{4\pi r^3} \cdot \left[-\frac{1}{2}H_x^2(1-3\sin^2\theta\cos^2\phi) - H_z^2(1-3\cos^2\theta)\right] \quad (8.4)$$

where θ and ϕ are the polar and azimuthal angle between the two dipoles, respectively. Incorporating the component field strengths we employed in our experiments, the term in brackets is largely positive, in this case indicating attraction, for dipole interactions in the x,z-plane where $\phi = 0^o$ and $-180^o < \theta < 180^o$. Additionally, the interaction between a dipole at the origin and the other directed along the y-axis ($\phi = 90^o$ and $\theta = 90^o$), as would be the case for two particles in the same position in neighboring layered structures, the term in brackets is negative, indicating a repulsive interaction. Therefore, it becomes clear that both the net attraction in the x,z-plane and repulsive force directed in the y-axis are the key time-averaged magnetostatic interactions at play that drive the formation of layered structures.

The separation distance of these layered structures depends both on the particle concentration and height of the sample chamber. The images shown in Fig. 8.3 are of hydrogel samples contained in a 300 μm height chamber. Under our experimental conditions we see in panels B1 and B2 separation distances of roughly 100-150 μm. Although single particle width layered structures are energetically favored, in experimental practice we witness some variation in the layer thickness. This can be due to particle aggregates forming before the field is applied, remnant magnetism in the particles, or a predisposed electrostatic interaction caused by oxidation. However, layer thickness is evidently much smaller compared to the separation distance. In Fig. 8.4 (panels B1 and B2) we also observe free-standing cells in the gaps between particle structures.

Triaxial fields and spiral/crosshatched structures

Moving on to triaxial magnetic field configurations we will first focus on precession fields. Precession fields are generated by superimposing a rotating field with a uniaxial static field, in our experimental setup the rotating field was induced in the x,y-plane and the static field directed in z-axis. The resulting triaxial field thus takes on the following form:

$$\vec{H} = H_z\,\hat{z} + H_{x,y}[\sin(\omega t)\hat{x} + \cos(\omega t)\hat{y}] \tag{8.5}$$

where $H_{x,y}$ is the field amplitude in both the x,y-axes, notably applied in quadrature phase, and $\omega = 2\pi f$ is the rotational field frequency. The resultant field vector has a strength of $H_0 = \left({H_z}^2 + {H_{x,y}}^2\right)^{1/2}$ with an angle of precession $\theta_f = \tan^{-1}\left(H_{x,y}/H_z\right)$. These values are necessary to fine tune the Mn calculation required in programming the optimal field configuration to promote the formation of spiral structures.

Terkel *et al.* (2023) illustrates and maps out the various 3D particle structures that self-assemble in their MR fluid system according to Mn and θ_f [20]. They define the Mn for a precession field as follows:

$$\mathrm{Mn} = \frac{12^2 \eta \omega \sin\theta_f}{\mu_0 M^2} \tag{8.6}$$

Here $\mu_0 = 4\pi \times 10^{-7}$ Tm A^{-1} is the permeability of a vacuum. In their work they identify a small range of Mn and θ_f that yields the spiral structure type, Mn $\sim$ 20 and $\theta_f \sim 45°$. By extracting the initial viscosity measurement for the 0.5% oxLAM hydrogel sample from Fig. 8.2, $\eta = 0.016$ Pa s, we can then determine suitable H_0 and f values that derives comparable Mn and θ_f values. We ultimately optimized the precession field configuration with the field components $H_{x,y} = H_z = 5.6$ kA m^{-1} with a resultant field strength of $H_0 =$ 7.9 kA m^{-1}, and $f = 545$ s^{-1}.

The spiral-like particle mesostructure would give cells a more labyrinthine playground to settle and proliferate, with the expectation that such an anisotropic scaffold would provide the micromechanical cues for coordinated cell growth and alignment. The larger separation distances in this structure type similarly resulted in free-standing cells post-gelation with some cells nestled more closely and in contact within the nooks of the structure, as seen in Fig. 8.4 (panels C1 and C2).

Next, inspired by Nagaoka's crosshatched 2D structures and Martin's 3D porous structures we set out to similarly self-assemble a 3D crosshatch structure in our hydrogel [16,21]. This particle scaffold type would promote

compartmentalized cell deposition during the hydrogel gelling phase. In order to bring the crosshatched structures into a 3D orientation, we superimposed two oscillatory fields of commensurate field strength but distinct field frequencies orthogonal to one another, and orthogonal to a static field directed in the z-axis. Essentially one can consider these field components as two competing high-frequency perturbation fields whose time-averaged magnetostatic interactions drive the formation of 3D crosshatched structures. For these experiments we worked with smaller 1 μm size Dynabead particles (Invitrogen by ThermoFisher, $\beta = 0.35$). By working with smaller particles we expect that Brownian interactions assist and are necessary in the formation of these structures. The larger CIPs, whose magnetic interactions dominate thermal fluctuations, were unable to reach an equilibrium state that yielded the desired 3D crosshatch pattern under the superimposed orthogonal oscillatory fields. Ultimately, despite promising brightfield microscopy results of the crosshatched structured hydrogel (Fig. 8.3, panel D1), the confocal images (Fig. 8.3, panels D2-D3) reveal that in one axis layered structures are formed and in the orthogonal direction exist chainlike connections. From an aerial perspective it appears that crosshatch structures are formed but, in fact, the final structure is predominately consistent with the layered structure type albeit with small separation distance between the banded structures. For this reason, in the cell encapsulation experiments (Fig. 8.4) we only show the layered structures formed under the high frequency biaxial perturbation magnetic field configuration.

Finally, we chose to carry out a multi-day study of the encapsulated cells in a 0.5% oxLAM hydrogel that was structured with banded particle scaffolds using the high-frequency perturbation field. Confocal images of these results are shown in Figure 8.5. The 0.5% oxLAM hydrogel formulation was chosen over 0.625% because preliminary studies suggested that the lesser concentration resulted in a more open crosslinked polymer network whose larger porosity facilitated cell extension. As early as Day 4 we begin to see cell extension and alignment that follows in parallel with the particle structure. Through micromechanical stress cues it is expected that the cells recognize these structural barriers and extend and proliferate in the direction of least resistance, or within the compartmentalize particle-vacant regions. In Fig. 8.5 (panels A and B) we show an angled confocal perspective of cell proliferation in a particle-free and banded hydrogel, respectively. In the latter case the particle structures (white channel) have been removed in post-processing of the images leaving behind only the cells to be visualized. After 8 days

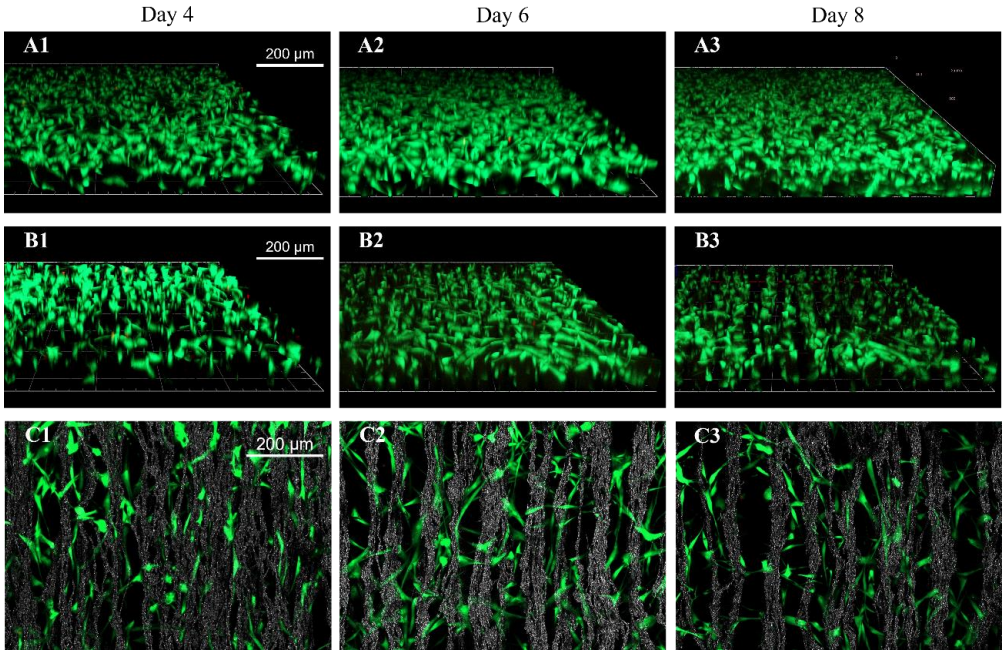

Figure 8.5 Multi-day study of a) fibroblast cells within the control hydrogel formulation (L0.5GHACa) and compared with b) the encapsulated cells within a magnetic hydrogel (L0.5GHACaMP5.5) structured with a banded particle scaffold. The banded structures (white channel) are removed to better visualize the cell orientation. In c) an aerial view of the encapsulated cells is shown along with the particle structure. A 0.5% oxLAM concentration was used in the hydrogel formulation as the lower concentration has a similar gelling dynamic as the 0.625% and was shown to promote cell proliferation better than the 0.625% concentration sample. The hydrogels were stained and imaged on days 4, 6 and 8 with Calcein. This preliminary study on cell proliferation confirms the possibility to guide cell extension and orientation with the anisotropically structured hydrogel. In the control formulation cell growth and extension appears random as the hydrogel retains its inherently isotropic polymeric matrix.

(Fig. 8.5, panel B3) of incubation it is clear that the cells have a predisposition to grow within their isolated band, as opposed to the random directional growth seen in the isotropic particle-free hydrogel (Fig. 8.5, panel A3). In a few cases we have witnessed a cell transverse a band due to a hole in the particle mesostructure. Further optimization to the hydrogel formulation with regards to particle concentration should be considered to ensure fully solid and upright banded structures that withstand the natural hydrogel degradation that takes place over the course of a multi-day study period.

8.3 Conclusions

In this study, we report a method to fabricate magnetic hydrogels and structure them during the gelling phase using advance external triaxial field control. Under a selection of carefully tuned field configurations, magnetic particles self-assemble into sample-spanning 3D particle scaffolds taking on the form of columns, layered sheets, and spirals. Encapsulated cells within the anisotropic particle network are shown to grow in alignment with the microstructure. Guided cell growth and proliferation is needed to more accurately emulate native tissues. Multi-day studies prove that the oxLAM and gelatin polymer matrix is a viable environment for fibroblasts cells, with pore sizes suitable for cell extension. We believe these magnetically structured hydrogels are the first step towards engineering less invasive cell regeneration therapies via an injectable alternative to current implant treatments.

8.4 Experimental section

Triaxial magnetic field control: Magnetic fields were generated using our homemade triaxial magnetic field generator that consists of four coils in the x,y-plane and a fifth coil situated beneath and oriented upwards that produces the z-axis field component. The resultant field is the superposition of each of the three independently controlled field vectors. For high frequency AC fields (upwards of 4 kHz) the triaxial device connects to a fractal capacitor bank and functions as an *R-L-C* circuit. Field configurations are pre-programmed using LabVIEW software. The field to current ratio was calibrated for each axis at the center of the sample platform using a F.W. Bell 5170 teslameter; $H_{x,y}(\text{kA m}^{-1})/I_{x,y}(\text{A}) = 7.77$ and $H_z(\text{kA m}^{-1})/I_z(\text{A}) = 2.80$.

Rheometry: The viscosity curves were measured using a MCR 302 Anton Paar torsional rheometer using a cone-plate configuration. The upper cone geometry had a diameter of 20 mm, 2º angle, and fixed minimum gap of 0.084 mm. The bottom plate was made of brass and temperature-controlled at 25ºC. Four hydrogel precursor solutions were prepared with varying oxLAM (2.5%, 1.25%, 0.625% and 0.5% w/v). In these tests neither magnetic particles nor cells were included in the hydrogel precursor solution. Upon mixing the two hydrogel solutions (gelatin, HA, and $CaCl_2$ in one Eppendorf tube and oxLAM in the other) in equal parts by volume, 80 µL were pipetted onto the bottom plate and the upper cone was immediately lowered, and the Rheoplus

experimental protocol was initiated. An estimated 90 s passes between sample mixing and the first data point acquisition, approximately the same duration between sample preparation and magnetic field application in the hydrogel synthesis experiments. The gelling hydrogel precursor solutions were imposed to a constant shear rate $\dot{\gamma} = 1\ s^{-1}$ with the viscosity measurement was acquired every 1 s for the 2.5% and 1.25% oxLAM hydrogels, and every 10 s for the 0.625% and 0.5% oxLAM hydrogels. The durations of these tests were carried out until the viscosity divergence point was clearly reached, ranging from 200 s for the highest oxLAM concentrations to 2000 s for the lowest tested oxLAM concentration, given that the gelling time is longer for the lower initial polymer concentration.

Oxidized laminarin synthesis: In our proposed hydrogel system the crosslinking occurs between the amine group provided by gelatin and an aldehyde group from the oxidized laminarin [22]. The reactive aldehyde groups are converted from the hydroxyl groups of naturally existing laminarin powder by utilizing sodium periodate ($NaIO_4$) as an oxidizing catalyst. The process begins by dissolving 500 mg of laminarin powder (laminarin from Eisenia Bicyclis, Carbosynth, LOT YL02421) in 5 mL of ultrapure distilled water (Milli-Q, Millipore) within a glass tube, to which 440 mg of $NaIO_4$ is then added. A flow of nitrogen gas is introduced into the glass tube as the mixture is stirred at room temperature with moderate magnetic stirring for a duration of five hours. To halt the reaction, 117 µL of ethylene glycol is added to the solution and is then transferred into a dialysis bag with a molecular weight cutoff 3500 Da (Spectrum Labs). The dialysis bag is immersed in distilled water for a week to remove all unwanted components of the laminarin oxidation process leaving behind the now oxidized biopolymer (oxLAM). Subsequently, the remaining sample is frozen at -20ºC and subjected to lyophilization for two days (Freeze Dry FLEXI-DRY-µP), resulting in a dry thread-like product that resembles cotton candy.

Hydrogel formulation, synthesis and storage: The hydrogels were made by first preparing two separate solutions. In solution 1 gelatin and DMEMsup (DMEM/F12 supplemented with 10% heat-inactivated fetal bovine serum (FBS, Sigma Aldrich), 1% penicillin-streptomycin (Gibco) and 1% l-glutamine (Sigma Aldrich)) are combined using a classic vortex mixer (VELP Scientifica) for 30 seconds and allowed to dissolve at 37ºC for an additional 30 minutes. Then, other component additives including hyaluronic acid (HA) and calcium chloride ($CaCl_2$) were added. The HA was pipetted using a dense

fluid pipette. The solution was vortexed again for 30 seconds and kept at 37ºC for 10 minutes. For hydrogel samples containing cells, they were added to solution 1 right before use. Next, solution 2 was made by combining oxLAM and DMEMsup, vortex mixing for 30 seconds and left to dissolve at 37ºC for 30 minutes. For hydrogels containing magnetic particles, they were then added after this initial 30-minute incubation period. To best avoid particle aggregation, after adding the particles the sample was vortex mixed for 30 seconds, followed by one minute of ultrasound, and then another 5 seconds of vortex mixing. This final mixing procedure was repeated each time before the sample was to be used to redisperse the magnetic particles. Once both solutions were prepared, the required volume of the final hydrogel sample was mixed in a 1:1 ratio of the two hydrogel precursor solutions. Table 8.1 summarizes the hydrogel formulations.

Two type of sample chambers were prepared to contain the hydrogels. For samples analyzed on the day of preparation, the sample chamber was a 12 mm by 12 mm square cutout from stacked layers of adhesive tape (height of 300 µm) on a glass cover slip. To enclose the sample a second cover slip was gently placed on top. Then, the hydrogel precursor solution was structured under the desired magnetic field configuration. For multi-day hydrogel sample analysis, the hydrogel solution was pipetted into a 35 mm diameter petri dish to provide additional volume to add DMEMsup on top of the hydrogel that was routinely changed every 2-3 days. Hydrogel samples containing cells were stored at 37ºC and 5% CO_2.

Cell culture: In this study we conducted in vitro biocompatibility investigations using fibroblasts cells derived from skin samples obtained from donors who provided informed consent and met the requires stipulated for the donation of human tissues and cells, in accordance with Royal Decree-Law 9/2014, issued on July 4. The fibroblasts were obtained through collaboration with the Cellular Production and Tissue Engineering Unit of the Virgen de las Nieves University Hospital in Granada, Spain with the kind assistance of Prof. S. Arias and Dr. A. Fernández-González.

The cell cultures were maintained under standard culture conditions, 37ºC and 5% CO_2, with regular DMEMsup changes every two days. Upon reaching 85-95% confluence the cells were passaged using a trypsinization protocol. For cell seeding, standard polystyrene plates and cell culture-treated bottles were utilized.

Cell viability by *Live/Dead assay*: To assess the viability of the encapsulated cells in our hydrogels, various samples were prepared of each hydrogel formulation for observation on days 4, 6 and 8. These samples, with a volume of 80 μL, underwent a preliminary wash with PBS 2-3 times. Then, they were incubated at 37ºC for 30-40 minutes with a solution contrainting the Live/Dead Viability/Cytotoxicity kit (Invitrogen, OR, USA) in PBS. The concentration used was 4 μL/mL of Ethidium Homodimer and 1 μL/mL of Calcein. Finally, the samples were washed twice again with PBS and their fluorescence was analyzed using a confocal microscope LSM 900 Airyscan 2 (Zeiss, Germany). Calcein was observed under an excitation and emission wavelength of 494 nm and 517 nm, respectively (green channel), and Ethidium Homodimer under 528 nm and 617 nm, respectively (red channel). In this manner, a qualitative observation and analysis of the encapsulated cells in the hydrogels could be performed.

References

[1] Bertsch, P., Diba, M., Mooney, D. J., & Leeuwenburgh, S. C. (2022). Self-healing injectable hydrogels for tissue regeneration. Chemical Reviews.

[2] Nardecchia, S., Jimenez, A., Morillas, J. R., & de Vicente, J. (2021). Synthesis and rheological properties of 3D structured self-healing magnetic hydrogels. Polymer, 218, 123489.

[3] Yang, J. A., Yeom, J., Hwang, B. W., Hoffman, A. S., & Hahn, S. K. (2014). In situ-forming injectable hydrogels for regenerative medicine. Progress in polymer science, 39(12), 1973-1986.

[4] Pardo, A., Gómez-Florit, M., Barbosa, S., Taboada, P., Domingues, R. M., & Gomes, M. E. (2021). Magnetic nanocomposite hydrogels for tissue engineering: design concepts and remote actuation strategies to control cell fate. ACS nano, 15(1), 175-209.

[5] Babu, S., Albertino, F., Omidinia Anarkoli, A., & De Laporte, L. (2021). Controlling structure with injectable biomaterials to better mimic tissue heterogeneity and anisotropy. Advanced Healthcare Materials, 10(11), 2002221.

[6] Gang, F., Jiang, L., Xiao, Y., Zhang, J., & Sun, X. (2021). Multi-functional magnetic hydrogel: Design strategies and applications. Nano Select, 2(12), 2291-2307.

[7] Xue, L., & Sun, J. (2022). Magnetic hydrogels with ordered structure for biomedical applications. *Frontiers in Chemistry*, *10*, 1040492.

[8] Kappes, M., Friedrich, B., Pfister, F., Huber, C., Friedrich, R. P., Stein, R., ... & Janko, C. (2022). Superparamagnetic Iron Oxide Nanoparticles for Targeted Cell Seeding: Magnetic Patterning and Magnetic 3D Cell Culture. Advanced Functional Materials, 2203672.

[9] Demri, N., Dumas, S., Nguyen, M. L., Gropplero, G., Abou-Hassan, A., Descroix, S., & Wilhelm, C. (2022). Remote Magnetic Microengineering and Alignment of Spheroids into 3D Cellular Fibers. Advanced Functional Materials, 32(50), 2204850.

[10] V. Rivera-Llabres, K. Gentry, and C. M. Rinaldi-Ramos, in Magnetic Soft Matter Fundamentals and Applications, ed. J. de Vicente, The Royal Society of Chemistry, 2023, ch. 15, pp. 410-445.

[11] Braunmiller, D. L., Babu, S., Gehlen, D. B., Seuß, M., Haraszti, T., Falkenstein, A., ... & Crassous, J. J. (2022). Pre-Programmed Rod-Shaped Microgels to Create Multi-Directional Anisogels for 3D Tissue Engineering. Advanced Functional Materials, 32(50), 2202430.

[12] Rose, J. C., Cámara-Torres, M., Rahimi, K., Köhler, J., Möller, M., & De Laporte, L. (2017). Nerve cells decide to orient inside an injectable hydrogel with minimal structural guidance. Nano letters, 17(6), 3782-3791.

[13] Babu, S., Chen, I., Vedaraman, S., Gerardo-Nava, J., Licht, C., Kittel, Y., ... & De Laporte, L. (2022). How do the Local Physical, Biochemical, and Mechanical Properties of an Injectable Synthetic Anisotropic Hydrogel Affect Oriented Nerve Growth?. Advanced Functional Materials, 2202468.

[14] Omidinia-Anarkoli, A., Boesveld, S., Tuvshindorj, U., Rose, J. C., Haraszti, T., & De Laporte, L. (2017). An injectable hybrid hydrogel with oriented short fibers induces unidirectional growth of functional nerve cells. Small, 13(36), 1702207.

[15] Pardo, A., Bakht, S. M., Gomez-Florit, M., Rial, R., Monteiro, R. F., Teixeira, S. P., ... & Gomes, M. E. (2022). Magnetically-Assisted 3D Bioprinting of Anisotropic Tissue-Mimetic Constructs. Advanced Functional Materials, 2208940.

[16] Martin, J. E., & Snezhko, A. (2013). Driving self-assembly and emergent dynamics in colloidal suspensions by time-dependent magnetic fields. Reports on Progress in Physics, 76(12), 126601.

[17] Martin, J. E., Venturini, E., Gulley, G. L., & Williamson, J. (2004). Using triaxial magnetic fields to create high susceptibility particle composites. Physical Review E, 69(2), 021508.

[18] Terkel, M., & de Vicente, J. (2020). Magnetorheology of exotic magnetic mesostructures generated under triaxial unsteady magnetic fields. Smart Materials and Structures, 30(1), 014005.

[19] Chang, L., Li, Y., Li, M., Liu, S., Han, J., Zhao, G., ... & Xu, F. (2021). An Injectable, biodegradable magnetic hydrogel system for exogenous promotion of muscle mass and regeneration. Chemical Engineering Journal, 420, 130398.

[20] Terkel, M., Wright, R., & de Vicente, J. (2023). Magnetorheology in unsteady fields: From uniaxial DC to rotating AC fields. Journal of Rheology, 67(4), 833-833.

[21] Nagaoka, Y., Morimoto, H., & Maekawa, T. (2011). Ordered complex structures formed by paramagnetic particles via self-assembly under an ac/dc combined magnetic field. Langmuir, 27(15), 9160-9164.

[22] Lavrador, P., Gaspar, V. M., & Mano, J. F. (2020). Mechanochemical patternable ECM-mimetic hydrogels for programmed cell orientation. Advanced Healthcare Materials, 9(10), 1901860.

Chapter 9

Conclusions

Rheometry and videomicroscopy experiments were carried out to study both particle structuration and the MR effect for our MR fluid system (carbonyl iron particles suspended in water and glycerol) under unsteady magnetic fields, predominantly triaxial precession fields. Our triaxial magnetic field generator is capable of producing static and oscillating fields with field frequencies upwards of 4 kHz by connecting to a fractal capacitor bank. We planned and executed a complete study of the rheological response of MR fluids under uniaxial DC to rotating AC field configurations and the intermediate precession field configurations in between.

A selection of geometry parameters were studied by means of particle-level simulations including average cluster size, number of clusters, and linearity among others for simulations of particles structuring under both a uniaxial and a precession field, with the latter exceeding the former in cluster size indicating greater lateral connectivity. These parameters, as well as a more thorough analysis of particle connectivity showed that simulated MR fluid systems deform similarly from a structural perspective and reach a comparable dynamic yield stress. However, a simulated suspension structured under a precession field did show a slight uptick in the static yield stress, or the minimum force required to induce flow. Experimental rheograms further validate the notion of a measurable increase in the yield stress for specified precession field configurations.

We have reported on two main aggregation dynamics that enhance the magnetorheological effect using time-varying precession fields and have shown a clear improvement over the uniaxial DC case.

- For low Mn precession fields the chain vector, or the rotating aggregate, will typically follow in line with the field vector. In this scenario the dipolar magnetostatic forces dominate the hydrodynamic forces and therefore the phase difference between the field and chain vectors is minimal as viscous drag is inconsequential. As a result, columnar structures prevail under these precession fields and for low precession angles these field configurations promote lateral chain coalescence through direct contact or a change in the spatial orientation from being in registry (repulsive) to out of registry (attractive for small separation distances). Thicker particle aggregates are therefore more resistant to deformation under applied shear. Particle-level simulations were also employed to study the average cluster size of a simulated box of 1000 particles under analogous conditions and similar showed a cluster size peak for low precession angles in the low Mn regime.

- In the case that the magnetic and hydrodynamic forces are more or less balanced, with a $\mathrm{Mn} \sim 1$, the MR enhancement witnessed for low precession angle configurations appears to be distinct from the low Mn explanation involving chain thickening via lateral coalescence. Through visual inspection of videomicroscopy experiments, we did not observe any noticeable variation in aggregate thickness, and yet, the MR response showed the highest measured increased of the storage modulus over the baseline uniaxial DC case for the $\mathrm{Mn} = 2$, $\theta_f = 20^{\circ}$ configuration. What we do observe, however, is an increasingly disordered response of the dynamic collapsed structures, most discernible at $\theta_f = 45^{\circ}$ where particles within each column escape from the center lateral axis and return in a chaotic fashion. Given the natural progression of this disordered behavior, we can make the argument that at $\theta_f = 20^{\circ}$ there may still be some particle agitation on a microscopic interparticle level, akin to thermal fluctuation in Brownian nanoparticles. As a result, we deduce that this particle movement promotes structural compacting as the particles would find a low energy configuration and, in turn, bolsters the MR fluid's resistance to deformation.

Beyond studying the MR effect, we also explored using triaxial field control to drive the formation of particle structures in a hydrogel system. The high water content environment of hydrogels makes this system viable for tissue regeneration, however, its inherent isotropic matrix of crosslinked polymers fails to depict the often anisotropic hierarchically-ordered structure of biological tissues. We were able to break the isotropy by incorporating magnetic particle scaffolds in the hydrogels. Uniaxial and time-varying biaxial and triaxial fields were employed to induce the formation of complex particle scaffolds. Depending on the magnetic field configuration we can drive the particle interaction and structuration into columnar, layered, spiral-like, and crosshatch structures. By combining the magnetically responsive particles, fibroblast cells, and a modified polysaccharide and protein polymer mixture into the hydrogel precursor solution, these particle scaffolds are trapped following the gelation of the hydrogel and provide additional structural reinforcement. Furthermore, the anisotropic particle microstructure provides an oriented matrix for the encapsulated cells, as confirmed by confocal microscopy experiments. A multi-day study showed both cell growth and oriented extension, confirming that the oxidized laminarin and gelatin polymer network is a compatible environment for cell viability and proliferation. We foresee this work as an exciting introduction to developing cell regeneration therapies that more closely represent the anisotropic network of some native tissues.

We hope the research presented in this thesis pays respect to the extensive hard work put into the theory of particle interactions in triaxial magnetic fields and encourages others to find new and exciting applications that make use of advance dynamic field control.